Bio-inspired Oleophobic/Conductive Micro/nano Structures and Their Applications in Frozen Oil Adhesion Reduction

by

Zihe Pan

A thesis

presented to the University of Waterloo

in fulfillment of the

thesis requirement for the degree of

Doctor of Philosophy

in

Chemical Engineering

Waterloo, Ontario, Canada, 2016

AUTHOR'S DECLARATION

I hereby declare that this thesis consists of material all of which I authored or co-authored: see Statement of Contributions included in the thesis. This is a true copy of the thesis, including any required final revisions, as accepted by my examiners.

I understand that my thesis may be made electronically available to the public.

Statement of contributions

Zihe Pan, Tianchang Wang, Shaofan Sun, Boxin Zhao. Durable Micro-structured Surfaces: Combining Electrical Conductivity with Superoleophobicity. *ACS Applied Materials & Interfaces* **2016**, *8*, 1795−1804.

Zihe Pan, Wei Zhang, Andrew Kowalski, Boxin Zhao. Oleophobicity of Biomimetic Micro-patterned Surfaces and Its Effect on the Adhesion of Frozen oil. *Langmuir*, **2015**, *31*, 9109-9110.

Zihe Pan, Hamed Shahsavan, Wei Zhang, Fut K Yang, Boxin Zhao. Superhydro-oleophobic Bio-inspired Polydimethylsiloxane Micropillared Surface via FDTS Coating/Blending Approaches. *Applied Surface Science,* **2015**, *324*, 612-620.

Zihe Pan, Tianchang Wang, Yikang Zhou, Boxin Zhao. Development of Electrically Conductive–Superoleophobic Micropillars for Reducing Surface Adhesion of Oil at Low Temperatures. *Applied Surface Science*, **2016**, *389*, 623-631.

I am the first author of all these peer-reviewed journal publications.

Abstract

Inspired by the excellent superhydrophobicity and self-cleaning properties of the lotus leaf, numerous superhydro-oleophobic micro/nanostructures have been developed which mimicked biological systems. These structures have broad applications in industrial processes, especially oil transportation, oil/water separation and anti-fouling applications where oil adhesion is a critical factor. Although the adhesion properties of oils have been well explored on a variety of surfaces at ambient environment, low temperature behaviors were rarely reported especially when the oil is frozen under a frigid environment. For instance, there are cases in which oils are stuck or frozen onto the walls of engines or pipelines resulting in a large drag force thus leading to excess energy consumption and potential instrument malfunction. In this research project, the initial stage was mainly focused on developing an effective approach to construct well-defined superhydro-oleophobic microstructures and investigating the effects of structures and surface chemistry on superoleophobicity. In this stage, two different chemical modification approaches were applied to both flat and micropillared PDMS: 1) vapour deposition of trichloro (1*H*, 1*H*, 2*H*, 2*H*-perfluorooctyl) silane (FDTS) on cured polydimethylsiloxane (PDMS) elastomer surface (FDTS coated PDMS); 2) blending FDTS with the liquid PDMS precursor before curing (FDTS blended PDMS). Surfaces with varied oleophobicity were fabricated to investigate the effects of superhydro-oleophobicity on the reduction of frozen oil adhesion as characterized by knock-off tests. The relationship between the oleophobicity, which ranged from oleophilic flat surfaces to superoleophobic micropillars, and the reduction of oil adhesion at low temperatures was examined. It was observed that reduced contact angle hysteresis (CAH) led to reduced adhesion strength. By blending FDTS into PDMS micropillars, 60% adhesion strength reduction compared with flat surfaces was achieved. In order to eliminate the frozen oil effectively, electrical de-freezing was proposed by passing electrical current through the top surface layer to induce joule heating effect. To achieve this, epoxy-silver flakes composite micropillars were developed, demonstrating electrical conductivity and superoleophobicity. The effects of resistivity and superoleophobicity on the reduction and elimination of frozen-oil adhesion have been systematically studied, showing that the larger the resistivity and the oleophobicity, the less force was needed to remove frozen-oil droplet. After developing the electrically conductive polymer composite micropillars for eliminating frozen oil adhesion, we have extended this work, aiming to reduce the amount of conductive Ag flakes in the composite and make stretchable multifunctional composite elastomers. Electrically conductive and superoleophobic PDMS has been fabricated by embedding Ag flakes (SFs) & Ag nanowires (SNWs) into microstructures of the FDTS-blended PDMS elastomer achieved in the first stage of this project. A series of surface analyses and characterizations showed that highly conductive and superoleophobic surfaces were indeed obtained with a relatively low surface coverage of conductive fillers. A significant improvement to the conductivity was further achieved by using SNWs to partially replace the SFs. The stretchability and conductivity were examined under external strain, which showed that the as-prepared samples are highly stretchable and reversible. The electrical resistance of the SFs/SNWs embedded surface was less dependent on the strain due to the presence of the SNWs, creating a bridging effect and allowing current to flow consistently even as the silver particles were stretched apart from each other. This research demonstrates a simple approach to transform insulating elastomers into functional composites with a desired surface oleophobicity and electrical conductivity, which is of great help for the development multifunctional superoleophobic structures and their applications in oil adhesion reduction at low temperatures.

Acknowledgements

I am very fortunate to have an opportunity to pursue my Ph.D. degree in Department of Chemical Engineering and Waterloo Institute of Nanotechnology in University of Waterloo; therefore there are many people I have to thanks for their contributions in my success. First and foremost, I would like to express my sincerely gratitude to my supervisor Professor Dr. Boxin Zhao. I appreciate your contributions of time, insightful discussions, expert guidance and abundantly support on making my Ph.D. study productive. I am also thankful for your great patience and encouragement allowing me to reach current achievement. Your enthusiasm on research and rigorous scientific approach has set an excellent example as successful scientist and professor. Without your support this research project would not have come true.

I would also like to express my deepest appreciations to community members, for your brilliant comments and suggestions. Your profound knowledge expands my research in various perspectives.

I would like to express my special thanks to all my lab mates and friends for their help during my PhD study and research. The joyful moments we spent together are memorable. Here, I would like to express my thanks to Hamed Shahsavan for his help on teaching me to use the instruments and discussions on my research. I am also like to thank Wei, Zhang, Fut (Kuo) Yang, Behnam Meschi Amoli, Alecksander Cholewinski, Josh Trinidad, Tianchang Wang for their help on improving my scientific writing.

I would also express my deeply thanks to my dad and mom, Lin Pan and Meirong Zhu, for giving me life and creating good education opportunities, and your expectations motivated me to work hard all the time. I would like to say a heartfelt thanks to my dear wife Wenjuan Li, for

your unconditional love and support. Thank you for accompanying me to get through the difficult times. I appreciate your sacrifices all these years and the priceless gift: our daughter Mo Pan. Without your support and understanding I cannot complete this thesis on time. I also would like to express my sincerely thanks to my parents in-law for their great help and support during my Ph.D. study.

I wish to acknowledge China Scholarship of Council and University of Waterloo for providing me scholarship to pursue my PhD degree.

Dedication

I dedicate this dissertation to my beloved wife Wenjuan Li. I am truly grateful for your understanding, support, encouragement and sacrifices all these years. Having you with me is the greatest happiness in my life.

This dissertation is also dedicated to my loving and caring daughter Mo Pan. You bring endless joy and happiness to our family. I wish you grow up happy and healthy. Dad will love you forever.

This dissertation is dedicated to my parents, Lin Pan and Meirong Zhu, for the dreams you always had on me when I was a kid.

This dissertation is dedicated to my grandparents Zhimin Pan and Suzheng Gu, Quanjun Zhu and Cuiping Wang, for teaching me to be a better man and your unconditional love.

This dissertation is dedicated to my sisters Xiaofei Pan and Xiaoxuan Pan for your companion, love and support.

Table of Content

List of Figures

List of Tables

List of Abbreviations

3D	Three Dimensional
Adv.	Advanced Contact Angle
AFM	Atomic Force Microscopy
ATF	Auto Transmission Fluid
CA	Contact Angle
CNFs	Carbon nanofibers
CNTs	Carbon nanotubes
CPCs	Conductive Polymer Composites
CVD	Chemical Vapor Deposition
DC	Direct Current
EDOT	3,4-ethylenedioxythiophene
FDTS	Trichloro (1*H*, 1*H*, 2*H*, 2*H*-perfluorooctyl) silane
FTIR	Fourier Transform Infrared Spectroscopy
GF	Graphene Foam
LED	Light Emitting Diode
μCP	Micro contact Printing
PDMS	Polydimethylsiloxane
PMMA	Poly(methyl methacrylate)
PMC	fluoroacrylic copolymer
Ra	Arithmetic Mean Surface Roughness
Rq	Root-Mean-Square Roughness
SEM	Scanning Electron Microscopy
SFs	Silver Flakes
SNWs	Silver Nanoowires
UMT	Universal Macro Tribometer
XPS	X-ray Photoelectron Spectroscopy

Chapter 1. Introduction

Inspired by the lotus leaf, highly water repellent materials have been found to play critical roles in nature, in both everyday life and in industry.[1-10] It has been well accepted that the multiple hierarchical micro/nanostructure and the low surface energy are responsible for the superhydrophobicity and excellent self-cleaning properties.[1-12] So far, a series of bio-inspired superhydrophobic structures [1-10] have been developed for self-cleaning,[13,14] anti-biofouling,[14] anti-icing,[15,16] anti-corrosion,[17] and adhesion reduction[18] applications. Nevertheless, many of the liquids in real cases contain oily components that can easily wet the superhydrophobic surfaces.[19,20] Thus, the fabrication of superhydrophobic surfaces with oleophobicity would meet the increasing demand of bio-nanotechnology and expand potential applications. The design of oleophobic surfaces follows the same principles of fabricating superhydrophobic surfaces, with a particular emphasis on the reduction of surface energy in combination with surface patterning. It is reported that fluoropolymers with high contents of function groups such as, $-CF_3$ and $-CF_2$ have the lowest surface energy. As a result, these fluoropolymers have been widely used to reduce the surface energy of solid surfaces. Also, the trapped air-pockets in the patterned structures can prevent the penetration of the liquids resulting in superoleophobicity.[8,9] Thus far, fluoropolymers with modified micro/nano structured superoleophobic surfaces (nano/micro hierarchical structure[9], micropillars[11] etc.) have been developed. The typical surface modification approaches in the fabrication of superoleophobic materials are chemical vapor deposition,[20-22] electrospinning,[23] dip-coating,[24-30] and plasma treatment to graft the fluoropolymer to the surface.[31-34] All of these methods have drawbacks: chemical vapor deposition and dip-coating of fluorocarbon tends to form aggregates and structural defects,[35] while electron-spinning causes weak bonding between fluoropolymer and substrate, and plasma treatment causes surface damages, creating microcracks.[36-38]

A feasible and simple technique is desired to solve the above problems and reduce the oil adhesion.[39-42] Oil adhesion plays increasingly important roles in industry applications such as in the motor engine, oil pipelines and in lubrication applications etc.[43-47] Although the oil adhesion at room temperatures has been widely studied, the low temperature behaviors of superoleophobic materials are not well studied especially when the oil is frozen under a frigid environment. But such low-temperature phenomena play important roles in engineering applications. For example if the oil is stuck to or frozen in engines or onto pipeline walls, it causes substantially more energy to be consumed with theincreased adhesion, with the potential to lead to instrument failure or cause an accident.[44-46] Thus, it is important to investigate the factors affecting the frozen oil adhesion strength and explore efficient ways to melt away the frozen oils.

The primary objective of this project is to develop multifunctional bio-inspired microstructures with superoleophobicity and electrical conductivity, and apply the as-prepared structures to reduce frozen oil adhesion strength and remove the frozen oil. To achieve this goal, this project was divided into four main sections:

- Fabrication and characterization of bio-inspired superhydro-oleophobic polydimethylsiloxane (PDMS) micropillared surface via trichloro (1*H*, 1*H*, 2*H*, 2*H*-perfluorooctyl) silane (FDTS) coating/blending approaches
- Oleophobicity of biomimetic micropatterned surface and its effect on the adhesion of frozen oil

- Bioinspired electrically conductive and superoleophobic composite microstructures for frozen oil elimination
- Durable microstructured surfaces: combining electrical conductivity with superoleophobicity

In the first part we have performed a series of experimental studies on the fabrication of FDTS coated/blended PDMS micropillars and investigated the superhydro-oleophobic behaviors for the purpose of developing simple and effective approaches to fabricate superoleophobic structures. The oleophobicity difference between FDTS coating/blending approaches and the effectiveness of blended FDTS on superhydro-oleophobicity were also studied. The water and oil contact angles were measured on both FDTS coated/blended PDMS flat and micropillared surfaces. Although the water contact angle on FDTS coated/blended PDMS micropillars were similar, a significant difference between oil contact angles was observed: the oil contact angle on FDTS blended micropillars was larger than on FDTS coated PDMS micropillars. The oleophobicity of FDTS blended PDMS micropillars was attributed to the migration of FDTS to the surface, resulting in surface enrichment of FDTS thereby reducing the surface energy and improving the oleophobicity. In addition, the investigation of FDTS concentration on oleophobicity indicated that the superoleophobicity was independent of the quantity of FDTS.

The extensive study in the first part provided understanding of the role of FDTS in surface energy reduction and self-cleaning performance improvement. One of the applications of superoleophobic material is for self-cleaning and adhesion reduction, especially at low temperatures.[48-50] Thus in the second step, the effects of surface chemistry and structures on the frozen oil adhesion were systematically studied at -25 ºC. For this, experimental set up for the frozen oil adhesion measurements were designed and built. The key feature was to equip a custom-built cooling system into a Universal Materials Tester (UMT). Diiodomethane was chose as model oil; a droplet of 10 µl was placed onto the oleophilic, oleophobic and superoleophobic surfaces, frozen and knocked-off. The knock-off force was used to quantitatively characterize the adhesion of frozen oil.

To further reduce the frozen oil adhesion and remove frozen oil effectively, superhydro-oleophobic surfaces[51-56] were functionalized with electrical conductivity aiming to utilize the Joule heat[57-61] generated from an applied DC current[62-67] to melt the frozen oil. In the third part of this project, electrically conductive and superoleophobic micropillars were fabricated by using Ag flakes-epoxy conductive polymer composites (CPCs) [68-74] due to their unique advantage of integrated polymer and conductive filler properties[75-80]. Comparing with PDMS, non-conductive epoxy can be made conductive at relatively low content of Ag flakes, while it required more than 80 wt% Ag flakes to make PDMS conductive.[79-84] The surface properties, conductivity and frozen oil elimination were studied for epoxy-silver flakes composite micropillars. The embedded monolayer of FDTS on the micropillar surface and the composite micropillars are responsible for the superoleophobicity and excellent self-cleaning property. Two approaches for melting the frozen oil were introduced and compared. It was determined that the DC current heating effect (“bottom-up” melting) is much more efficient than the hot wind effect (“top to bottom” melting).

However, the typical drawback of CPCs is the consumption of large amount of conductive fillers, leading to high manufacturing costs. In addition, the conductivity is not improved with the increasing fraction of conductive fillers. Thus in the last part of this project, Ag flakes (SFs) and Ag nanowires (SNWs) were used as conductive fillers embedded into superoleophobic microstructures to delivery electrical conductivity. The strechability of the prepared microsructured samples and durability of these fillers embedded in microstructured PDMS and the superoleophobicity were studied. In addition, frozen oil adhesion tests were performed on SFs embedded PDMS microstructures to evaluate their frozen oil adhesion reduction properties.

The results presented in this project provide fundamental knowledge for further investigations of on the fabrication of superoleophobic and conductive micro/nanostructures and their application in frozen oil adhesion reduction. We believe that our efforts and areas of focus are distinct from those of other researchers and will provide complementary contributions to this field.

In Chapter 2, the literature review and the underlying principles related to the superhydro-oleophobic and electrically conductive microstructures on frozen oil elimination will be discussed in depth. In Chapters 3 to 6, the results of four research steps as presented at the beginning of this chapter are presented. In Chapter 7, the work in this thesis is summarized and possible suggestions for future work in this field are provided.

Chapter 2. Literature Background

2.1. Wetting Phenomena in Nature

Wetting phenomena can be found everywhere in nature. A variety of wettability states are observed on biological and synthetic materials. Some plant leaves are superhydrophobic and have low contact angle hysteresis for self-cleaning.[1,2,85] Some of them are superhydrophobic but have high contact angle hysteresis which can keep moistures on leaf surfaces.[1,2,85] Some are superhydrophilic for nutrition uptake and photosynthesis.[85] One classic case of the extremely high water repellency is found on the surface of plant leaves, where water droplets bead up and sit on the surface without wetting (Figure 2.1a).[85] The spherically-shaped water droplets can easily roll down and take away the dust from plant leaves to clean themselves. Wetting phenomena are also commonly seen in our daily life. For instance, fabric clothes are completely wetted by water, leaving water stains on surface (Figure 2.1b).[86] Water droplets ball up on transparent and superhydrophobic glass slide (Figure 2.1c) and roll down carrying away particles leaving clean traces on glass (red rectangles) (Figure 2.1d).[87] For technical applications, wetting is an important property for self-cleaning, anti-fogging, anti-fouling, painting, waterproof products, oil recovery, water recycling, coating *etc*.[1-10] At micro/nanoscales, it affects micromachining such as microfluidic channel, nanoprinting, and lab-on-a-chip systems as surface tension controls the spreading of liquid.[1-10] Several classical theories have been developed to understand the principles behind wetting.[11,12]

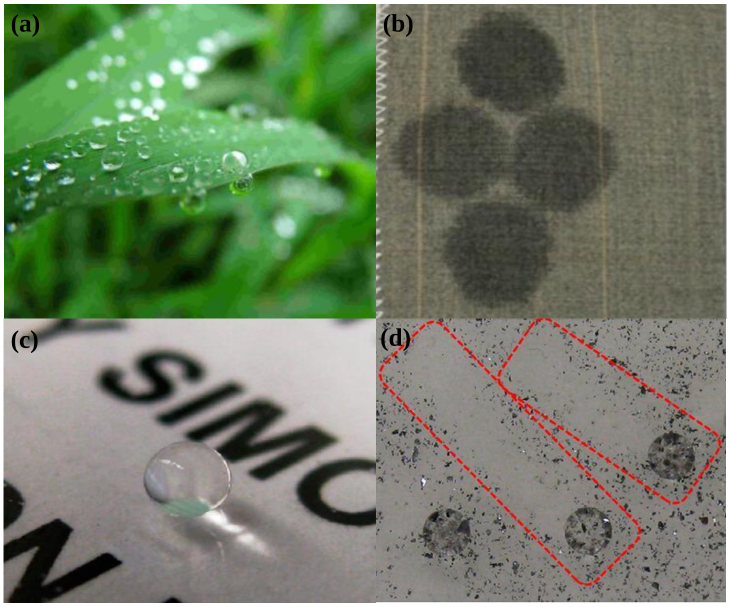

Figure 2.1 Examples of wetting phenomena in everyday life: (a) plant leaf remains non-wetted after rain;[85] (b) water wets the fabric surface completely to leave water stains;[86] (c) water droplet beads up on transparent superhydrophobic glass slide;[87] (d) water droplets roll down carrying away the dusts to leave a clean trace on glass (in red rectangles).[87]

2.2 Theoretical background

Wetting is the interaction between liquid and solid surfaces;[88] the intermolecular force at the interface determines whether the solid can be wetted by a given liquid or not.[11,85,88] In the process of wetting, the air-solid interface is replaced by an equivalent-sized liquid-solid interface and a new liquid-air interface is formed.[11] The system consists of three interfaces in total: a solid-liquid interface, a liquid-air interface and a solid-air interface. Each interface has specific interfacial energy and any change in the interfaces causes a variation in free energy of the whole system.[2,11,85] The change of free energy of the whole system determines the wetting behaviors of the liquid, i.e. whether or not the liquid spreads on the surface.[11] The most intuitive parameter reflecting the wettability of solid surface is the liquid contact angles, including static contact angle and advancing/receding contact angles.[2,11,85,89-91]

Contact angle is defined as the angle between the liquid and solid; its measurement is a common approach to characterize the surface property of the solid surface.[91] Four general cases of wettability have been recognized when water droplet is placed on a solid surface:[85] (a) hydrophilic state, where water wets the surface, the water contact angle is less than 90° (Figure 2.2a); (b) hydrophobic state, where the water droplet on a surface shows a contact angle larger than 90° but less than 120° (Figure 2.2b); (c) superhydrophilic state, where water wets the surface and spreads immediately, leading to a contact angle close to 0° (Figure 2.2c); (d) superhydrophobic state, where the water droplet retains a spherical shape on the surface, showing a contact angle usually higher than 150° (Figure 2.2d).[85]

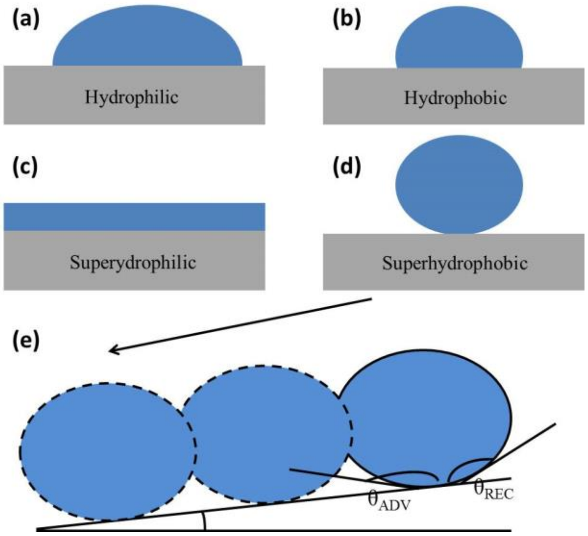

Figure 2.2 Four general cases of wettability:[85] (a) hydrophilic; (b) hydrophobic; (c) superhydrophilic and (d) superhydrophobic; (e) Contact angle hysteresis $\theta_H = \theta_{ADV} - \theta_{REC}$.[92]

The contact angle hysteresis is another important parameter for evaluating the interaction between liquid and solid. It depends on the surface heterogeneity, roughness, adsorption, deformation and other factors of the solid surface.[2,90,91] It is defined as the difference between the advancing and receding contact angles as shown in Figure 2.2e.[91] The advancing contact angle is measured at the front of the liquid droplet when the droplet starts to slide. This is the largest contact angle that can be measured on the solid surface.[89-91] On the other hand, the receding contact angle is measured at the backside of the liquid droplet when it starts to slide and it is the lowest theoretical contact angle.[89-91] Contact angle hysteresis determines the motion behavior of water on solid in motion.[85] Surfaces with higher contact angle hysteresis require more energy to remove the liquid because the droplet adheres to the surface and therefore is difficult to remove. This means that more energy would be dissipated when liquid flows along such a surface. Surfaces with lower contact angle hysteresis allow a droplet to easily roll off from the solid surface. These aspects are important for designing self-cleaning, micro/nanofluidic materials.[1-3]

2.2.1 Young's Equation

From a thermodynamics perspective, Young's equation as given in Equation 2.1 provides the basic principle to explain the wetting phenomenon.[1-3,11] It is established based on the assumption that the solid surface is smooth and flat and the system is ideal. It neglects influences such as surface roughness, size of droplets, liquid evaporation, surface swelling, vapor condensation and chemical heterogeneity.[2,92] The contact angle is a balance of solid-gas, liquid-gas and solid-liquid interfacial forces under thermodynamic equilibrium (Figure 2.3a).[1,2,7-12]

$$\gamma_{SL} + \gamma_{LG} cos\theta_C = \gamma_{SG} \qquad \text{Equation 2.1}$$

where γ_{SL}, γ_{LG} and γ_{SG} are the interfacial tensions of solid-liquid, liquid-gas and solid-gas interfaces respectively. θ_C is the equilibrium contact angle. The maximum water contact angle on a smooth and flat surface is approximately 120° due to the large interaction between water molecules and substrate.[11] Roughness (such as microstructure or nano/microstructure) on such surface can enhance the water contact angle further ($150° < \theta < 170°$).[11] Thus far, two general models, the Wenzel model and Cassie-Baxter model, have been proposed to study the effect of surface roughness on wettability.

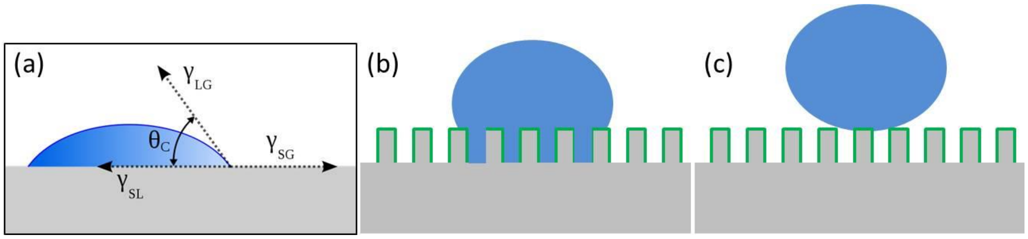

Figure 2.3 (a) Yong's model;[1] (b) Wenzel model: water droplet penetrates into cavities;[7] (c) Cassie-Baxter model: water droplet sits on the top of structures.[8]

2.2.2 Wenzel Model

Wenzel comprehensively studied the effect of surface roughness on wettability, obtaining that the wettability is proportional to the surface roughness of wetted area.[11] As shown in Figure 2.3b, in the Wenzel state, water is in contact with the solid surface at all points including cavities. This results in a larger actual contact area than what is observed (observed contact area calculated from the contact line of water droplet and substrate).[11,88] The relationship between apparent contact angle and the surface roughness is described in Equation 2.2,[11,88]

$$\cos\theta^* = r\cos\theta_C \qquad \text{Equation 2.2}$$

where $\theta*$ is the apparent contact angle on the rough surface, and *r*, commonly called the surface roughness, is defined as the ratio of the actual area over the apparent area. Equation 2.2 indicates that an increased roughness makes a hydrophobic ($\theta > 90°$) surface more hydrophobic while a hydrophilic surface will become more hydrophilic[11]. That is, the surface roughness amplifies the wettability of the smooth surface. However, the wettability of a surface with extremely high roughness and porous structure cannot be predicted by the Wenzel model. The reason is the extremely large roughness would result in the values of $cos\ \theta*$ larger than 1 or smaller than -1 which is not mathematically possible. In order to solve the problem Cassie and Baxter developed the Cassie-Baxter model.[8]

2.2.3 Cassie-Baxter Model

As illustrated in Figure 2.3c, in the Cassie-Baxter model, water rests on the protrusions of the structured surface.[12] The trapped air in cavities is seen as a non-wetting medium, preventing the droplet from penetrating,[12,87] so that the droplet can easily roll off when the surface is slightly tilted. The Cassie-Baxter equation relates the apparent contact angle to the contact angle on flat surface:

$$cos\,\theta^* = -1 + \Phi_S\,(1 + cos\,\theta) \qquad \text{Equation 2.3}$$

where θ is the contact angle on flat surface, θ^* is the apparent contact angle, and Φ_s is the fraction of the solid in contact with the liquid. Compared to the Wenzel model, the Cassie-Baxter model is applicable to achieve $\theta^* > 90°$, even for $\theta < 90°$ on a flat surface.

2.2.4 Wetting Transition

In most practical situations, liquid-solid contact might change from the Cassie-Baxter model to the Wenzel model irreversibly due to changes in pressure, evaporation, or condensation, or any combination of the three.[93-95] The threshold value θ_C is defined as the transition point of the Cassie-Wenzel state. Combining the Wenzel and Cassie-Baxter equation, the threshold value θ_C can be determined from the Equation 2.4:[2]

$$\cos\theta_C = (\Phi_S - 1)/(r - \Phi_S) \qquad \text{Equation 2.4}$$

Figure 2.4a shows the apparent contact angle $cos\ \theta^*$ plotted as a function of contact angle $cos\theta$ with the solid line displaying the anticipated behavior. The dotted line represents the Cassie regime under a moderate hydrophobicity to stress its metastability.[96] The transition process is complicated and many factors are involved such as the Laplace pressure ΔP across the liquid-air interface as given in Equation 2.5.[2]

$$\Delta P = \frac{2\gamma_{lg}}{R_d} \qquad \text{Equation 2.5}$$

where γ_{lg} is the surface tension of the liquid and R_d is the radius of the droplet.

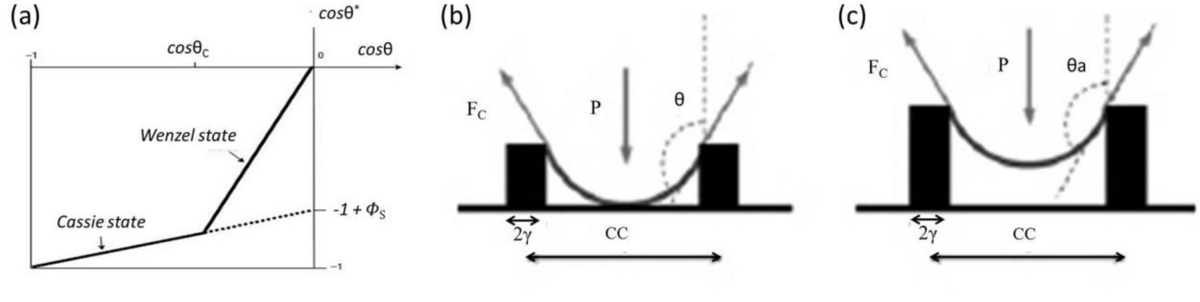

Figure 2.4. (a) The transition between Cassie-Baxter and Wenzel state;[96] (b) liquid touches the bottom of the solid surface;[97] (c) the advancing contact angle reaches the critical contact angle so that the liquid slides down the structure.[97]

Two Cassie-Wenzel transition cases have been proposed in literature:[97] touch down (Figure 2.4b) and sliding (Figure 2.4c). The “touch down” case studies the surface with low pillar height while the “sliding” case focuses on the case with high pillar height. In the “touch down” scenario, the droplet penetration depends on the droplet pressure and the critical impalement pressure. This is defined in Equation 2.6:

$$P_{imp} = \frac{\gamma h R}{CC^3} \qquad \text{Equation 2.6}$$

where P_{imp} is the critical impalement pressure, γ is the surface tension of the testing liquid, h is the height of the pillars, R is the radius of the pillars and CC is the center-center spacing of two pillars. If the external pressure of the water droplet exceeds P_{imp}, liquid penetrates into the grooves and the Cassie-Baxter model transfers into the Cassie-Wenzel state.[50-53] The critical impalement pressure of the “sliding” case is expressed as:[97]

$$P_{imp} = \frac{2\varphi}{1-\varphi}\left|cos(\theta_C)\right|\frac{\gamma}{R} \qquad \text{Equation 2.7}$$

where φ is the solid fraction, θ_C is the advancing contact angle, γ is the surface tension of the testing liquid and R is the radius. If the contact angle θ is larger than θ_C then the liquid will spontaneously penetrate into the cavities and reach the bottom.[97] Physical features such as the height of the microstructures and the spacing between grooves strongly influence the Cassie-Wenzel transition. C. Ran *et al.*[94] studied the influence of the diameter and the depth of nanoholes and pointed out that decreasing the diameter and depth of nanoholes can lead to the transition of Cassie state to Wenzel state.

2.3 Bio-inspired Superhydrophilic, Superhydrophobic Structures

2.3.1 Bio-inspired Superhydrophilic Structures

Superhydrophilicity is a characteristic of any surface with a high surface energy. They have a water contact angle of less than 10°, sometimes close to 0°, which corresponds to the complete wetting state.[84,98,99] The two important factors for the superhydrophilicity are surface structure and surface chemistry.[11,12] Superhydrophilicity is an important issue for plants in nature because it involves many activities such as the water and nutrition uptake as well as the activity of photosynthesis.[98] Wetting behaviors on superhydrophilic plants are divided into three cases based on the surface structure and chemistry: a smooth surface with high surface energy which is permanently wetted; porous and multiple structure surfaces which absorb water; and hierarchical micro/nanostructure surfaces for immediate water spreading.[85]

Figure 2.5a shows the external shape of a pitcher plant which is superhydrophilic.[100] The surface absorbs water moisture to form a thin water film, leading to a slippery surface that can trap insects as food. The microstructure of the peristome is shown in Figure 2.5b in which the pitch value of the microgrooves (covered by hydrophilic hygroscopic nectar) is 500 μm.[100] This greatly enhances the surface roughness and makes the surface superhydrophilic. Figure 2.5c shows 5 μl of water droplets spreads on the ruellia devosiana leaf within 0.2 s (Figure 2.5c).[98] The microstructure of ruellia devosiana leaf is different from the pitcher plant as shown in Figure 2.5d. The surface contains hair papillae, papillae cells, glands and channel structures. However, the glands substrate is hydrophilic. Consequently, the hierarchical structure surface is superhydrophilic.[97] So far, a variety of approaches for fabricating superhydrophilic structures have been developed such as self-assembly, electrospinning, template transfer, layer-by-layer deposition.[99-106] Li *et al.*[101] reported fabricating superhydrophilic polystyrene colloidal crystals in vertically aligned hierarchical arrays for photocatalysis applications. Son *et al.*[104] manufactured nanopillar/holes to improve self-cleaning and anti-reflective properties. The results showed that the light transmittance of the nanopillar/holes were as high as 94%.

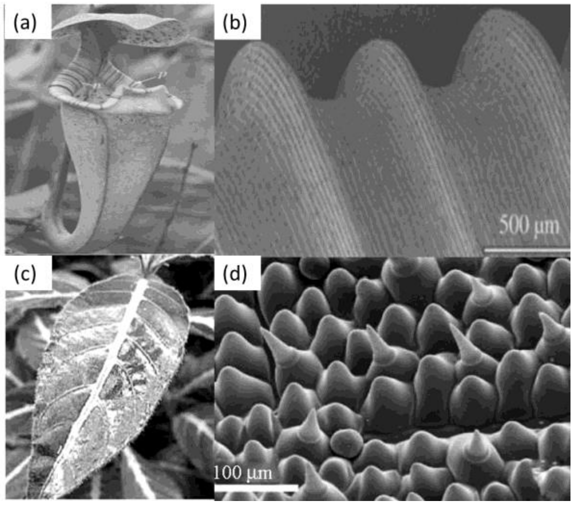

Figure 2.5. (a) pitcher plant and (b) the microstructure;[100] (c) ruellia devosiana leaf wetted by water with contact angle of 0° and (d) the microstructure taken by SEM.[98]

2.3.2 Bio-inspired Superhydrophobic Structures

2.3.2.1 Bio-inspired Structures with "Lotus Effect"

Superhydrophobicity is the ability of a solid surface to repel water, exhibiting a water contact angle ranging from 150° to 180°.[12] The measured water contact angle on lotus leaf is 162° (Figure 2.6a) with a low contact angle hysteresis (CAH) of 2°.[107] The superhydrophobicity and low CAH provide the lotus leaf self-cleaning property. Scientists define this property of lotus leaf as the "lotus effect".[1,7,107] Microstructure investigation showed that the lotus leaf is composed of micro scale papillae (Figure 2.6b) and each single micropapilla consists of many nano sized nipples, forming a hierarchical structure (Figure 2.6c).[107] Surface chemistry analysis results indicate that the multiple micro/nanostructure is covered with a thin layer of wax which reduces the surface energy of the lotus leaf and makes the surface hydrophobic. Additionally, the multiple micro/nano structures significantly enhance surface hydrophobicity, thus the lotus leaf achieves the superhydrophobic state.[11,12,107] Rice leaf is another common example in nature exhibiting the "lotus effect" (Figure 2.6d).[4] The microstructure of the rice leaf is similar to the lotus leaf: plenty of well-arranged microparticles are aligned on the surface and each individual microparticle is composed of nanofibers. The length of these nanofibers reaches 1-2 μm with a diameter about 200 nm (Figure 2.6f).[4] Comparing with the lotus leaf, the well-arranged microparticles form two dimensional structures display varied wettability in each direction. The contact angle in the parallel direction is 153° while it is 146°in the perpendicular direction.[4]

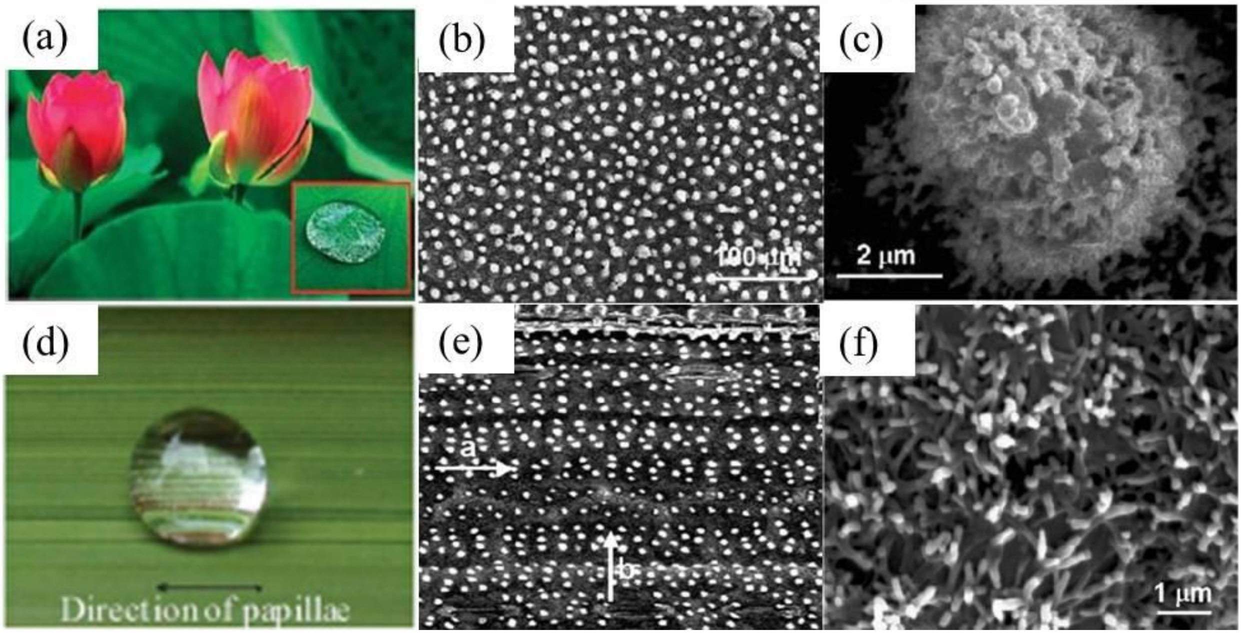

Figure 2.6. (a) A water droplet rests on a lotus leaf without wetting the leaf;[107] (b) SEM image of lotus leaf showing micropapillae on the surface;[107] (c) high magnification SEM image of a micropapilla indicating the micropapilla is composed of nanonipples;[64] (d) rice leaf with superhydrophobicity;[4] (e) microstructure of rice leaf which is similar to lotus leaf;[107] (f) high magnification SEM image of rice leaf shows the micro particles are composed of nanoscale fibers.[4]

Many insects and animals also have their own specific water repellent and self-cleaning property as well as drag reduction in fluid flows. Several examples with special structures and superhydrophobicity are shown in Figure 2.7. The water strider can walk quickly on the surface of water (Figure 2.7a) with its non-wetted legs.[13] The water strider legs are covered with a mass of oriented micro/nano needle-shaped setae (Figure 2.7b).[13] These micro/nano sized setae structures provide a superhydrophobic state with a static water contact angle of 167.6° ± 4.4°. The SEM image in Figure 2.7c shows that the superhydrophobicity of butterfly wings is attributed to the nanotips/micro anisotropic aligned sheets hierarchical structures (Figure 2.7c and d).[108] Comparing with butterfly wings, cicada wings are made of nano scale pillars. The center-center spacing of nanopillars is around 110-140 nm, and the height of the nanopillars is in the range of 220 to 250 nm (Figure 2.7e).[109] The waxy coating on these regular nanopillar arrays is responsible for the superhydrophobicity (water contact angle of 160°). The shark is known as one of the fastest swimming creature in oceans and its skin is found to have remarkable drag reduction property during swimming. Micrographs of shark skin (Figure 2.7f) reveal that it contains microsized single direction oriented tooth-like scales (dermal denticles) which are covered by specifically sized (Figure 2.7g) and spaced riblets that are oriented parallel to the direction of swimming.[110] This specific structure gives the shark skin excellent self-cleaning, low adhesion, antibiofouling and drag reduction abilities.

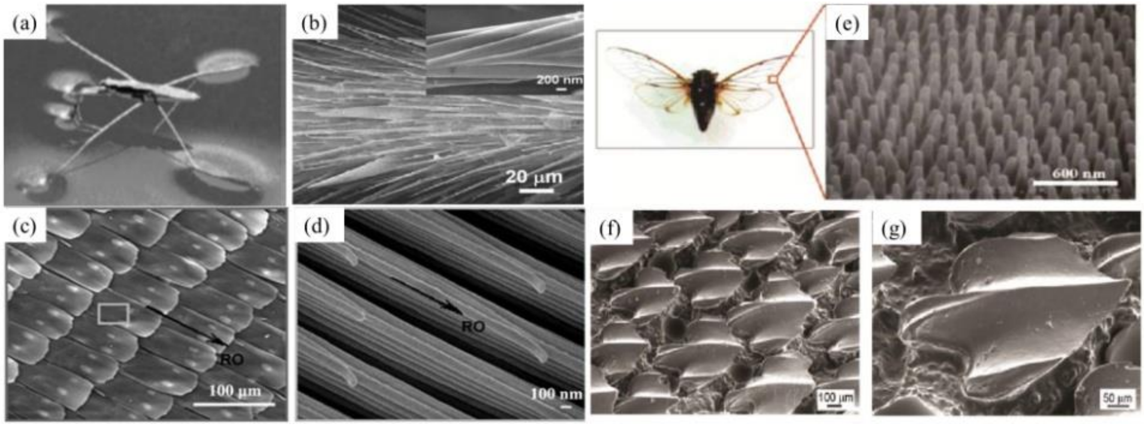

Figure 2.7. (a) Water strider walks on water;[13] (b) micro/nano structure of water strider legs;[13] (c) the step-like butterfly wing[108] and (d) high resolution microimage;[108] (e) micro structure of cicada wing;[66] (f) and (g) shark skin.[110]

The extensive study of bio-inspired structures with superhydrophobicity and remarkable self-cleaning property has led to the development of biomimetic structures. A variety of bio-inspired superhydrophobic structures such as microgrooves,[1] nanoparticles,[26] micro/nanopores,[28] micro/nanopillars,[14] micro/nanofibers[13] have been developed as potential self-cleaning[13,14] materials in anti-icing,[111-113] erosion prevention[17], friction and drag reduction[18] applications. The low temperature behaviors of the superhydrophobic materials, such as anti-icing materials have attracted great interest world-wide.[111-114] Ice accumulated on exposed surfaces (power lines, air craft, offshore oil platforms and wind turbines) cause various problems such as equipment failure or serious accidents, resulting in great economic loss.

Superhydrophobic micro/nanostructures have been proved to be effective to slow down ice freezing and it is reported that there is a close relationship between freezing rate and superhydrophobicity.[49,50] Guo *et al.*[49] reported a micro/nanostructured surface which was fabricated by mimicking the structure of the butterfly wing using microsized stainless steel as a substrate and planting ZnO nanohairs on the substrate. The top view of the micro/nanostructure shows the aligned structure (Figure 2.8a) and the groove which is covered by the nanofibers can be seen from the side view (Figure 2.8b). The SEM images of the top and side views in Figure 2.8c illustrate that the prepared step-like microstructure is similar to the features of a butterfly wing. The formation time of ice on different surfaces, which evaluates the anti-icing property is compared in Figure 2.8d. From the chart we learn that the ice formation on micro-/nanostructured surface (MN-) takes a longer time than on the nanostructured surface (N-), microstructured surface (M-) and smooth surface (S). This is because of the large microsize grooves (260 μm in periodicity and 75 μm in height), which are easier for the water to penetrate into, leading to the fast formation of ice.

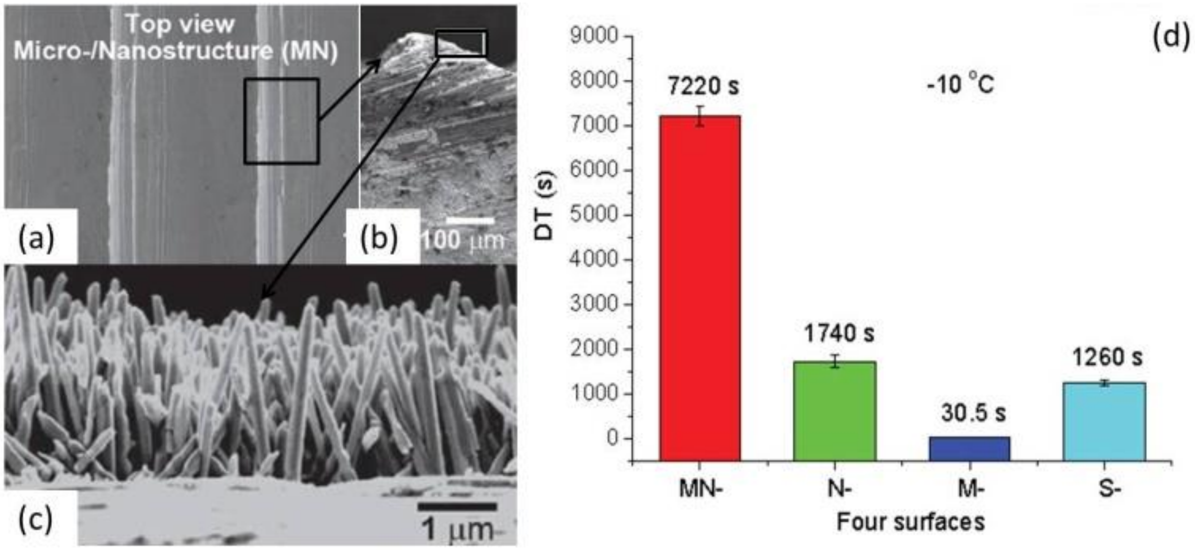

Figure 2.8 Top view (a) and side view (b) of the overall structure of microgrooves; (c) side view of nanohairs on microgrooves; (d) ice formation delay comparison on nano/microstructure (MN-), nanostructured surface (N-), microstructured surface (M) and smooth surface without any structure (S).[49]

The superhydrophobicity is not only helpful for delaying ice formation, but can also be used to reduce ice adhesion. The synergetic effects of surface structure and surface chemistry on ice adhesion can be explained in terms of dynamic contact angles (advancing and receding contact angles) and contact angle hysteresis. Since the surface wettability determines the energy required for the elimination of ice from surfaces, the work of adhesion between water droplet and substrates was determined by the receding contact angle. Meuler et al.[48] studied the relationship between wettability and ice adhesion comprehensively on varied surfaces ranging from hydrophilic to superhydrophobic and found that ice adhesion strength increased significantly when the surface transferred from superhydrophobicity to hydrophilicity. He et al.[114] explored the effects of surface structure on ice adhesion showing that the contact angle hysteresis has a remarkable influence on ice adhesion. As illustrated in Figure 2.9, three different surfaces: micropillars (Figure 2.9a), hierarchical micro/nanopillars (Figure 2.9b) and smooth surface (Figure 2.9c) were observed indicating that the ice adhesion strength decreased with the decrease of contact angle hysteresis (Figure 2.9d).

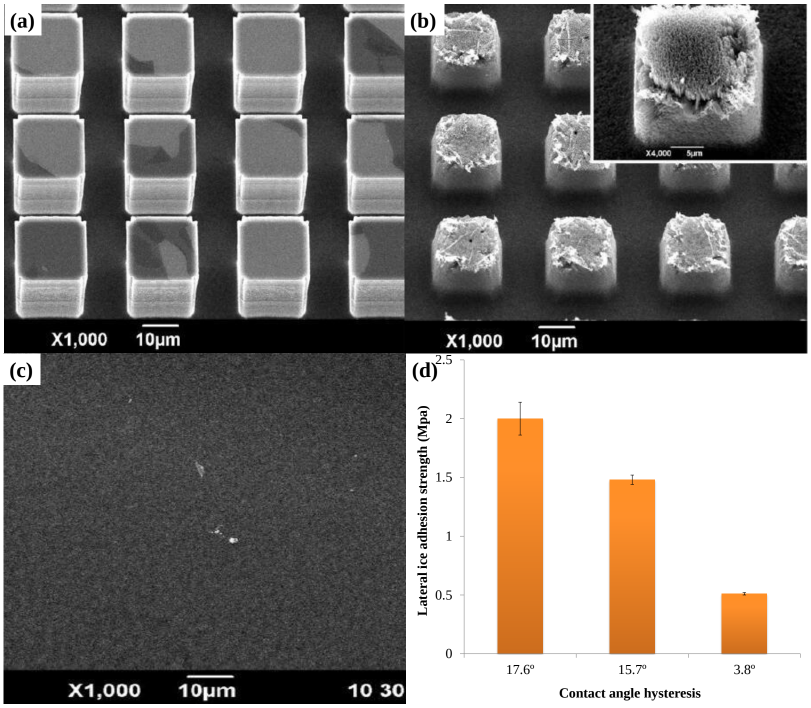

Figure 2.9. SEM images of (a) micropillars, (b) micro/nanopillar hierarchical structure, (c) smooth surface and (d) the relationsip between ice adhesion and contact angle hysteresis on corresponded surfaces.[114]

2.3.2.2 Bio-inspired Structures with “Petal Effect”

The other well-known superhydrophobicity phenomenon is the “petal effect”.[1] Surfaces with “petal effect” show a superhydrophobic state with static water contact angle larger than 150°, but with a strong adhesion to water.[115] The contact angle hysteresis of “petal effect” structure is very large. For instance, the water droplet sticks to rose petal even when it is placed upside down.[116,117] Surfaces with “petal effect” are not rare in nature, such as on garlics, rose petal, lizards and gecko feet, *etc.*.[1,4,116,117] These interesting materials have wide applications, such as the transport of microliter-sized superparamagnetic liquid droplets by alternating magnetic fields.[1,4]

Figure 2.10a is the microstructure of rose petal showing lots of hierarchical microbumps on rose petal.[1] Many nanofolds were further found on the top of single microbump (Figure 2.10b).[13] This multiple hierarchical micro/nanostructure resulted in a water contact angle of 152° (Figure 2.10c).[13] However, the water droplet clings on the surface without moving even when it is inverted (Figure 2.10d), indicating a strong adhesion force.[13] Compared with lotus leaf, the pitch value (center-center spacing between microbumps) of the microbumps and nanofolds on rose petals are larger than on the lotus leaf and the depth of the microvallies are much smaller. With these parameters water can easily penetrate into the bottom of the pillar structure as illustrated in Figure 2.10e, thus the surface of rose petals shows a stronger adhesion to water droplet. On the other hand, more air pockets are formed between the microstructures with lower pitch value and higher pillars as illustrated in Figure 2.10f, which prevent the liquid penetration and minimize the contact area between water and the surface and eventually results in a superhydrophobic surface with lower contact angle hysteresis and lower adhesion.[115,116]

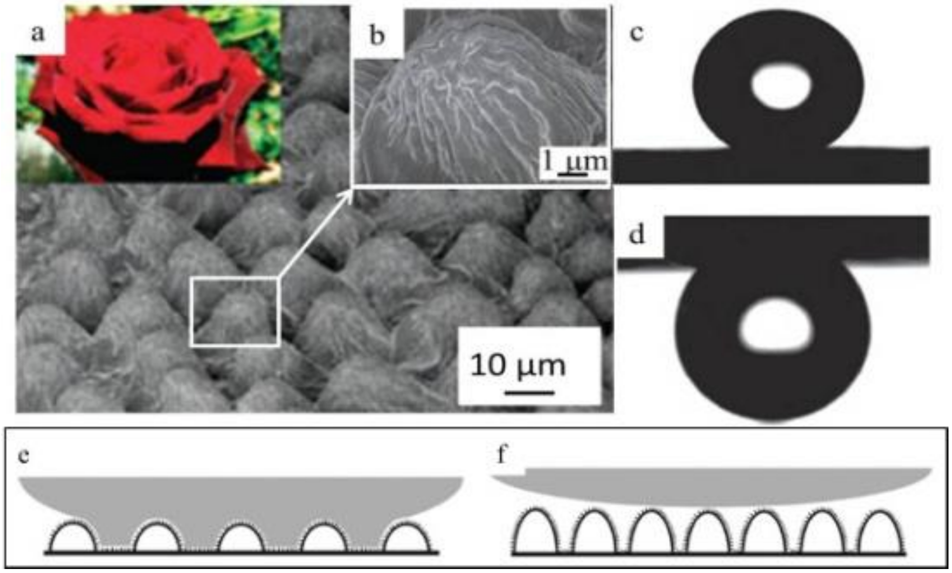

Figure 2.10. (a) The micro structure of rose petal shows the size of the micropapillae is around 10 µm[1] and (b) the high magnification SEM image of individual micropapillae shows nano sized folds;[1] (c) static water contact angle on rose petal is 152° and (d) the water droplet clings to the surface even when it is placed upside down;[1] (e) water pins to the cavities;[115] (f) water rests on the structures.[115]

Feng *et al.*[117] mimicked rose petal using polystyrene and the duplicated structure is shown in Figure 2.11a. The water droplet sticks to the surface even when the surface is placed upside down, implying superhydrophobicity and strong adhesion. Ebert *et al.*[116] studied the wear resistance of the biomimetic rose petal structure *via* a replicating microstructure from Si micromodel. The overall structure consisted of low density micropillars with large center-center spacing as shown in Figure 2.11b;[116] the inset image shows the single pillar's surface which was covered by nanoparticles. This hierarchical structure gave rise to strong adhesion to water without dropping from the surface when it was placed inverted. The wear resistance study was performed under AFM (Figure 2.11c) by evaluating the roughness before and after the test. The root mean square roughness (RMS) and peak-valley roughness (PV) were 463 nm and 17599 nm respectively while RMS and PV after sliding were 455 nm and 1782 nm, respectively which did not change significantly indicating the surface was anti-wear (Figure 2.11c).

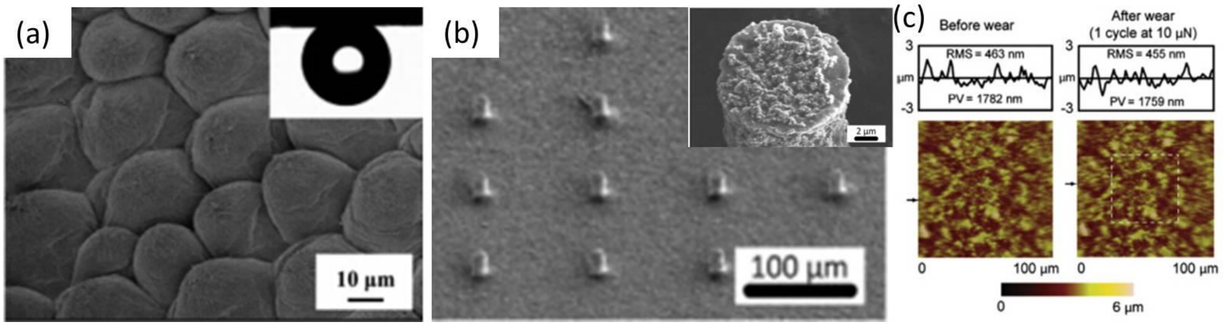

Figure 2.11. (a) bio-inspired rose petal structure with strong adhesion;[117] (b) hierarchical micro/nano pillar showing superhydrophobicity and strong adhesion;[116] (c) wear test performed by AFM.[116]

2.4 Bio-inspired Superoleophobic Structures

Generally, materials with only superhydrophobicity can be contaminated by organic oily species,[14, 15, 20] which have surface tensions much lower than water. Materials that are both superhydrophobic and oleophobic are in high demand for many applications,[4,5,118] such as anti-biofouling[119,120] for ships, non-stick and corrosion-resistant[121-123] protective coating, self-cleaning in polluted water[42], anti-bacterial[124] coatings for cotton fabrics and microfluidics[125, 126] in lab-on-a-chip systems. To fabricate materials that are able to achieve superhydro-oleophobicity, bio-inspired micro/nano patterned structures[14, 15, 20] combined with surface energy reduction treatment[14, 15, 20] have been developed. Among those reports, fluorine compounds with a high percentage of –CF_3 and –CF_2 groups have been applied to reduce the surface tension of the patterned surface[119-126]. Table 1.1 shows some examples of the recent developments in fabrication of bio-inspired oeleophobic structures. Several surface modification approaches such as vapor deposition, liquid deposition and electrospinning are used for the fabrication of the biomimetic oleophobic materials.[19-34] Even then, plasma treatment on superhydro-oleophobic polymer surfaces may cause surface damage such as cracks,[35] and the coating approach would worsen the surface roughness and cause surface defects, ultimately reducing the oleophobicity.[127, 128]

Table 2.1 List of the bio-inspired structures, materials, surface modification techniques for the fabrication of the biomimicked oleophobic materials and the oil(s) contact angles

Biomemetic structure	Material	Surface modification technique	Oils for testing	Static contact angle (º)	Reference
Nanogrooves	Aluminum $CF_3(CF_2)mCH_2CH_2OP(=O)(OH)_2$	Dip-coating	Decane	120	25
Microholes	SiO_2, 1H, 1H, 2H, 2H-perfluorodecyltrichlorosilane	Vapor deposition	Octane	143	20
Nanofibers	PMMA, fluoro POSS	Electrospin	Hexadecane decane	110 145	20
Nanoparticle covered cotton textiles	Silica nano particle, cotton textiles, 1H, 1H, 2H, 2H-perfluorodecyltrichlorosilane	Dip-coating	Sunflower oil Hexadecane	140 135	26
Nano filament	Silicone, 1H, 1H, 2H, 2H-perfluorodecyltrichlorosilane, octadecyltrichlorosilane	Plasma treatment before vapor deposition	Hexadecane Diiodomethane	140 165	27
Nanoporous	Si, tridecafluoro-1,1,2,2,-tetrahydrooctyl trichlorosilane	Dip-coating	Diethylene glycol Hecadecane	153.4 150.7	17
Nanopores	Alumina, 1H, 1H, 2H, 2H-perfluoro-octadecyltrichlorosilane	Dip-coating under 120°C	Glycerol Diiodomethane Hexadecane Silicon oil Crude oil	158.4 155.3 153.2 150.4 155.6	28
Hierarchical microtextured structure	ZnO, water bone perfluoroalkyl metheacrylic copolymer,	Spray casting	Hydraulic oil	120 to 150	33
Micro fibers	Polyester, fluorodecyl POSS	Dip-coating	Rapeseed oil	145	30
Nanoparticles	Silica, sacrificial polystyrene, tridecafluoro-1,1,2,2,-tetrahydrooctyl trichlorosilane	UV-ozone treatment and Dip-coating	Hexadecane	70	32
Nanotube arrays	TiO_2, Ti, 1H, 1H, 2H, 2H-perfluoro-octadecyltrichlorosilane	Dip-coating	Glycerol Diiodomethane Hexadecane Colza oil Crude oil	162 165 155 157 156	24
Pyramidal structure	Si, perfluoro octyl trichlorosilane	Dip-coating	Ethylene glycol hexadecane	160 130	28
Diamond nanograss array	Polycrystalline boron-doped film, 1H, 1H, 2H, 2H-perfluorodecyltrichlorosilane	Dip-coating	hexadecane	100	13
Inverse-trapezoidal microstructure	Polydimethylsiloxane, 1H, 1H, 2H, 2H-perfluorodecyltrichlorosilane	Plasma treatment vapor deposition	methanol	135	34
Micropillars roughed with nano particels	Fluorinated 3,4-ethylenedioxypyrrole	Electro deposition	Hexadecane Sunflower oil Dodecane	144 153 135	23
Textured micropillar	Si, tridecafluoro-1, 1, 2, 2-tetrahydrooctyltrichlorosilane	Vapor deposition	hexadecane	150	21
Overhang micro pillar	Si, tridecafluoro-1, 1, 2, 2-tetrahydrooctyltrichlorosilane	Vapor deposition	hexadecane	145	21
Sol-gel nanocomposite coating	Silica, methyltriethoxysilane, perfluoroalkylmethacrylic copolymer	Blending	Ethylene glycol Lubricant oil	146.7 113.3	129
Mushroomlike micropillar	Silicon on insulator wafer, PDMS, perfluoropolyether, octafluorocyclobutane	Vapor deposition	ethanol	150 to 160	24
Overhang structure	Poly (perfluorodecylacrylate)1H, 1H, 2H, 2H-perfluorodecyl acrylate	Oxygen plasma treatment vapor deposition	Mineral oil	110	130

2.4.1. Self-cleaning Superhydro-oleophobic Materials

The comprehensive understanding of surface roughness/structure and surface energy on superhydrophobic structures inspired the development of superhydro-oleophobic structures. Among those applications, the topics relating to oil adhesion attract significant attention including topics such as bio-adhesion, microprinting, self-cleaning in oil polluted water, antifouling, oil adhesion reduction, oil transportation and oil/water separation.[119-126] Take the printed image in a printer as an example; the melted ink is supposed to print onto paper and adhere completely without adhering to the fuser roll, thereby to improve the ink using efficiency. This requires the fuser roll surface to have self-cleaning property which can be achieved by functionalizing the surface with superoleophobicity. Zhao *et al.*[121] designed a superhydro-oleophobic structure applied in paper printers, aiming to reduce the high adhesion between fuser surface and paper during the fusing process. As illustrated in Figure 2.12a, the melted toner or ink separated from the superoleophobic fuser surface without any residues left, thus improving the efficiency of printing.[121] The adhesion behavior of melted ink was compared on an oleophilic surface (oil contact angle of 63º, Figure 2.12b-f) and a superoleophobic textured micropillars surface (oil contact angle of 155º, Figure 2.12 g-k). When the ink was melted and detached from the fuser surface (Figure 2.12b-f), there was ink residue left due to the oleophobicity and strong adhesion to the fuser surface. However, the melted ink separated from the fuser surface completely without residue left (Figure 2.12g-j) indicating the superoleophobic surface had low adhesion and excellent self-cleaning properties.

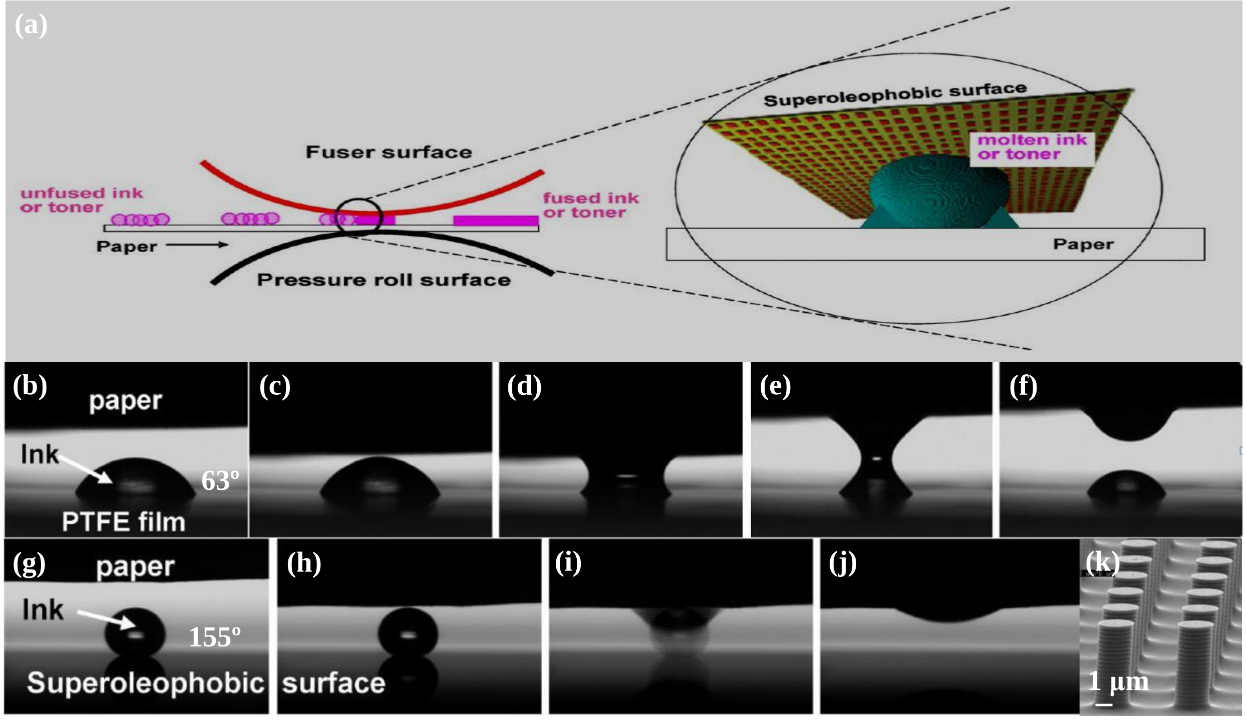

Figure 2.12. (a) Basic principle of the fuser with superhydro-oleophobic surface; (b) to (f) illustration of the interaction between paper and molten ink droplet on oleophilic PTFE substrate during printing process and part of ink was left on PTFE film without completely printed onto paper (f); (g) to (j) illustration of the interaction between paper and molted ink droplet on superoleophobic textured silicon pillars and ink was completely printed onto paper (j); (k) shows the textured superoleophobic pillar arrays used in the printing process.[121]

In addition, the superoleophobic materials play much more important roles in water/oil separation and oil transportation. In the water/oil separation industry, the common method is using membranes to separate water and oil.[131] However, most of these membranes are oleophilic with significant oil adhesion which lead to heavy oil contamination.[132] Preventing the oil from penetrating the membrane can further decrease the water/oil separation efficiency. Another example of oil adhesion can be seen in oil transportation. During transport, oil can easily form hydrates and these hydrates adhere to the walls of pipelines causing a dramatic increase in drag force, leading to a greater energy requirement for transporting the oil. To solve these problems, Yao, *et al.*[133] studied the effects of surface structures on oil adhesion reduction. The structures used in the study are shown in Figure 2.13a to c with surface treatment times of 12h, 24h and 36h, respectively. The measured water and oil contact angles were plotted in Figure 2.13d showing that both the water and oil contact angle increased with the increase of surface treatment time. The dynamic adhesion tests showed that the adhesion forces first increased and dropped suddenly after it reached the peak point (Figure 2.13e) and also showed the tendency that the adhesion forces decreased with increase oleophobicity which matched the results in Figure 2.13f. These results indicate that superoleophobic materials can be used to reduce oil adhesion.

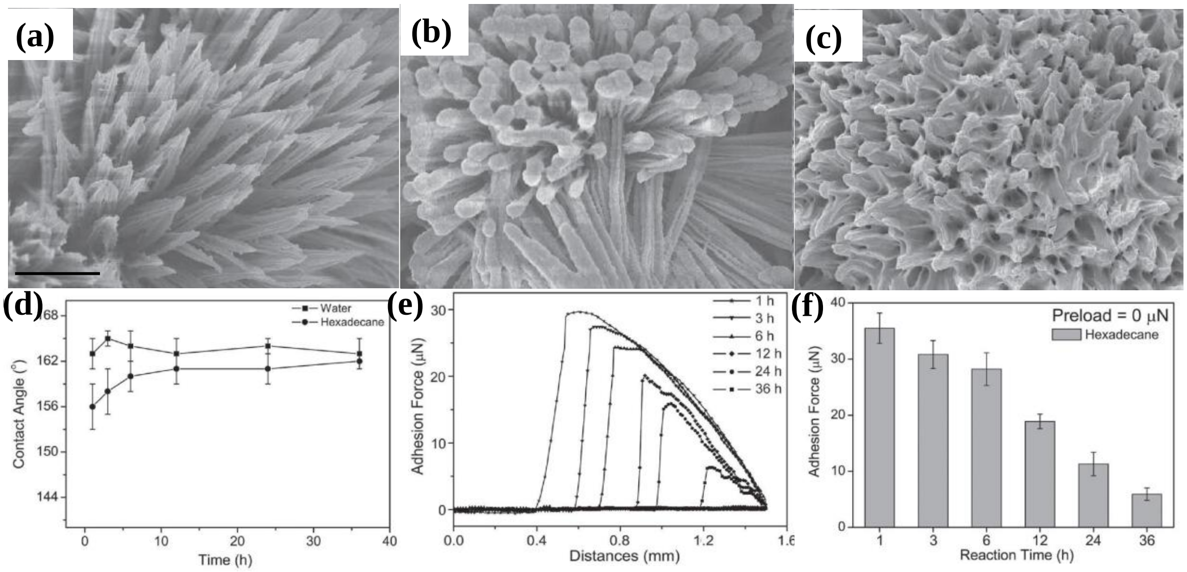

Figure 2.13. Surface morphologies of prepared nanostructures with different surface treatment time of (a) 12h, (b) 24h and (c) 36h; (d) the water and oil contact angles on varied surfaces showing superhydro-oleophobicity; (e) dynamic adhesion measurement showing the adhesion forces decrease with the increased oloephobicity at longer reaction time; (f) the adhesion forces of hexadecane at the zero preload decreased with increasing oleophobicity.[133]

2.4. 2. Superhydro-oleophobic Materials with Electrical Conductivity

Superhydro-oleophobic materials show excellent water/oil repellence property; so they can protect the surface from oil, bacteria, and dust contaminations resulting in clean surface. Thus, superhydro-oleophobic materials are well studied and applied in the areas of self-cleaning, anticorrosion and antifouling. However, most superhydro-oleophobic materials are not electrically conductive, which restricts their applications in the fields of conductive materials such as skin sensors, electrically controlled or signal collecting systems, radiofrequency antennas and lab-on-a-chip systems,[134-140] which play important roles in everyday life and industry activities. In some cases, conductive materials with well machined micro/nano structures are required, which could not be achieved with metallic materials. For instance, Wang *et al.*[137] reported a robust, conductive and superhydro-oleophobic composites fabricated by vapour polymerization of 3,4-ethylenedioxythiophene (EDOT) on fluoropolymer-modified fabrics, showing a water contact angle of 169° and a hexadecane contact angle of 156°. However, the conductivity of this fabricated superhydro-oleophobic materials was low (the conductivity was about 1×10^{-3} S/m). In a following research, Wang *et al.*[138] developed a simpler procedure of one-step vapor deposition of conductive coatings on the structured surfaces to deliver the conductive and superhydro-oleophobicity.[136]

PDMS is widely used in academia and industry for fabricating superhydro-oleophobic bio-inspired structures such as inverse-trapezoidal microstructures, hierarchical PDMS micropillar/nanohairs, *etc.*,[139] since it is non-toxic, hydrophobic, flexible, biocompatible, and chemically and thermally stable.[140] Although PDMS is an insulating material, its properties of biocompatibility, stretchability, chemical stability, and hydrophobicity make it a promising candidate which could be modified as a conductive and stretchable material.[140]

Cong and Pan reported PDMS-Ag conductive composites that were fabricated *via* photolithography technique.[139] Figure 2.14a shows the microstructure of PDMS-Ag conductive composites from which the Ag grooves were well aligned on PDMS substrate with a pitch value of around 100 μm.[139] The resistance of the composites decreased with increasing content of Ag fillers. As can be seen in Figure 2.14b, stable conductivity of 5×10^3 S/m was obtained when the volume concentration of Ag reached 19 vol%.[139] Figure 2.14c shows a micrograph of the rough surface of PDMS based conductive composites filled with over 80 wt% of Ag flakes added into (Ag flakes shown in the inset image); the conductivity of the PDMS-Ag conductive composite increase with the increasing of Ag flakes content and the threshold of the conductivity was 83 wt% (Figure 2.14d).[140] For carbon black reinforced PDMS, a similar trend was observed but with a much lower threshold concentration and smaller percentage of carbon flakes(Figure 2.14d).[140] Even though using more Ag flakes can remarkably increase the conductivity, which is 3 orders lager than the carbon black reinforced PDMS composites, the large amount of conductive fillers negatively affects the mechanical performance of the composites such as stiffness, brittleness, and difficulty with fabricating micro/nanostructures.[140]

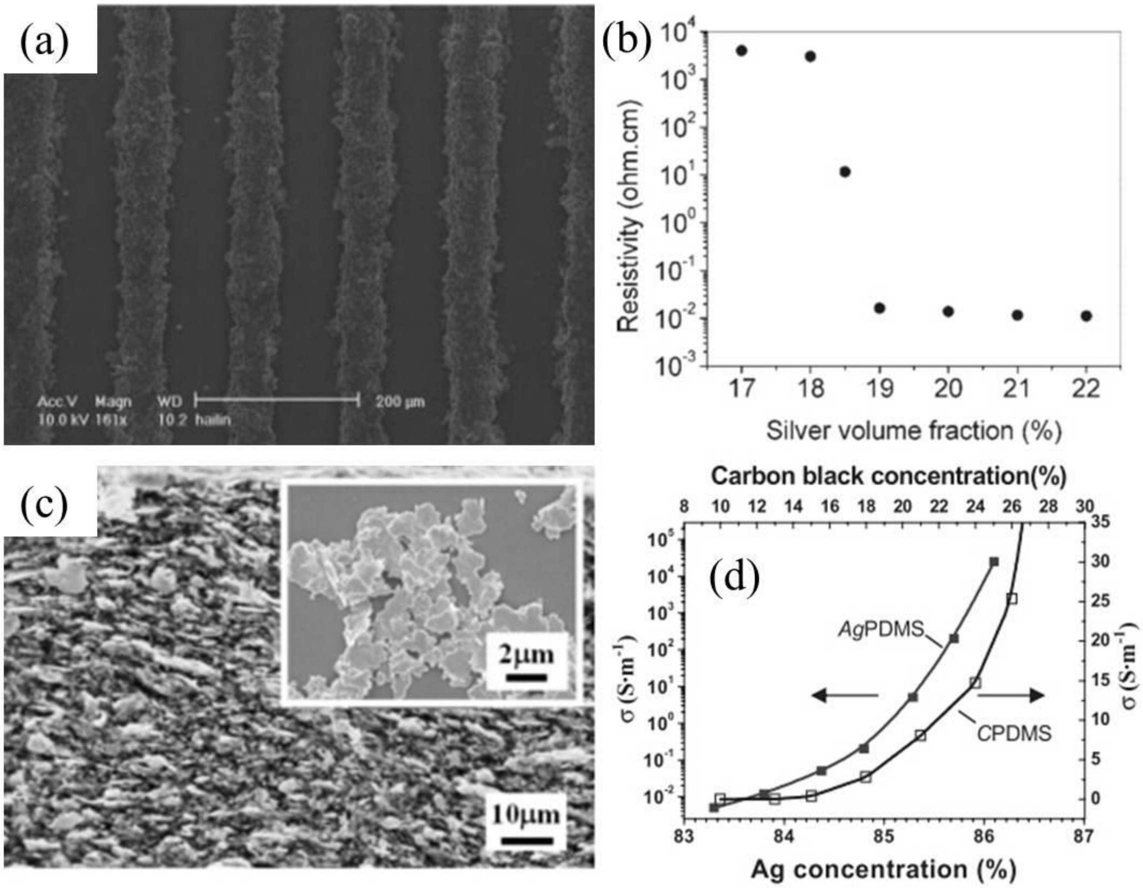

Figure 2.14 (a) the fabricated PDMS-Ag composite with microstructure ~100 µm;[139] (b) the resistance measurement of the obtained sample showed that the resistance reached a stable level when the content of Ag was 19 vol%;[139] (c) microimage of PDMS-Ag composite (Ag: 84 wt%);[140] (d) the conductivity of Ag and carbon black reinforced PDMS.[140]

Xu and Zhu[134] reported a coating approach of silver nanowires (SNWs) on PDMS surface, as showed in Figure 2.15a. First, silver nanowires were cast and dried onto silica substrate and then PDMS elastomer solution was poured onto the dried SNWs layer. The PDMS bonded SNWs were peeled off from the Si substrate after PDMS was cured. The obtained PDMS-SNWs thin film showed that the SNWs were embedded into PDMS forming a dense Ag layer on the PDMS surface (Figure 2.15b).[134] Stretch tests and conductivity tests indicated that the resistance increased with the increasing strain (Figure 2.15c).[134] The first stretching circle implied that the resistance had a linear correlation with strain (Figure 2.15c), but the linear correlation is not shown in the second stretching cycle.[134] Besides, the fabricated surface was smooth and oleophilic which restricts the application in oil species environment.

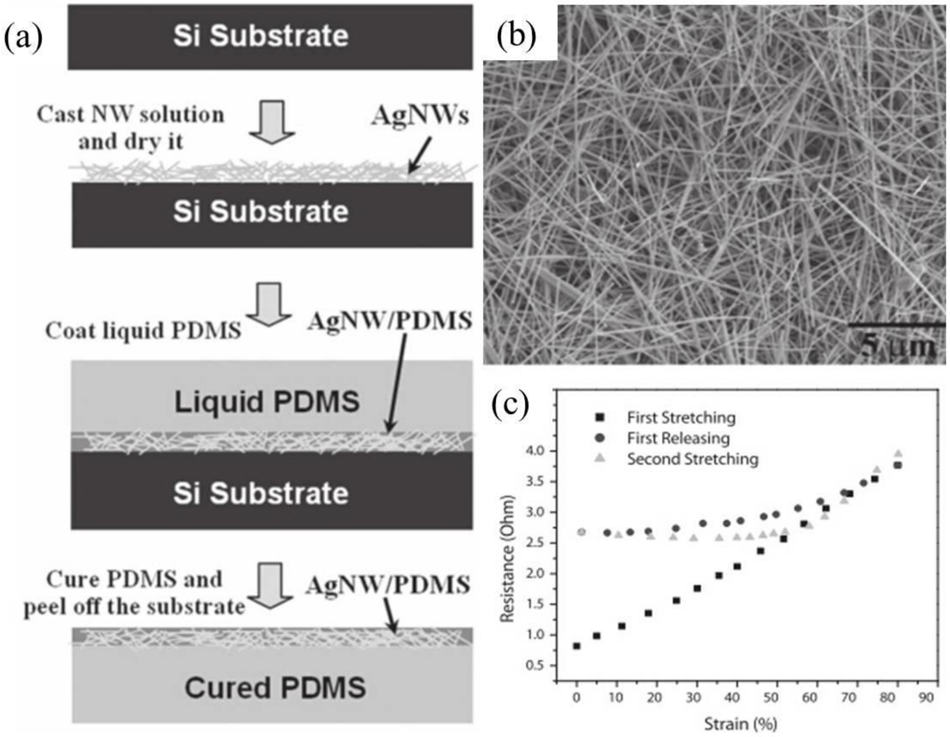

Figure 2.15. (a) the schematic of fabrication PDMS-Ag nanowire conductive composite; (b) micrograph of the obtained PDMS-Ag nanowire surface and (c) the conductivity and stretch test.[134]

Chen *et al.*[83] reported a graphene foam (GF) fabricated *via* chemical vapor deposition method (CVD). As shown in Figure 2.16 a-f, the nickel foam was selected as the template and CH_4 was deposited on nickel foam at 1000 °C to form graphene. A thin film of PMMA was then deposited onto the foam to support graphene and then treated with $FeCl_3$/HCl to remove the nickel. Hot acetone solution was used to dissolve PMMA, followed by deposition of PDMS. The conductivity of GF and GF/PDMS was measured as a function of the number of graphene layers. Figure 2.16g indicated that the highest conductivity was achieved using a graphene mass concentration of 0.8 % with 5 layers.

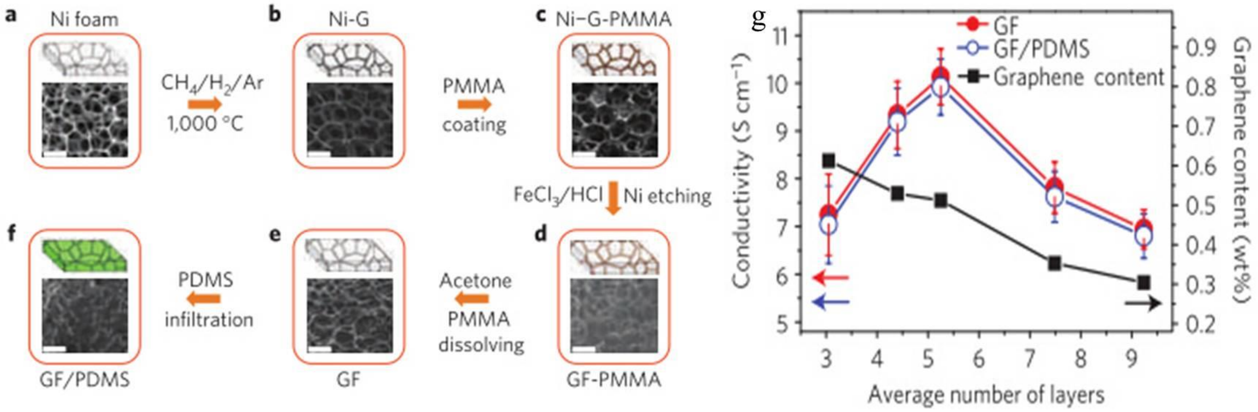

Figure 2.16. (a-f) the schematic of GF/PDMS fabrication; (g) the conductivity of GF/PDMS as a function of the number of graphene layer.[83]

Carbon nanofiber (CNF) reinforced fluoroacrylic co-polymer nanocomposites were fabricated by Das *et al*.[141] The effectiveness of CNFs on the conductivity and superoleophobicity of the nanocomposites was studied. The oleophobicity of the nanocomposites changed from oleophobic at a concentration of 10 wt% (CNFs) to superoleophobic at 60 wt%. The oil contact angle hysteresis (9°) was small at high CNFs concentrations (higher than 40 wt%), while the nanocomposites surface showed strong adhesion to oils at low concentrations of CNFs (10 wt% and 20 wt%). The low oil contact angle hysteresis indicated that the surface had remarkable self-cleaning property. The conductivity of the nanocomposites reached as high as 1×10^3 S/m at a concentration of 60 wt%. Figure 2.17a is the low magnification micrograph of CNFs reinforced fluoroacylic co-polymer (PMC) showing a rough surface, which is beneficial to enhance the oleophobicity. From the high magnification SEM image (Figure 2.17b), it was found that the CNFs formed condensed network pathways for electron transportation inside the electrical network.

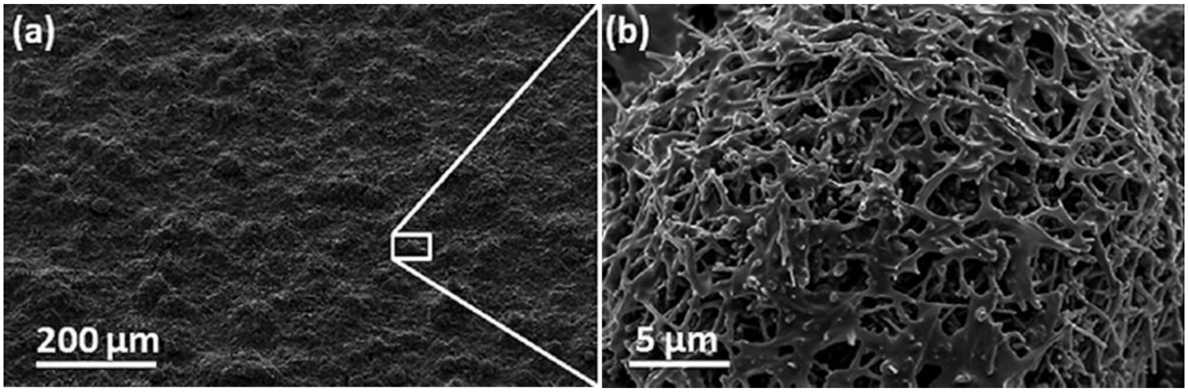

Figure 2.17. (a) Low magnification surface structure of carbon nano fibers reinforced PMS nanocomposites; (b) the high magnification SEM image of nanocomposites surface.[141]

2.5 Strategies to Eliminate Frozen Oil

Oil adhesion has attracted extensive studies over the past decades due to its important role in many industrial applications such as lubrication, lithographic etching, anticontamination *etc*.[176-179] Ambient temperature behaviors on varied surfaces ranging from oleophilic to superoleophobic have been well investigated. However, there is a lack of understanding of the low temperature behavior, especially when the oil is frozen at sub-zero (Celsius) temperatures. Such low-temperature phenomena are very important in scenarios such as oil freezing in engines or in oil transport pipelines, where the freezing leads to a dramatic increase in adhesive force, requiring substantial amounts of energy to overcome, potentially causing instrument failure as well.[43-47] Since there is limited literature on the adhesion between frozen oil and micropatterned surfaces, it is informative to review the work of ice adhesion reduction. Many efforts have been devoted to exploring possible strategies to remove ice from surfaces, which can all be categorized into either passive strategies or active strategies.[51-53]

2.5.1 Passive Strategy

The passive strategy is implemented either by controlling the surface wettability to reduce the ice adhesion or by applying mechanical forces to remove the accumulated ice.[51-53] This is because superhydrophobic surfaces can be used to delay the ice formation and reduce the contact area thereby reducing the shear forces between the ice and substrates. Davis *et al.*[57] studied the effects of wettability on ice adhesion reduction (Figure 2.18). The experiment set-up is shown in Figure 2.18a, where the ice was formed at -20 ºC and was removed using high pressure compressed air. Figure 2.18b presents the wettability of the as-prepared samples including the static contact angle, dynamic contact angle, contact angle hysteresis (CAH) and rolling-off angle. Their effects on ice adhesion reduction are shown in Figure 2.18c, from which it can be seen that the ice adhesion is reduced significantly with increasing water contact angle and decreasing contact angle hysteresis. However, such tests are only applicable to laboratory research; the practical application of using superhydrophobic coatings alone is not an ideal method and mechanical elimination is difficult to conduct on a large scale in real world/industrial applications.

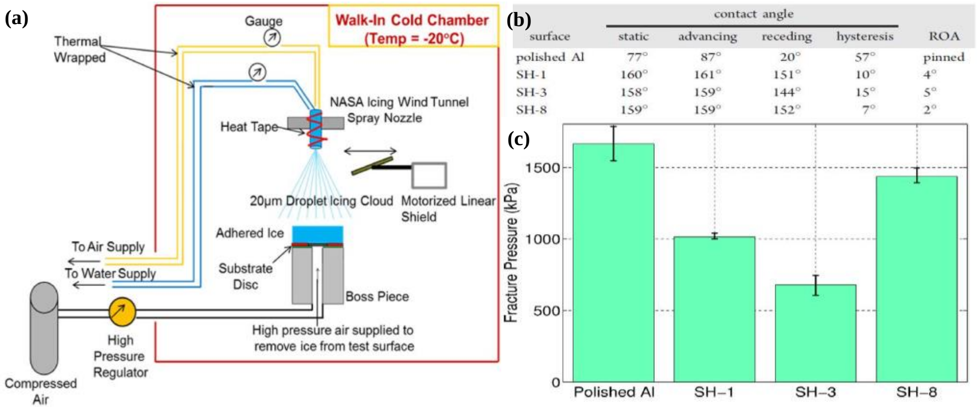

surface	contact angle				ROA
	static	advancing	receding	hysteresis	
polished Al	77°	87°	20°	57°	pinned
SH-1	160°	161°	151°	10°	4°
SH-3	158°	159°	144°	15°	5°
SH-8	159°	159°	152°	7°	2°

Figure 2.18. (a) schematic set-up of ice adhesion test; (b) the wettability of tested samples; (c) the ice fracture pressure on varied surfaces with different wettability.[57]

2.5.2 Active Strategy

The active strategy employs external energy such as thermal, chemical or pneumatic to eliminate the accumulated ice.[204,207,208] Among these methods, thermal melting uses sources such as warm air or electrical current and is regarded as one of the most effective ways to remove ice.[204,207,208] One decade-old traditional approach is warm air melting, in which intense warm air was blown onto the objects through a special tube.[51-53] This raises the temperature of the system quickly, resulting in the melting of ice.[204] However, this requires large consumption of energy at low temperatures and is more difficult to operate in an environment with strong winds present. Currently, electrical joule heating is widely utilized due to its lower energy cost and easy operation.[58-60] An example of the application of this method is given in Figure 2.19.[58] In figure 2.19a, the conductor wires were surrounded with thick ice. A significant amount of ice was melted by applying electrical current for certain times (Figure 2.19b). Figure 2.19c illustrates the increase of surface temperature with the prolonged time of the applied current, indicating the high efficiency of conductors for heating.[58]

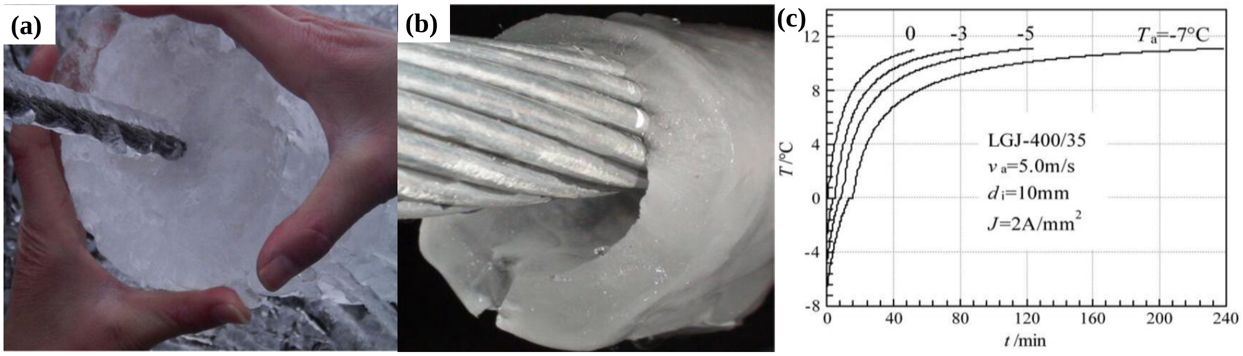

Figure 2.19. (a) ice accumulated on conductor wires; (b) the ice that surrounded the conductor wires melted after certain time of electrical current heating; (c) bottom temperature of conductors.[58]

Chapter 3. Superhydro-oleophobic Bio-inspired Polydimethylsiloxane Micropillared Surface via FDTS Coating/Blending Approaches

3.1 Introduction

Superhydrophobic materials have attracted extensive interests in the past decades.[13, 14, 26, 142] By mimicking the micro/nano surface structures from the nature, such as lotus leaf,[14, 142, 143] superhydrophobic materials with micro/nano surface structures (e.g. grooves,[143] nanoparticles,[26] nanoporous,[17] or pillars [14, 142]) have been developed as potential self-cleaning materials[142-144] in anti-icing,[15, 16] erosion prevention[17, 144] and friction/drag reduction[113] applications. Nevertheless, materials only with superhydrophobicity are usually not feasible because they can easily be contaminated by organic oily species[8, 20, 24] where surface tension is much lower than water. Hence, materials that are both superhydrobicity and oleophobicity are in high demand in many applications such as anti-biofouling[119, 120] for ships, anti-sticking/corrosion[145, 146] protective coating, self-cleaning in polluted water[145-147] and microfluidics[148].

To achieve superhydro-oleophobicity, bio-inspired micro/nano patterned structures[149] combined with surface energy reduction treatment[150-152] have been developed. Normally, the trapped air in the gaps of patterned surfaces restrains the spread of a water droplet, causing it to bead up, but the low surface tension of oil (surface tension is around 20-30 mJ/m^2 while surface tension of water is 72.8 mJ/m^2) would wet the patterned surface by breaking the air-pillar barrier and flow into the gaps[12, 30, 33]. In order to achieve superhydro-oleophobicity, fluorine compound with a high percentage of $-CF_3$ and $-CF_2$ groups have been applied to reduce the surface tension of the patterned surface[145, 148, 153]. The most widely reported technique to fabricate oleophobic

---

* This chapter has been published in *Applied Surface Science* **2015**, *324*, 612-620.

materials is to deposit a self-assembled monolayer (SAM) of fluorocarbon onto the patterned surface through vapor deposition[153-155]. For instance, Zhao et al[153] coated fluorosilane FOTD on silicon micropillars by vapor deposition and obtained a highly oleophobic surface. In the report of Darmanin, fluorinated 3,4-ethylenedioxypyrrole (EDOP) was electrodeposited on nano particle over-hang structure with hexadecane contact angle of 132º. [154]

Polydimethylsiloxane (PDMS) is a soft and hydrophobic material which is easily to fabricate different structures[133, 154]. With these properties PDMS have been widely studied in the research area of self-cleaning[34], microfluidic channel[131], drag reduction[146, 155] and many other applications. For instance, Liu et al[146] utilized the PDMS to duplicate fish scale structure and then was deemed as second template to prepare oleophobic materials by a casting technique. Im et al[34] achieved oleophobicity by the vapor deposition of tridecafluoro-1, 1, 2, 2-tetra-hydrooctyl trichlorosilane on PDMS inverse trapedoids with methanol contact angle of 135º. However, one main limitation of vapor deposition perfluorocarbon on structure surface to fabricate oleophobic material is that the fluorocarbon tends to form aggregates (normally tens of nano meters thickness) and structural defects such as disordered tail structure or domain boundaries[156-158]. These aggregates and defects often negatively impact the performance of the material[35]. For example, perfluorodecyltrichlorosilane (FDTS) deposited on to the surface can form aggregates such as micelle or lamellar, leading to the degradation of anti-wetting properties and premature delamination of FDTS coating.[156]

In this work, we reported superhydro-oleophobic PDMS micropillar surfaces which were fabricated through trichloro (1*H*, 1*H*, 2*H*, 2*H*-perfluorooctyl) silane (FDTS) modification in two approaches. Blending a small amount of FDTS in PDMS precursor making superhydro-oleophobic PDMS micropillars (oil contact angle ~ 141°) is reported for the first time to the best knowledge of the authors. Oleophobicity of the common approach where FDTS was deposited as coating on PDMS micropillar samples by vapor deposition approach were fabricated to have an oil contact angle of 115°. The segregation of FDTS from bulk PDMS to the surface showed a smooth surface whereas the coated FDTS on PDMS micropillar induced rough surface and structure defects causing the reduction of oleophobicity. The influence of FDTS on PDMS micropillar superhydro-oleophobicity has been studied and the results showed the superhydro-oelophobicity kept a stable tendency as more FDTS was blended into PDMS.

3.2 Experimental

3.2.1 Materials

Trichloro (1*H*, 1*H*, 2*H*, 2*H*-perfluorooctyl) silane (FDTS, 97% Sigma–Aldrich Chemicals, USA), and polydimethylsiloxane (PDMS, Sylgard 184 Dow Corning Co., USA,) were used to make the superhydro-olephobic materials. The negative master mold of micropillars was fabricated on silicon wafer using a negative SU-8 photoresist (SU-8-25, MicrochemCo., Newton, MA, USA). Arrays of micropillar (14 mm × 14 mm in size) were prepared with pillars of 15 μm in diameter, 45 μm in height and 32.5 μm of center–center spacing. Diiodomethane (99%, Sigma–Aldrich Chemicals, USA), dimethyl sulfoxide (DMSO, ≥99.8%, Caledon Laboratories LTD.), ethylene glycol (≥99.5%, Sigma–Aldrich Chemicals, USA), formamide (≥99%, Sigma–Aldrich Chemicals, USA), glycerol (≥99%, Sigma–Aldrich Chemicals, USA), *n*-hexadecane (99%, Sigma–Aldrich Chemicals, USA), automatic transmission fluid (ATF, The National Association for Stock Car Auto Racing Inc., USA) and DI water (lab provided) were used as the probing liquids in contact angle measurements and surface tension calculations. The surface tension and the components of the liquids used in this research were listed in Table 3.1.

Table 3.1 Surface tension and its components of the liquids in this experiment

Surface tension (mJ/m^2)	γ_{LW}	γ_{AB}	γ^+	γ^-	γ (mJ/m^2)
Diiodomethane	50.8	0.0	0.0	0.0	50.8
DMSO	36	8.0	0.5	32	44
Ethylene glycol	29	19.0	1.92	47	48
Formamide	39	19.0	2.28	39.6	58
Glycerol	34	30.0	3.92	57.4	64
Hexadecane	27.5	0.0	0.0	0.0	27.5
Water	21.8	51.0	25.5	25.5	72.8

3.2.2 Fabrication

Six types of PDMS specimens have been fabricated and listed in Table 3.2. Sample 1: neat flat PDMS; sample 2: FDTS-coated flat PDMS; sample 3: FDTS-blended flat PDMS; sample 4: PDMS micropillar; sample 5: FDTS-coated PDMS micropillar; sample 6: FDTS-blended PDMS micropillar. In a typical experiment, the PDMS base was mixed with its curing agent with a weight ratio of 10:1. The mixture was poured onto a silicon wafer to make flat samples (about 1.2–1.3 mm thickness and 45 cm^2 in area) and on a silicon negative mold to make micropillared samples. Each sample was fully degassed before they were put into oven to cure at 90 °C for 1 h. Once cured, the micropillared PDMS films were gently peeled from the silicon negative mold. To coat FDTS on PDMS samples, a thin layer of FDTS were deposited onto the surface of PDMS samples by vaporizing 50 μl of FDTS solution per PDMS sample in a sealed container (diameter: 140 mm, height: 20 mm, the density of coated FDTS is 2.14 g/m^2) at 70 °C for 2 h. Note that no plasma treatment of the PDMS was made because of the possible instability and roughening/damage of plasma-treated surface even though it may enhance the surface reactivity with the FDTS.[127, 128]. To blend FDTS into PDMS, a certain quantity of FDTS was added into the PDMS solution with varied FDTS/PDMS weight percentage: 0, 0.57%, 1.42%, 2.27%, 3.12% and 3.97%. The mixtures were stirred, fully degassed and poured onto glass slide and silicon negative mold respectively. These samples were put into oven to cure at 100 °C for 30 min after fully degassed.

Table 3.2 A list of samples: flat, micropillared, with and without FDTS modification by coating and blending.

Flat		Micropillar	
Sample 1	Neat	Sample 4	Neat
Sample 2	FDTS coated	Sample 5	FDTS coated
Sample 3	FDTS blended	Sample 6	FDTS blended

3.2.3 Characterization

Field emission scanning electron microscopy (FE-SEM, LEO-Ultra, GEMINI, Germany) was used to examine the FDTS-modified PDMS micropillars. Fourier transform infrared spectroscopy (FTIR, Tensor 27, LN-MCT detector, diamond crystal, PIKE Technologies, USA) was used to analyze the -CF_2 and -CF_3 groups in FDTS-blended PDMS micropillar. The surface roughness of FDTS-coated/blended flat PDMS were measured by an optical profiler (MFP-D WLI 3D surface profilometer, Rtec Instruments Inc., USA) and AFM (Digital Instruments 3100), respectively. X-ray Photo-electron Spectroscopy (XPS, monochromatic Al Ka X-ray source, Thermo Scientific Alpha) was used to analyze the atomic composi- tion at the surface and the cross-section. Water and oil static contact angle measurements were performed by a sessile drop system in ambient environment at room temperature as illustrated in Figure 3.1. The liquid was dispensed with a micro size needle (New Era Pump Systems Inc.) through a syringe pump in shape of droplets with volume of 5 μl. Measurements were carried out in ambient environment at room temperature after the droplet settled for 5 s. The contact angle was measured by fitting the profile using a custom- made LabVIEW program.

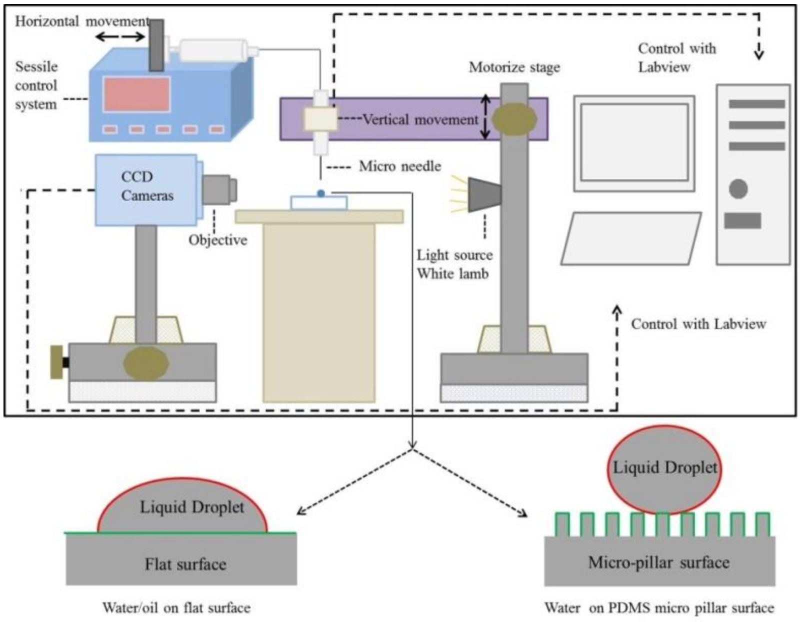

Figure 3.1 Schematic illustration of the contact angle measurement system and hydro/oleophilic state (left bottom) and superhydro/oleophobic state (right bottom) on FDTS-modified PDMS micropillared surface.

3.3 Results and Discussion

3.3.1 FDTS-functionalized PDMS Micropillars

Neat and FDTS-modified PDMS micropillars were fabricated using our previously developed mold transfer method.[113, 159] The prepared PDMS micropillars are 15 µm in diameter, 45 µm in height with 32.5 µm center–center spacing. This gives the micropillars an aspect ratio of 3 (the value of height divided by the diameter) to avoid the collapse of micropillars. Both the neat and FDTS-blended PDMS micropillar samples can be easily peeled from the negative template after curing. The addition of FDTS to the PDMS by either blending or coating has negligible effects on the global structure of the micropillars (Figure 3.2a and b). However, the surface qualities of individual FDTS-modified micropillars are different. The surface of FDTS-blended micropillars is smooth as shown in Figure 3.2c. In contrast, the individual micropillar coated with FDTS by vapor deposition has rough surfaces and contains many bumps (Figure 3.2d). Thus, the blending method appears to be more efficient in terms of maintaining the original smooth surface.

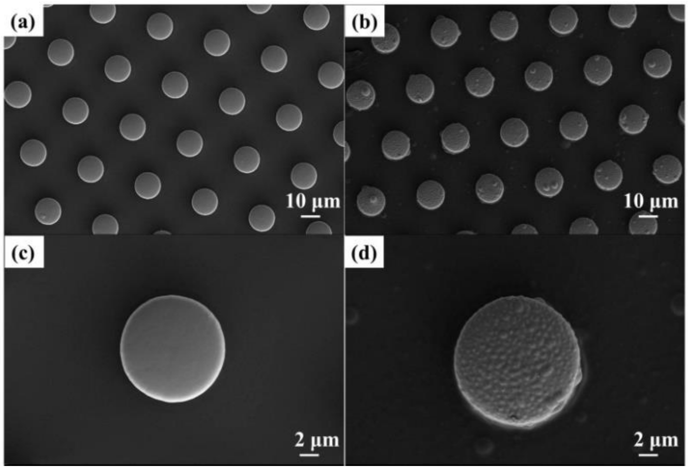

Figure 3.2. The global structure of FDTS blended PDMS micropillar (a) and FDTS coated PDMS micropillar (b); and the individual micropillar of FDTS blended PDMS micropillar (c) and FDTS coated PDMS micropillar (d).

The surface morphology of FDTS-coated flat surface was examined by SEM (Figure 3.3a) showing the same type of bumps on the surface as observed on FDTS-coated PDMS micropillars. The aggregation of FDTS caused the structure defects such as the generated of nanocracks on the surface in Figure 3.3b. The roughness measurements were measured by optical profilometry for FDTS-coated surface (sample 2) and AFM for FDTS-blended surface (sample 3). Figure 3.3c is the 3D image of the FDTS-coated PDMS surface showing the significant surface roughness. Surface roughness is obtained by a selected area of 0.24 mm × 0.24 mm at the center of the image (Figure 3.3d). The average roughness of the selected area is 0.433 µm. The measured roughness is consistent with the SEM observation of FDTS-coated PDMS micropillars.

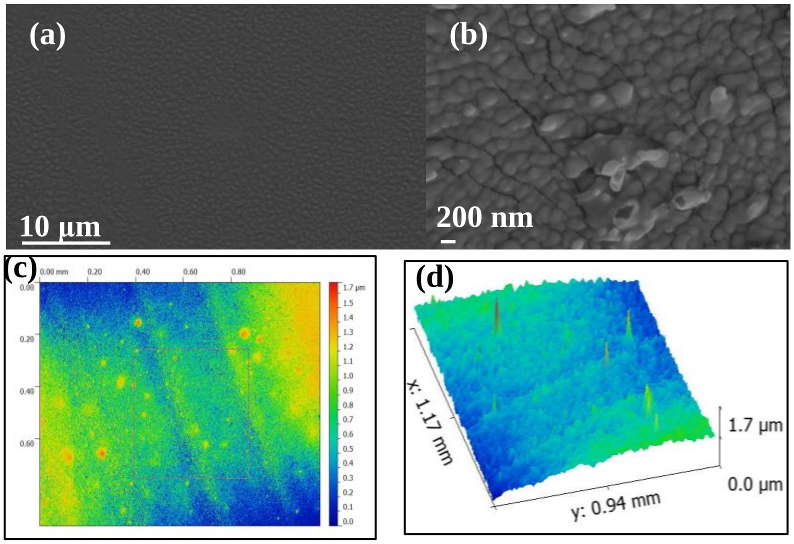

Figure 3.3. SEM image of FDTS coated flat PDMS (a); nanocracks on FDTS coated PDMS surface (b); 3-D image of FDTS coated flat PDMS surface (c) and the surface roughness measurement (d).

As the SEM image has shown that the surface of FDTS-blended flat PDMS is smooth (Figure 3.4a). AFM was applied to examine the surface of the FDTS-blended flat PDMS sample and was displayed in Figure 3.4b. The average roughness of FDTS-blended PDMS flat sample was determined to be 2.43 nm (indicated by the selected area). The roughness measurement revealed that coating FDTS on PDMS by vapor deposition showed obvious surface roughness whereas FDTS blended into PDMS has a negligible effect on surface roughness. Likely, the rough surface is caused by the aggregation of FDTS during the vapor deposition process[35, 157]. In the presence of water moisture during the vapor deposition process the terminal chorosilane groups of FDTS would react with water to form the OH groups; and, the OH groups can aggregate together or aggregate to the Si-compound surface making the surface rough.[156]

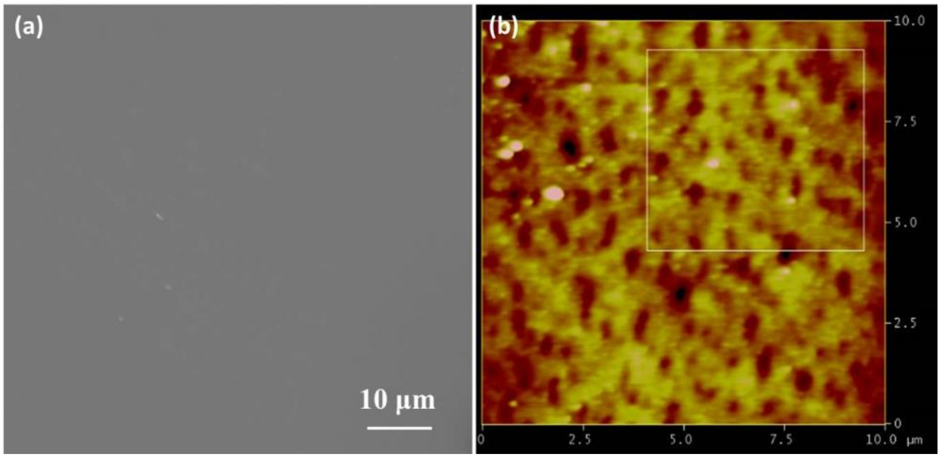

Figure 3.4. FDTS blended PDMS flat surface SEM image (a); typical AFM image of FDTS blended flat PDMS surface (b), the sqaured area is used to estimate surface roughness.

FTIR was employed to verify the existence of functional groups ($–CF_2$ and $–CF_3$) on the surfaces of FDTS-coated/blended PDMS micropillar (Figure 3.5). There is a strong peak near 1084 cm^{-1} for both FDTS modified PDMS, corresponding to $–CF_3$ symmetric stretching mode. The peaks near 774 cm^{-1}, 735 cm^{-1} and 553 cm^{-1} corresponding to $–CF_2$ scissoring mode, $–CF_2$ symmetric stretching mode and $–CF_2$ bending mode are also observed in the spectra of both FDTS-coated/blended PDMS micropillar samples.[160,161] Further examination of the spectra revealed some differences between the two methods of FDTS modifications. The –CF_2 symmetric mode of FDTS-coated PDMS micropillar is at the peak of 1197 cm^{-1}; and –CF_3–CF_2 asymmetric deformation appears at the peaks of 1376 cm^{-1} and 1408 cm^{-1}.[160,161] In contrast, there are no similar peaks in FDTS-blended PDMS at the same spots of spectra. The most significant difference between the coated and blended samples is the peaks associated with H_2O in FDTS coated PDMS.[37] Presumably some water vapor might have deposited on the surface during the process of FDTS vapor deposition on PDMS surface. This unintentional deposition of H_2O on the surface of FDTS coated PDMS may influence the wetting properties of the samples as studied in the following sections.

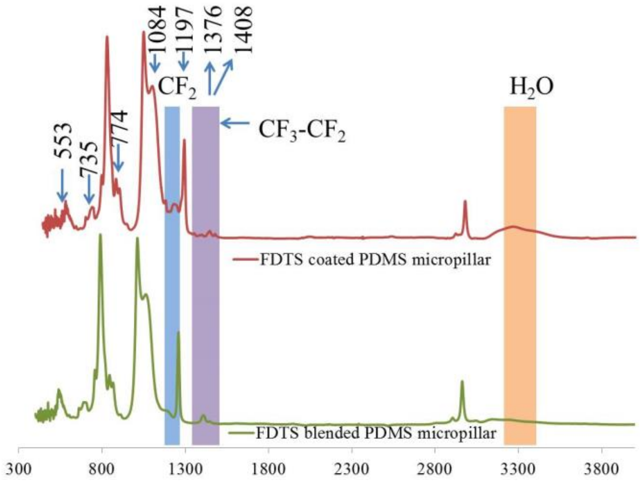

Figure 3.5. FTIR spectra of FDTS coated PDMS micropillar and FDTS blended PDMS micropillar samples.

3.3.2 Hydrophobicity and oleophobicity

Hydrophobicity and oelophobicity of three types of micropillared surfaces (sample 4: neat PDMS micropillar, sample 5: FDTS-coated PDMS micropillar; sample 6: FDTS-blended PDMS micropillar) and the control flat surfaces (sample 1: neat flat PDMS; sample 2: FDTS-coated flat

PDMS and sample 3: FDTS-blended flat PDMS) were first evaluated by examining the contact angle of water, n-hexadecane and commercial auto transmission fluid oil droplets on these surfaces. The flat PDMS is moderately hydrophobic, showing an average water contact angle of 103° (Figure 3.61a). The hydrophobicity of FDTS coated/blended flat PDMS (Figure 3.6 b-c) are comparable and have water contact angles of 115° and 119°, respectively. The change in surface structure by making micropillars significantly increased the water contact angle, rendering the surface superhydrophobicity (Figure 3.6 d-e). In contrast to the hydrophobicity, the PDMS is oleophilic, having a small hexadecane contact angle of 28° (Figure 3.6f). The addition of FDTS increased the contact angle by 39° for coated one and 43° for blended one (Figure 3.6g, h), but still relatively oleophilic; the addition of micropillars to FDTS blended PDMS changed the surface to be oleophobic, having an n-hexadecane contact angle of 98° for FDTS coated pillar (Figure 3.6i) and 130° for FDTS blended pillar (Figure 3.6j). We also examined auto transmission fluid (ATF) contact angle on both flat and micropillar surface of neat PDMS and FDTS coated/blended PDMS (Figure 3.6 k-o). The results followed the similar trends as n-hexadecane which further verified the oleophobic effect of both adding FDTS and creation of micropillars on PDMS surfaces.

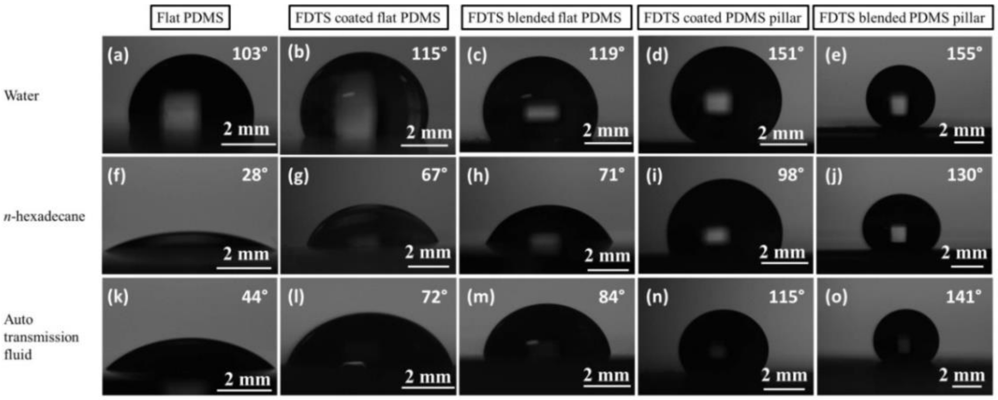

Figure 3.6. Microscope images of water contact angles on neat flat PDMS (a); FDTS coated flat PDMS (b); FDTS blended flat PDMS (c); FDTS coated PDMS micropillar (d) and FDTS blended PDMS microplillar (e); the contact angles of *n*-hexadecane and auto transmission fluid were performed on the same samples and were shown in (f-j) and (k-o), respectively.

A series of water and oils contact angle measurements were performed to quantitatively characterize the observed hydrophobity and oleophobicity of the FDTS coated/blended micropillars. Additional measurements were performed on the flat control samples to provide mechanistic studies by applying the classical Wenzel[11] and Cassie-Baxter theory[12]. Assuming the liquid completely wets the surface, the Wenzel model recognizes that textured surface increases the available surface area of the solid, which modifies the surface contact angle according to Equation 3.1:[11]

$$\cos\theta^* = r\cos\theta_C \qquad \text{Equation 3.1}$$

where θ_C and θ^* are equilibrium contact angle and the apparent contact angle on the textured surface, respectively; r is a roughness factor defined as the ratio of the actual area over the apparent area which can be calculated from Equation 3.2 for arrays of micropillars in a hexagonal configuration used in this work.[159]

$$r = \frac{4\pi Rh}{\sqrt{3}CC^2} + 1 \qquad \text{Equation 3.2}$$

R, h and *CC* denote the micro pillars' radius, height and center-to-center spacing, respectively.

The Cassie-Baxter theory considers both the wetted and non-wetted areas and proposed the effective contact angle is related to the contact angle on the flat surface by the following equation[12]

$$\cos\theta^* = -1 + \Phi_S(1 + \cos\theta) \qquad \text{Equation 3.3}$$

where Φ_S is defined as the fraction of solid-liquid interface[36]

$$\Phi_S = \frac{\text{textured area}}{\text{whole area}} = \frac{2}{\sqrt{3}}\frac{\pi R^2}{CC^2} \qquad \text{Equation 3.4}$$

Both models were applied to our system. It was found that only the Cassie-Baxter model is applicable to the micropillar surfaces. The contact angles of water and oils on both FDTS-coated and blended samples were shown in Figure 3.7. The predicted contact angles from equation 3.3 are also presented to examine how well the Cassie-Baxter model fits the experimental values so as to obtain insights into the wetting mechanisms for FDTS modified micropillar surfaces. Figure 3.7a shows the water contact angles on the flat and micropillar surfaces and the calculated contact angles from Cassie-Baxter equations. Creating micropillars on PDMS surface significantly enhanced the hydrophobicity which is reflected by water contact angles (both are higher than 150°) in Figure 3.7a. The water contact angles on both FDTS coated/blended micropillar samples are very similar and well predicted by the Cassie-Baxter model. The results indicate that coating and blending FDTS had negligible difference on their ability to alter the water contact angles. The contact angles of *n*-hexadecane on flat FDTS-modified flat/micropillar surface are displayed in Figure 3.7b. The contact angles of *n*-hexadecane on FDTS modified flat samples (sample 2 and sample 3) are 67°and 71°, suggesting the blending FDTS has almost the same effects on oleophobicity as the coating FDTS. It is interesting to note that *n*-hexadecane contact angle on FDTS coated PDMS micropillar is 98° (Figure 3.7b). Higher *n*-hexadecane contact angle (130°) is obtained on FDTS blended PDMS micropillar indicating that the better effectiveness of enhancing oleophobicity is achieved by blending FDTS in PDMS. When Cassie-Baxter model is applied to predict the *n*-hexadecane contact angles on sample 5 and sample 6, the results are calculated as 139° and 140°, which are similar to the experimental contact angles of the blended pillars but larger than the contact angle on the coated samples. The results showed that the theory over-estimated the contact angles of oils likely because of the structure defects of

FDTS coated micropillare surface.[156] SEM image of FDTS coated PDMS showed that there were many micro bumps dispersed on the surface with nanocracks after FDTS coating. Figure 3.7c shows the contact angles of ATF on flat FDTS-modified surface and micro-pillared surface and the predicted effective contact angles from the Cassie-Baster model. The trends are similar to Figure 3.7b, further confirming the effectiveness of blending FDTS for improving oleophobicity. Overall, both the experimental contact angles of water and oils on the FDTS blended PDMS micropillared surfaces follow the Cassie-Baxter theory well. On the other hand, the Cassie-Baxter model only predicted the experimental contact angles of water on FDTS coated PDMS micropillar surface. It did not predict the contact angle of oils on the FDTS coated micropillar surface.

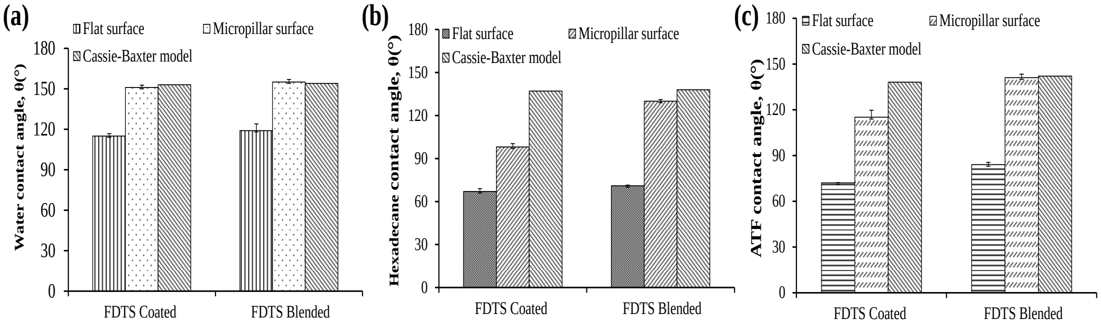

Figure 3.7. (a) Comparison of experimental average water contact angles and model-prediction results of the prepared PDMS; (b) Comparison of experimental average *n*-hexadecane contact angles and model-prediction results of the prepared PDMS; (c) Comparison of experimental average ATF contact angles and model-prediction results of the prepared PDMS.

3.2.3 Effects of FDTS surface segregation

The above analysis shows the blending had a similar or even better effect than vapor deposition of FDTS on improving the oleophobicity of PDMS. Considering FDTS has lower surface energy than PDMS[162], there might be a surface segregation of FDTS in the system. When they are mixed together, the material with lower surface tension prefers to migrate to the surfaces to minimize the free energy of the whole system, leading to the enrichment of low surface tension polymer in the inter-surface.[162, 163] Figure 3.8a illustrates that a layer of FDTS forms at the air-PDMS interface because of the surface segregation. The driving force for this phenomenon is the difference in the surface tension of the two mixing components described by the modified Gibbs-Duhem theory for the system at a non-equilibrium state[162]:

$$\mathrm{d}(\mathrm{n_r}\mu_\mathrm{r}) + \mathrm{d}(\mathrm{n_f}\mu_\mathrm{f}) = -\mathrm{A}\mathrm{d}\gamma = \mathrm{A}(\gamma_\mathrm{r} - \gamma_\mathrm{f})\mathrm{d}\emptyset_{\mathrm{s,f}} \qquad \text{Equation 3.5}$$

where chemical potential of PDMS and FDTS can be μ_r and μ_f, respectively; nr and nf represent the moles of PDMS and FDTS; A is the surface area, γ_r, γ_f and $d\phi_{s,f}$ represent PDMS surface tension, surface tension of FDTS and the changes of FDTS surface fraction. The value of $A\ (\gamma_r - \gamma_f)$ determines the migration of the additives. If it is positive, the low surface tension component would spontaneously migrate to the surfaces to reduce the energy of the whole system[162,163] (Figure 3.8). In our system, the surface energy of PDMS is 21.9 mJ/m^2, which is higher than the surface energy of FDTS (about 15 mJ/m^2).[164, 165] The surface area of the flat samples maintained a constant value during the blending and curing process. As a result, the value of $A\ (\gamma_r - \gamma_f)$ is positive resulting in the spontaneous migration of FDTS into the surface.

To verify this hypothesis, we measured the surface atomic concentrations of neat flat PDMS (sample 1), flat PDMS coated FDTS (sample 2) and flat PDMS blended FDTS (sample 3) by XPS analyses. Figure 3.8b is the typical XPS spectra of FDTS-coated and FDTS-blended PDMS, and a neat PDMS surface as the control. To examine the possible migration of FDTS, we also analyzed the cross-section of FDTS-blended PDMS sample. As expected, there is a significant fluorine peak at 700 eV for both the FDTS coated and blended surface while the control sample did not show any fluorine peaks.[129,166,167] It is informative to notice that the cross-section of sample 3 shows only a weak peak of fluorine whereas the peak of fluorine on FDTS-blended surface (sample 3) is as strong as that FDTS-coated PDMS (sample 2).

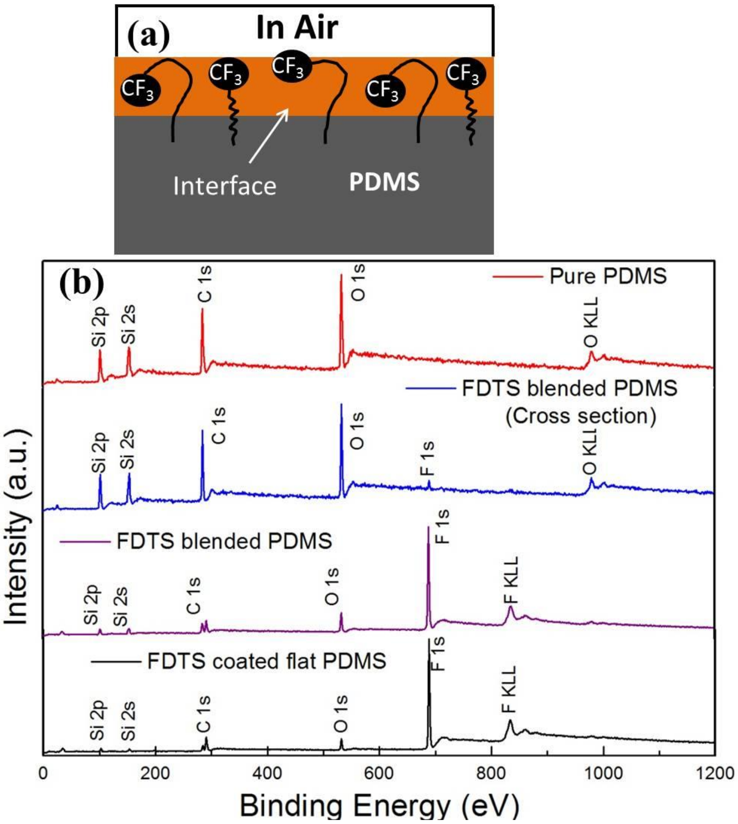

Figure 3.8. (a) the blended FDTS migrates to the surface of PDMS after cured; (b) the surface elements composition analysis by XPS.

The atomic compositions of each sample are calculated and tabulated in Table 3.3. The control neat PDMS (sample 1) has 45.82% carbon, 26.29% oxygen, 27.79% silicon. For FDTS coated sample (sample 2), the content of fluorine is 53.49%. The fluorine concentration at the surface of FDTS blended PDMS is 44.04% with only 1.66% was detected at the cross-section. This confirmed that the blended FDTS in PDMS indeed migrate to the surface. Here the fluorine weight fraction concentration is calculated in equation 3.6 to compare the concentration of fluorine on the surface:

$$c_i^{wt} = \frac{c_i \times A_i}{\sum_{i=1}^{n} c_i \times A_i}$$ Equation 3.6

c_i^{wt} is the weight fraction concentration of element i, c_i is the mole fraction of element i, A_i is the relative atomic mass of element i. The calculated results showed the weight fraction concertration of fluorine on FDTS coated and blended PDMS surface were 60.33% and 48.49%, respectively. As the XPS scanning area and depth were the same on FDTS coated and blended PDMS samples, the calculated results indicate the fluorine on FDTS coated PDMS is more than FDTS blended PDMS.

Table 3.3 XPS analysis of the atomic composition of samples 1-3.

Sample ID	C1s	F1s	O1s	Si2p
Sample 1 (Surface)	45.82 ± 0.98	0	26.29 ± 1.05	27.79 ± 0.09
Sample 2 (surface)	34.17 ± 0.26	53.49 ± 0.51	7.27 ± 0.34	5.07 ± 0.27
Sample 3 (Surface)	33.68 ± 0.22	44.04 ± 1.09	11.44 ± 0.57	10.84 ± 0.46
Sample 3 cross-side	44.16 ± 0.27	1.66 ± 0.27	25.65 ± 0.74	28.54 ± 0.65

In order to determine how much of the surface energy has been reduced by the addition of FDTS to the surface, the surface energy of the FDTS coated/blended flat PDMS samples were estimated using Wu's theory.[168] Wu's theory divides the liquid into polar and non-polar components. Contact angle is related to the dispersive and polar components of surface energy by equation 3.7.

$$\frac{\sigma_L(cos\theta+1)}{4}=\left[\frac{\sigma_S^D\sigma_L^D}{(\sigma_S^D+\sigma_L^D)}+\frac{\sigma_S^P\sigma_L^P}{(\sigma_S^P+\sigma_L^P)}\right] \qquad \text{Equation 3.7}$$

σ_L is the total surface tension of liquid, θ is the contact angle of the liquid on the substrate, σ_L^D and σ_L^P are dispersive and polar component of liquid, σ_S^D and σ_S^P are dispersive and polar component of the solid substrate, σ_S is the overall surface tension of the solid. The liquids and the dispersive and polar components value which were used for calculation surface tension are listed in Table 3.1 and the contact angles (Table 3.4) were obtained to calculate the surface energy.

Table 3.4 The contact angle of the liquids which were used to calculate the surface energies.

Contact angle	PDMS θ (°)	FDTS coated flat PDMS θ (°)	FDTS blended flat PDMS θ (°)
Diiodomethane	70 ± 3.77	90 ± 3.56	95 ± 3.17
DMSO	73 ± 1.36	86 ± 6.22	92 ± 4.39
Ethylene glycol	90 ± 2.80	96 ± 5.57	100 ± 2.92
Formamide	97 ± 3.15	104 ± 5.14	105 ± 2.02
Glycerol	105 ± 3.99	116 ± 4.88	120 ± 5.09
Hexadecane	28 ± 0.37	67 ± 2.03	71 ± 0.46
Water	103 ± 0.45	115 ± 1.76	119 ± 4.97

Based on Wu's theory, the calculated the surface tension of neat flat PDMS, FDTS coated flat PDMS and FDTS blended flat PDMS (Table 3.5) are 21.9 mJ/m^2, 16.7 mJ/m^2 and 14.9 mJ/m^2, respectively. The overall surface tension of FDTS blended flat PDMS is almost the same as FDTS coated flat PDMS. The dispersive components of sample 2 and sample 3 are 15.8

mJ/m^2 and 14.0 mJ/m^2, which are also close. The same conclusion can be obtained by comparing the polar component. van Oss theory[169,170] was further utilized to identify the surface tension differences as it divides surface tension into dispersive, acid and basic components (Equation 3.8).

$$\sigma_L(cos\theta + 1) = 2\left[(\sigma_S^D \sigma_L^D)^{1/2} + (\sigma_S^- \sigma_L^+)^{1/2} + (\sigma_S^+ \sigma_L^-)^{1/2}\right] \qquad \text{Equation 3.8}$$

σ_L is the overall surface tension of liquid, θ is the contact angle of the liquid on the solid surface, σ_S^D and σ_L^D are dispersive component of the solid and liquid, σ_S^+ and σ_S^- are acid and base components of the solid substrate, σ_S is the overall surface tension of the solid, and σ_L^+ and σ_L^- are acid and base components of the liquid. The results of neat flat PDMS (sample 1), FDTS coated flat PDMS (sample 2) and FDTS blended flat PDMS (sample 3) (Table 3.5) are 28.0 mJ/m^2, 13.9 mJ/m^2 and 11.8 mJ/m^2, respectively. Though the overall surface tensions of sample 2 and sample 3 remains similar, the base component of FDTS coated PDMS (1.2 mJ/m^2) is two times larger than FDTS blended PDMS (0.61 mJ/m^2). The higher value of base component indicates a strong propensity to form polar interactions between PDMS and the liquids. These analyses suggested that a small disparity of surface tension between flat PDMS coated FDTS and flat PDMS blended FDTS led to a pronounced difference in oil contact angles.

Table 3.5 The effective surface tesions and their components of the samples 1, 2 and 3 caculated by van Oss theory and Wu's theory.

Surface tension (mJ/m^2)	γ_{disperse}	γ_{polar}	γ^{+} (acid)	γ^{-} (base)	γ_{total} (mJ/m^2)
Neat PDMS (Sample 1) van Oss	23.7 ± 0.77	4.3 ± 2.57	1.1 ± 0.89	4.4 ± 1.90	28.0 ± 3.34
Neat PDMS (Sample 1) Wu's	16.8 ± 7.58	5.1 ± 3.24			21.9 ± 4.44
PDMS coated FDTS(Sample 2) van Oss	12.8 ± 0.46	1.1 ± 0.91	0.35 ± 0.33	1.2 ± 0.96	13.9 ± 1.34
PDMS coated FDTS(Sample 2) Wu's	15.8 ± 1.09	0.9 ± 0.44			16.7 ± 7.24
PDMS blended FDTS (Sample 3) van Oss	11.0 ± 0.66	0.84 ± 0.98	0.31 ± 0.3	0.61 ± 0.71	11.8 ± 1.81
PDMS blended FDTS (Sample 3) Wu's	14.0 ± 1.1	0.9 ± 0.45			14.9 ± 0.73

We also investigated the effect of the quantity of FDTS on hydrophobicity and oleophobicity. Six different weight ratios of FDTS/PDMS have been tested. Figure 3.9 plots the contact angles of water, ATF and *n*-hexadecane as a function of the quantity of blended FDTS. Water contact angles do not change much with the increasing of the amount of FDTS. In contrast, a small amount FDTS in PDMS can cause enormous enhancement in terms of the oil contact angles; the oil contact angles are zero for no FDTS and are 68° and 91° at weight ratio of 0.57% for *n*-hexadecane and ATF, respectively. The highest contact angle occurs at the weight ratio of 1.42%. After this point the contact angle shows a stable trend when more FDTS is added. This suggests that the weight ratio of 1.42% FDTS is sufficient to saturate the surface with high oleophobicity. Thus a relative small amount of FDTS in the blend is enough to obtain the desired oleopheobicity; adding more FDTS did not improve further.[171]

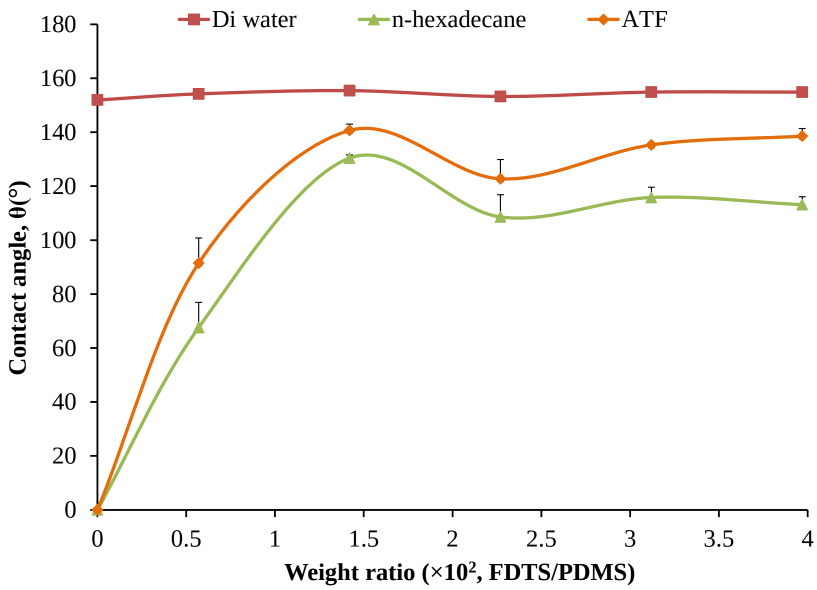

Figure 3.9. Superhydro-oleophobicity of varied weight ratios of blended FDTS/PDMS micropillar reflected by contact angles (water, *n*-hexadecane and ATF).

Finally, it is worthwhile to discuss some advantages of the FDTS blending method in comparison with the common vapor deposition method. First, the blending method has the desirable feature to maintain the original surface roughness while enhancing surface oleophobicity; but the vapor deposition method makes the surface rough. Second, the blending FDTS into PDMS do not require high temperature to vaporize FDTS and do not require extra enclosure to retain FDTS vapor. Third, only a finite amount of FDTS is required to saturate the surface and deliver significant enhancement of oelophobicity. It is also desirable but difficult to make quantitative comparison of the molecular efficiency of the FDTS of the two methods because of the unknown distribution of FDTS in the bulk (or thickness-direction) of the blended PDMS and uneven distribution of vapor-deposited FDTS on the surface. Overall, we may state that the blending FDTS into PDMS is an effective alternative way and work better than the direct vapor deposition to make the hydrophobic but oleophilic PDMS micropillars superhydrophobic and superoelophobic.

3.4 Conclusions

The intrinsically hydrophobic but oleophilic surface of PDMS elastomer were successfully modified to be superhydro-oleophobic by surface patterning and functionalization with FDTS. Two types of FDTS modifications were investigated: direct vapor deposition of FDTS on PDMS surface and blending FDTS into the PDMS precursor. It was found the blending approach is more effective than the coating methods for improving the oleophobicity. FTIR results indicated that both the functional groups of -CF_2 and -CF_3 existed on the surfaces of FDTS modified PDMS samples ensuring the surface of FDTS blended PDMS micropillar was oleophobic. The surface tensions of the two type samples were calculated by Wu’s theory and van Oss theory indicating that the FDTS blended PDMS shows lower surface tension than FDTS coated ones especially for the base component. The FDTS coated PDMS surface showed obvious surface roughness whereas FDTS blended PDMS maintained the smoothness. The XPS analyses indicated that the blended FDTS migrated to the surface owing to the surface segregation and maintained surface smooth. Thus, we can conclude that blending FDTS into PDMS works better than the direct coating FDTS on PDMS surface; the micropillar made from FDTS-blended PDMS has smooth surface and have better oil repellent property than the rough FDTS coated surface via vapor deposition.

Chapter 4. Oleophobicity of Biomimetic Micro-patterned Surface and Its Effect on the Adhesion of Frozen Oil

4.1 Introduction

Micropatterned surfaces mimicking biological systems such as lotus leaf with superhydrophobic and self-cleaning properties, have been studied extensively in the past decades.[1, 2, 7, 172, 173] These studies have shown that the surface energy reduction and surface patterning can be both applied to the design of surperhydrophobic materials.[11,12] Superhydrophbic materials are widely used in the applications of anticontamination, antifouling, antifogging, anti-icing etc.[1, 2, 7, 172, 173] However, such materials are easily wetted by oily liquids to lose their functions, significantly restricting their potential applications.[20, 42, 174] Consequently, finely engineered surfaces with utmost resistance to both water and oil are becoming increasingly important in practical engineering.[20] The design of oleophobic surfaces follows the same principles of fabricating superhydrophobic surfaces with a particular emphasis on the reduction of surface energy in combination with surface patterning.[20, 25] It is reported that $–CF_2$ and $–CF_3$ functional groups have a very low surface tension thereby the use of fluoropolymers can reduce the surface energy and adhesion between liquid/solid surface.[20, 25] Also, the trapped air-pockets in the patterned structures can prevent the penetration of the liquids resulting in superoleophobicity.[12, 20] Thus far, fluoropolymer modified micro/nano structured superoleophobic surfaces (nano/micro hierarchical structure[20], micropillars[174] etc.) have been developed; their oleophobic behaviors and adhesion properties have been studied at room temperature.[175, 176]

---

*This chapter has been published in *Langmuuir* **2015**, *31*, 9901-9910.

Oil adhesion is an important topic due to its involvement in many industry applications[24,41,176-179], such as anti-contamination,[20] and lithographically etching[41]. It depends on both of the surface morphologies[41] and surface composition[179], and is a phenomenon closely related to the hydro/oleophobicity.[48,115] From the thermodynamic point of view, eliminating a liquid from its solid substrate requires the energy to overcome the adhesion.[48,115] The basic relation between the work of adhesion and surface wettability is given by the Dupre-Yong equation[48]

$$W_e = \gamma_{lv}(1 + cos\theta_e) \qquad \text{Equation 4.1}$$

in which, W_e is the work of adhesion at the equilibrium state, γ_{lv} is the surface tension of the liquid and θ_e is the equilibrium contact angle (CA). At a large equilibrium CA, it requires a small amount of work to remove droplets; however, in many applications, there is often a finite contact angle hysteresis (CAH); the receding CA is more directly related to the separation of a liquid droplet other than the equilibrium CA.[180-182] Thus, equation 2 has been used to predict the work of adhesion to separate the liquid from the surface in terms of the receding CA[48]:

$$W_p = \gamma_{lv}(1 + cos\theta_{rec}) \qquad \text{Equation 4.2}$$

In contrast with many research activities on the oil adhesion on varied surfaces ranging from oleophilic to superoleophobic surfaces at room temperatures, the low temperature behaviors of superoleophobic materials are not well studied, especially when the oil is frozen under a frigid environment, but such low-temperature phenomena play important roles in engineering applications. Examples include oils in motor engines and oil transportation in pipelines in the cold region.[43-47] The oils stuck to or froze on the pipeline wall, leading to a large drag force and surface corrosion.[44-46] In practice, the adhesion between a frozen liquid and its substrate is commonly evaluated in terms of adhesion energy or strength measured from mechanical tests such as shearing tests and knock-off tests.[183,184] The thermodynamic equations 4.1 and 4.2 have also been utilized to predict the adhesion energy required to remove the frozen liquid from solid surfaces.[48,115]

Because there is little literature on the adhesion between frozen oil and micropatterned surfaces, it is informative to briefly review the recent work of the anti-icing and ice adhesion.[49,50,57,93,185] Many efforts have been devoted to investigating the possible utilization of hydrophobic surface for the reduction of ice accumulation and adhesion.[180-182] It is reported that superhydrophobic surfaces with proper structures could delay the ice accumulation by postponing the formation of ice nucleation.[49,50] Guo et al.[50] successfully fabricated hierarchical nano/microstructure where the ice accumulation was detected after 7000 s. In terms of the reduction of ice adhesion strength, a close relationship was found that the ice adhesion strength could be reduced by increasing the hydrophobicity and decreasing the CAH of the material.[180-182] In particular, superhydrophobic surfaces have been reported to have low ice adhesion strength.[183,184] Davis et al.[57] reported that ice adhesion on nanostructured superhydrophobic surfaces was only one-third of that on the superhydrophilic surface. In general, the effects of surface structures on ice adhesion have been attributed to the facts that the nano/microstructure provides a large number of voids to prevent the formation of interlocks between water and substrate so as to have a small contact area and low adhesion strength.[93] Furthermore, the thermodynamic relationship between wettability and ice adhesion has been studied by Meuler et al.[48]; they found that the ice adhesion was significantly reduced by decreasing the receding CAs; however the effects of micropatterning on the relation between adhesion strength of frozen liquid and the liquid CA or work of adhesion are still not well understood, limiting the possible prediction of practical strength from the principle of thermodynamics and surface parameters.

We report the oil repellency behavior of micropatterned PDMS surfaces, which was applied as a model system and explore the influences of the oleophobicity on the adhesive strength of frozen oil droplets at –25 °C; one particular objective was to examine how the surface patterning influence the relationship between the measured adhesion and the thermodynamic work of adhesion calculated from CA measurements. Five different surfaces were fabricated to reveal the relationships between oleophobicity and the frozen oil adhesion strength. To the best of the authors' knowledge, it is the first time that the frozen oil adhesion behavior has been symmetrically investigated on the surfaces with different structures and oleophobicity (ranging from oleophilicity to superoleophobicity). The results show that surface patterning significantly shifted the correlation between the measured adhesion and thermodynamic work of adhesion, and there is a possible synergic effect of low surface energy of micropatterning on the reduction of adhesion strength of frozen oil droplets.

4.2 Experimental

4.2.1. Materials

Trichloro (1*H*, 1*H*, 2*H*, 2*H*-perfluorooctyl silane (FDTS, $CF_3(CF_2)_7(CH_2)_2SiCl_3$, 97%, Sigma-Aldrich Chemicals, USA), polydimethylsiloxane (PDMS: $(C_2H_6OSi)_n$, Sylgard 184, Dow Corning USA), and sylgard 184 silicone elastomer curing agent (Dow Corning Co. USA) were used as received. Different parameters of silicon wafers with microholes (SU-8-25, Microchem, Newton, MA, USA) were utilized as the mold to transfer the microstructures. A flat and smooth silicon wafer was used to prepare flat surfaces. Diiodomethane (CH_2I_2, 99%, freezing point: 5.4°C, Sigma-Aldrich Chemicals, USA) was used as the probing oil for CA measurements and frozen oil adhesion strength test.

4.2.2. Sample Fabrication

In this study, PDMS samples of different oleophobicities have been prepared using the procedures reported in our previous work[172]: oleophilic neat flat PDMS (sample 1), oleophobic FDTS blended flat PDMS (sample 2: 1.42 wt% of FDTS), superoleophobic FDTS blended PDMS micropillars with different parameters (samples 3-5, 1.42 wt% of FDTS). The dimension of the prepared sample is 14 mm × 14 mm with 3 mm thickness. The parameters of the fabricated samples are listed in Table 4.1. Three superoleophobic FDTS blended PDMS micropillars were fabricated by varying only the height or aspect ratio of the micropillars whereas the diameters (15 μm) and center-center-space (32.5 μm) of the micropillars are the same.

Table 4.1 List of samples of varied surface modification and micropillar structures

Sample ID	Materials	Surface modification	Structural parameters of the micropillars			
			diameter (μm)	height (μm)	center-center space (μm)	aspect ratio
1	PDMS	flat				
2	FDTS/PDMS blend	flat				
3	FDTS/PDMS blend	micro-patterned	15	22.5	32.5	1.5
4	FDTS/PDMS blend	micro-patterned	15	45	32.5	3.0
5	FDTS/PDMS blend	micro-patterned	15	68	32.5	4.5

4.2.3. Characterization

An optical profilometer (MFP-D WLI 3D surface profilometer, Rtec Instruments) was used to compare the surface roughness and structures of flat samples (sample 1 and sample 2). The overall structures of the prepared periodic micropillars arrays were observed by field emission scanning electron microscopy (FE-SEM, LEO-Ultra, GEMINI, Germany). All of the samples were deposited with a thin layer of Au (thickness is estimated to be 40 nm) to enhance conductivity of the micropillars before SEM testing.

4.2.4. Wettability Measurement

Surface wettability was characterized by measuring the static CAs, advancing, receding angles and CAH. Diiodomethane was used as the probing oil in contact angle measurements. CAs (on all samples) were obtained by placing 10 μL of diiodomethane on the flat/micropillar surfaces using an auto pipette (Fisher Scientific). The CAH was measured by the common tilting method.[20,21] During the tilting process, one end of the glass slide was kept immobile and the other side was raised gradually with a tilting rate of 1°/s. The advancing and receding CAs were recorded when the droplet started to roll down as the glass slide was gradually tilted. CAH was calculated from the discrepancy between advancing and receding contact angles. Measurements were carried out in ambient environment at room temperature after the droplet settled for 5 seconds. The CAs and sliding-off angles were recorded using an optical contact angle system. The CA was calculated by fitting profiles using a custom-made LabVIEW program. CA measurements were performed on three different spots of each specimen; at least three specimens were measured for each sample.

4.2.5. Frozen Oil Adhesion Strength Test

The frozen oil adhesion measurements were performed on oleophilic, oleophobic and superoleophobic surfaces by using a custom-build cooling system. Figure 4.1a illustrates the system, which has three main parts: (I) a Universal Materials Tester (UMT, UNMT-2MT, by Center for Tribological dimensions: 28.0 cm × 53.0 cm × 65.0 cm) used to control the movement of a steel plate probe (9 mm in length, 6 mm width and 0.96 mm in thickness) to knock off the frozen oil droplet and obtain the adhesion forces, (II) a coolant circulating system consisting of a temperature controller (ranging from -20 to 100 °C, Thermo Scientific C10, dimensions: 10.0 cm × 17.0 cm × 16.0 cm) as well as a coolant container and pump (Thermo Scientific K10, dimensions: 19.0 cm × 35.0 cm × 37.0 cm) to supply circulating coolant (antifreeze, Recohem) to cool a thermoelectric cooling chamber, and (III) a thermoelectric cooling chamber (able to reach as low as –40 °C) (model 1198E925, Horus, Techmologies dimensions: 16.5 cm × 12.5 cm × 8.0 cm) consisting a Peltier plate surrounded with insulating silicon foam walls to achieve a steady temperature of –25 °C. Figure 4.1b illustrates the mechanism of the thermoelectric cooling system. The operating principle of the thermoelectric cooling plate is based on the Peltier effect that revolves around the conductivity discrepancy between the two sides. When voltage is applied on the two different conductors, temperature difference between the top and bottom sides is generated: the low temperature is achieved on the top side, while heat from the bottom hot side is taken away by the coolant.

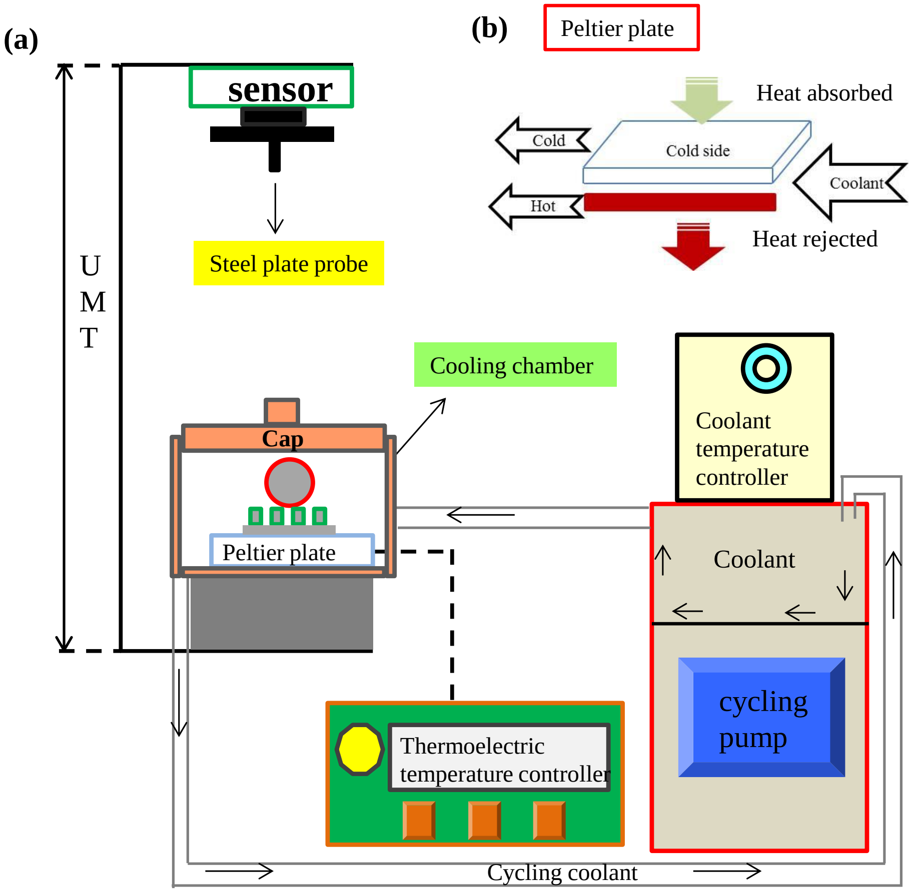

Figure 4.1. (a) schematic illustration of the experimental setup of the frozen oil knock-off test and (b) the thermoelectric Peltier plate system.

The sample was tightly attached onto the Peltier plate and then a 10 μL droplet of diiodomethane was deposited to freeze the oil droplet (Figure 4.1). After that, the whole system was cooled using the cooling system on the surface (Figure 4.1a). In this study, the freezing temperature was set to –25 °C and the holding/freezing time was 30 min. The adhesion forces of frozen oil droplets were obtained by measuring the knock-off forces. The steps of performing the knock-off test are as follows: (i) The steel probe was moved down to touch the substrate beside the frozen oil droplet. The probe was held stationary for 10 s to cool to the same temperature as the droplet. (ii) The probe was lifted up slightly to have a gap distance of 0.1 mm between the probe and substrate surface to avoid scratching the substrate surface. (iii) The steel plate probe was moved laterally to touch the side of the droplet and knock-off the frozen oil droplet with a speed of 0.1 mm/s. The effect of freezing time on the knock-off forces was performed on sample 4 with a variety of times: 30, 40, 60 and 90 min. The knock-off tests were repeated on four to five specimens for each sample.

4.3. Results and Discussion

4.3.1. Sample Fabrication and Oleophobicity Characterization

Surface energy and roughness are two crucial factors of surface wettability. The blended FDTS in PDMS migrated into the surface of prepared samples and reduced the surface energy to14.9 mN/m^2, as reported in our previous work. The effect of FDTS on surface geometry was investigated by optical profilometry. The 3D surface profiles of sample 1 and sample 2 are shown in Figure 4.2a and b, respectively. The arithmetic mean surface roughness (R_a) and root mean square roughness (R_q) are the widely used parameters to describe the surface height variation.[185] The values of R_a and R_q for sample 1 are 25.9 and 32.5 nm, which are slightly lower than those for sample 2 (with R_a and R_q of 36.1 and 45.6 nm, respectively). This result indicates the surface of sample 2 has more peaks and valleys than sample 1, which can be attributed to the migration of FDTS to the surface.[174]

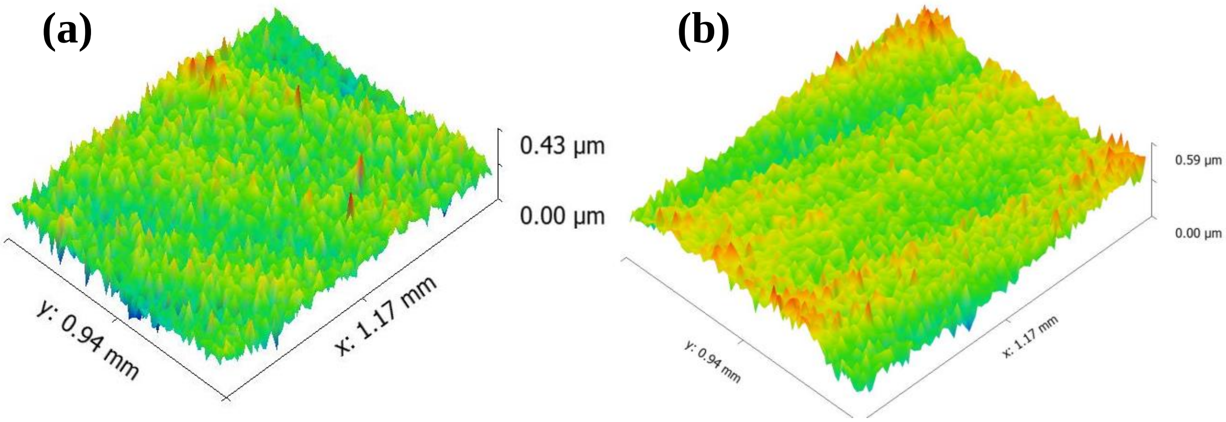

Figure 4.2. (a) 3D surface profiles of the sample 1 and (b) 3D surface profiles of the sample 2.

FDTS blended PDMS micropillars were fabricated *via* a mold transfer method. Figure 4.3 shows the microstructures of the fabricated three types of the FDTS blended PDMS micropillars. Figure 4.3 a-c is the top view of the sample 3, 4 and 5 while Figure 4. 3 d-f are the side-view images of the sample 3-5, respectively. These top-view and side-view micrographs of the samples showed that the micropillars for all samples were well organized, as expected. These micropillars made of the FDTS blended PDMS were expected to have varying degrees of oleophobicity.

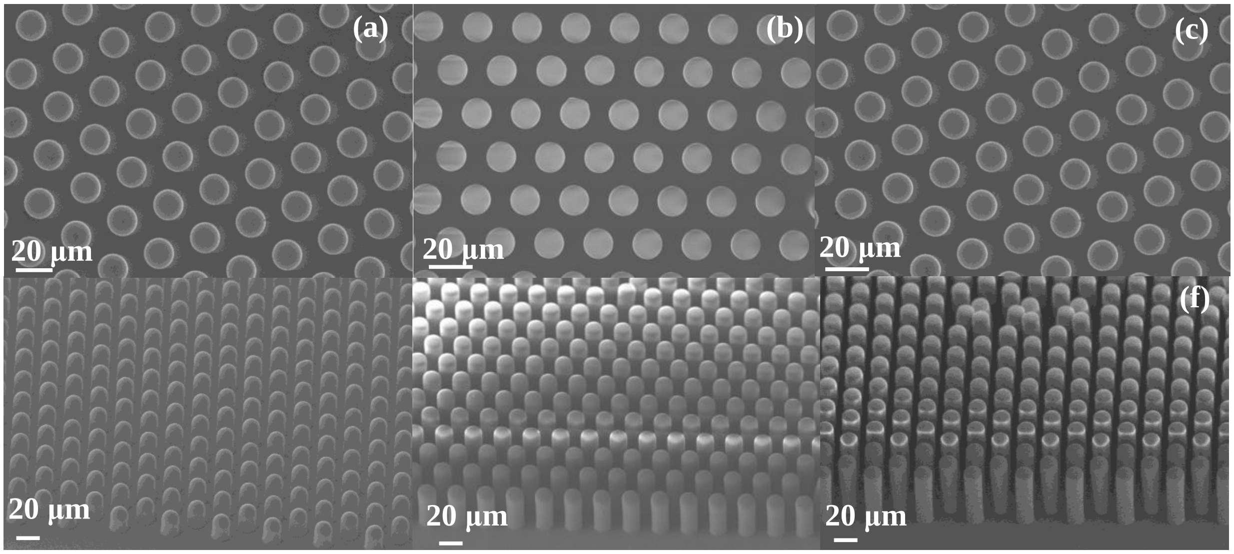

Figure 4.3. (a, b, c) Top-view SEM image of the micropillar arrays in a hexagonal configuration, (d, e, f) side-view of micropillars of varied aspect ratios: (b) sample 3 having an aspect ratio of 1.5, (c) sample 4 having an aspect ratio of 3.0, and (d) sample 5 having an aspect ratio of 4.5.

The oleophobicity of as-prepared samples was characterized at room temperature in terms of the static, advancing, receding angles and CAH as listed in Table 4.2. A comparison was first made to evaluate the effect of FDTS on the oleophobicity between sample 1 and sample 2. Sample 1 has a static oil CA of 76° while the sample 2 has a static oil CA of 100° indicating an oleophobic surface was obtained by blending FDTS. The advancing, receding and CAH of the sample 1 and sample 2 further showed that the blended FDTS improved the oleophobicity and reduced the CAH from 23° for the sample 1 to 17° for the sample 2. Since the smaller CAH indicates the lower energy required to remove liquid from the surface, the addition of FDTS could reduce the oil adhesion.

Table 4.2 Static contact angle (CA), advancing contact angle (Adv.), receding contact angle (Rec.) and contact angle hysteresis (CAH) of samples 1 to 5.

Sample ID	Aspect ratio	CA	Adv.	Rec.	CAH
1		76.0°±5.9°	80.0°±5.6°	57.3°±6.7°	23.0°±2.6°
2		100.0°±3.1°	107.0°±1.2°	90.0°±0.6°	17.0°±1.5°
3	1.5	141.0°±3.3°	149.0°±2.0°	137.0°±0.6°	12.0°±1.0°
4	3.0	146.0°±3.3°	150.0°±1.0°	140.0°±1.0°	10.0°±1.0°
5	4.5	138.0°±2.4°	141.0°±1.0°	127.0°±0.6°	14.0°±0.6°

In this work, sample 3, sample 4 and sample 5 are micropillars made of the FDTS blended PDMS, which displays the static oil CA of 141°, 146° and 138°. It could be intuitive to expect that oil CAs might keep increasing as the samples' aspect ratio increased from 1.5, 3.0, to 4.5 (Table 4.2), however, the largest aspect ratio of 4.5 (sample 5) showed a smaller static oil CA of 138°. This is because micropillars tend to deform at a high aspect-ratio. There are two possible types of pillar deformations associated with the aspect-ratio: (a) lateral collapse or bundling because of the surface forces between the neighboring pillars and (b) buckling because of the body weight of the pillars and any external load.[186-188] For the lateral collapse, the critical aspect ratio of PDMS micropillars can be estimated from recent contact mechanics analysis by Glassmaker et al which provides the following equation.[186]

$$\left(\frac{h}{d}\right)_C = \left[\frac{3^{\frac{3}{4}}\pi E w^{\frac{3}{2}}}{2^{\frac{1}{4}}32\gamma_{sv}(1-v^2)^{\frac{1}{4}}d^{\frac{1}{2}}}\right]^{\frac{1}{3}} \qquad \text{Equation 4.3}$$

In which h, d and w are the height, diameter and lateral separation of the micropillar, respectively. γ_{sv}, v and E are the surface energy of the pillar materials, Poisson value (~0.5)[174] and PDMS elastic modulus (~ 2.0 MP). The calculated critical aspect ratio $\left(\frac{h}{d}\right)_C$ of the PDMS micropillars is estimated to be 4. The aspect ratio of the sample 5 is 4.5, which exceeds the critical aspect ratio. For the pillar buckling, we estimated the critical height for the pillar buckling from the following equations.

$$h_C = \left(\frac{7.837 \times EI}{q}\right)^{1/3}, \qquad \text{Equation 4.4}$$

where q is the compressive load on the pillars, $I = \frac{\pi d^4}{64}$. When only the body weight of the pillars (1.2×10^{-10} N) was considered, the h_C was estimated to be 152 μm; however, when the external load from the oil droplet on an individual pillar (148 N/m) is considered, the h_C is estimated to be 44 μm, which is close to the micropillar height of sample 4 but is much smaller than that of sample 5. Therefore, even though we did not observe the micropillars of the sample 5 bundle or collapse under their own weight, it is likely that the micropillars might have been deformed under the pressure of the oil droplet during the contact-angle measurements, causing a decrease in the oil CA in comparison with the sample 4.

The examination of the CAH of the samples 3-5 in Table 4.2 showed that the CAH values of micropillars are much smaller than those of the flat sample surfaces; the sample 4 has the smallest CAH. The low CAH shows that the FDTS blended PDMS micropillars have a remarkable self-cleaning property, which is supposed to reduce the frozen oil adhesion forces. To predict how much work is needed to remove the frozen oil droplet from the prepared surfaces, was applied the Dupre-Yong equation to calculate the work of adhesion using the receding CAs. The values of dimensionless factors: $(1 + cos\theta_{rec})$ for all samples are listed in Table 4.3 and the value of W_p is plotted in Figure 4.4.

Table 4.3 The dimensionless factor at equilibrium state and practical case.

surfaces	$1 + cos\theta_{rec}$
sample 1	1.54±0.096
sample 2	1.00±0.01
sample 3	0.27±0.07
sample 4	0.23±0.025
sample 5	0.40±0.008

At the dynamic (or receding) state, 78.2 J work would be applied to remove the oil droplet from the sample 1 surface, while the work of adhesion dropped to 50.8 J when the surface became olephobic, as in sample 2. Compared with the flat surfaces, the surface with the smallest oil CA only needs a work of 11.9 J (on sample 4) to remove the frozen oil droplet, which is 7 times less than that of sample 1, suggesting a remarkable reduction of frozen oil adhesion *via* construction of micropillars. Overall, Figure 4.4 shows the trend of the work of adhesion decreasing with the improvement of oleophobicity in terms of the receding CA. Thus, we hypothesized that the frozen oil adhesion strength can be reduced with the increasing in oleophobicity, assuming that the measured frozen oil adhesion is proportional to the calculated thermodynamic work of the adhesion.

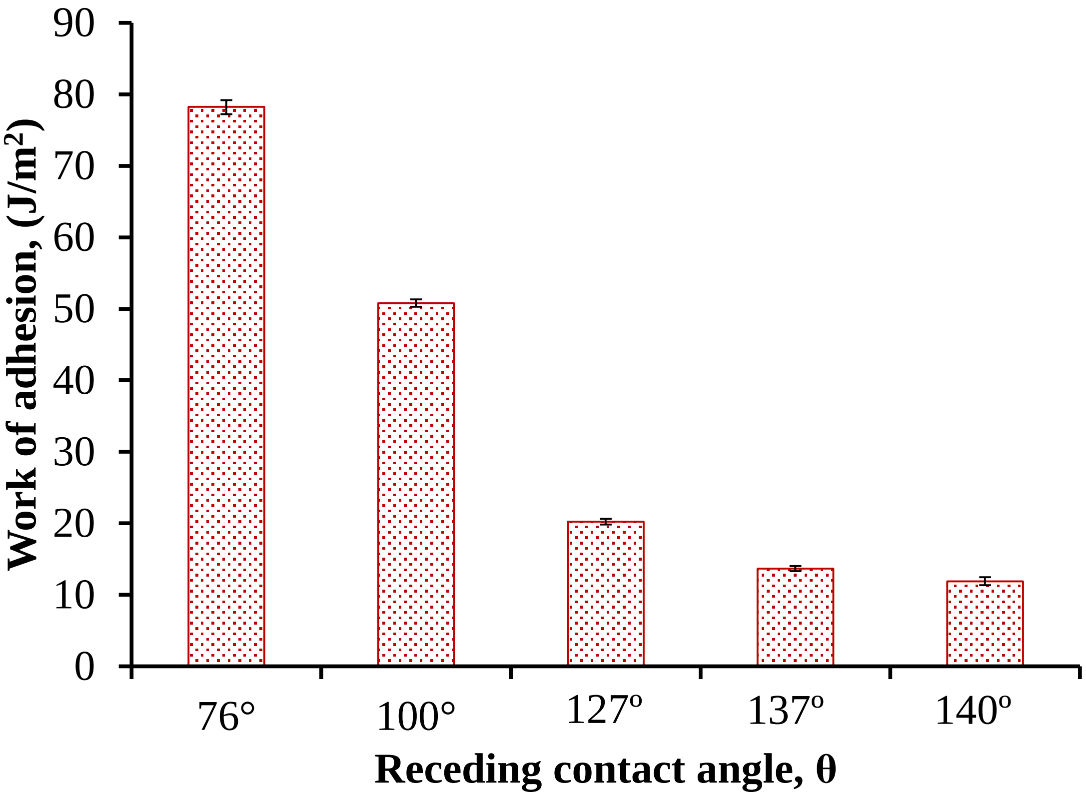

Figure 4.4. Work of adhesions calculated from equation (2) versus the receding oil contact angles for the flat and micropillared surfaces.

4.3.2. Frozen Oil Adhesion at Low Temperature

The freezing of the liquid diiodomethane droplets into solid state can be roughly reflected by the color change and its nontransparency. Liquid diiodomethane is transparent while its frozen state has a white color and is opaque. Figure 4.5 shows optical images of the samples at room temperature (transparent) and after freezing for 30 mins at –25 °C (white in color and nontransparency). The left column is the liquid diiodomethane on sample 1 to sample 5. The static CA on sample 1 is 76°; and diiodomethane spreads on the surface resulting in a large contact area (Figure 4.5a). The CA on sample 2 (Figure 4.5b) is 100°, having a smaller contact area than on sample 1 because sample 2 is more oleophobic due to the blended FDTS. After micropillars are constructed on the oleophobic surface, liquid droplets all bead up, leading to even smaller contact areas. Overall, the contact area between the solid droplets and surfaces follows the same trend as that for the liquid state. The contact line and area of the frozen droplet on micropillars are slightly larger than those of liquid oil droplets (Figure 4.5 h-j, indicating a possible change in the wetting state during the freezing; the oil may have penetrated partially into the grooves and spread out a bit. This is because during the long freezing process the liquid oil was not at stationary[1,7] and wetted the micropillars partially, resulting in the slightly increasing of contact line/area of frozen oil droplet.

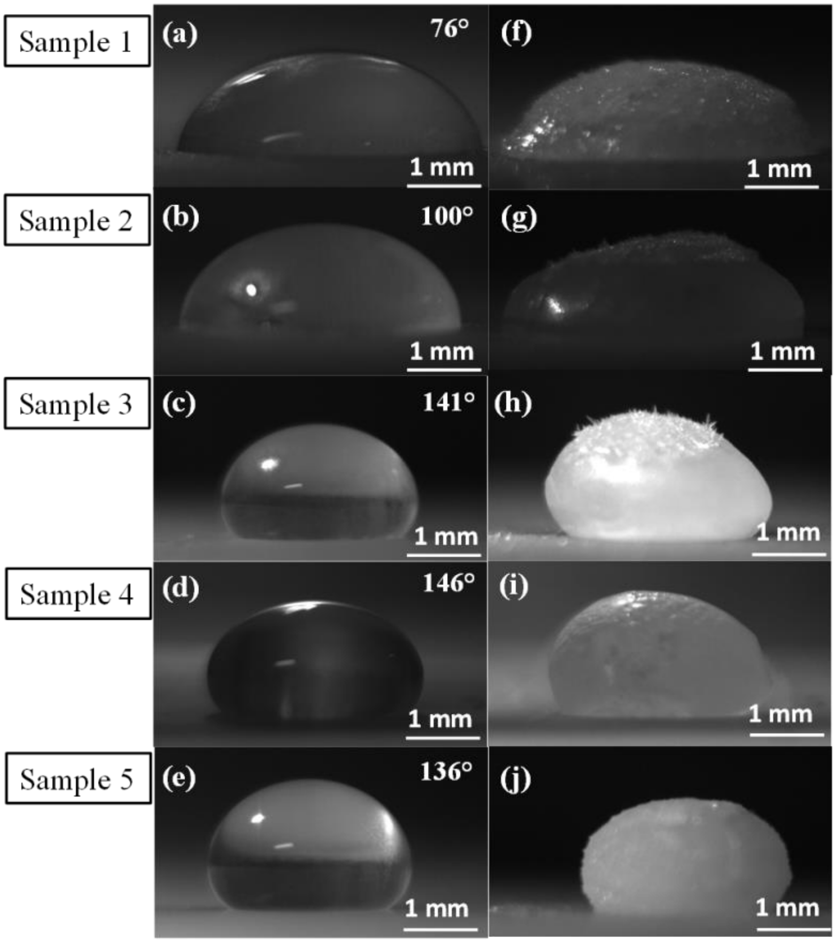

Figure 4.5. (a-e) Optical images of liquid droplets of diiodomethane on samples of varied oleophobicity, and (f-j) the corresponding frozen droplets of diiodomethane at –25 °C after freezing for 30 mins.

The adhesion of frozen oil droplets on the surfaces is characterized through the knock-off test, as illustrated in Figure 4.6a, which is similar to the setup in the previous studies of ice adhesion.[189] Figure 4.6b shows a frozen diiodomethane droplet adhered on the flat surface (sample 1) which exhibited a white color; Figure 4.6 c, d shows the surfaces after the knock-off tests. Note that a thin layer of frost condensed on the surfaces outside the oil droplet.

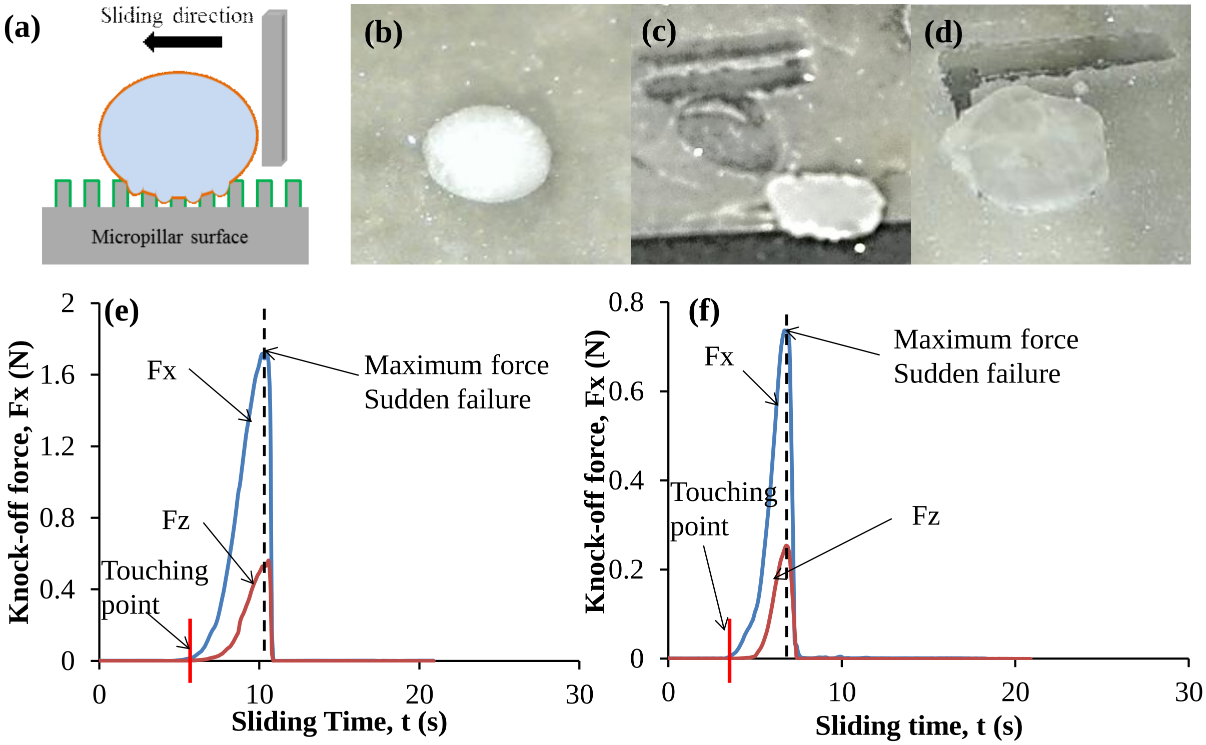

Figure 4.6. (a) Schematic illustration of the knock-off test on oleophobic surfaces; an optical image of (b) the top view of frozen oil droplet sit on the sample 1 and (c) the detached surface after the test; (d) the detached spot of the knock-off test on the sample 4; and (e, f) the lateral (F_x) and normal (F_z) knock-off forces on the flat PDMS (sample 1) and the FDTS blended PDMS micropillars (sample 4).

The possible effect of the frost on measured oil adhesion were investigated by additional scratch tests, showing that the frost sat loosely on the surface and could be scratched off by a small force (< 10 mN when keeping a 0.05 mm gap between the probe and substrate), and thus it has a negligible effect on the measured knock-off forces (Figure 4.7).

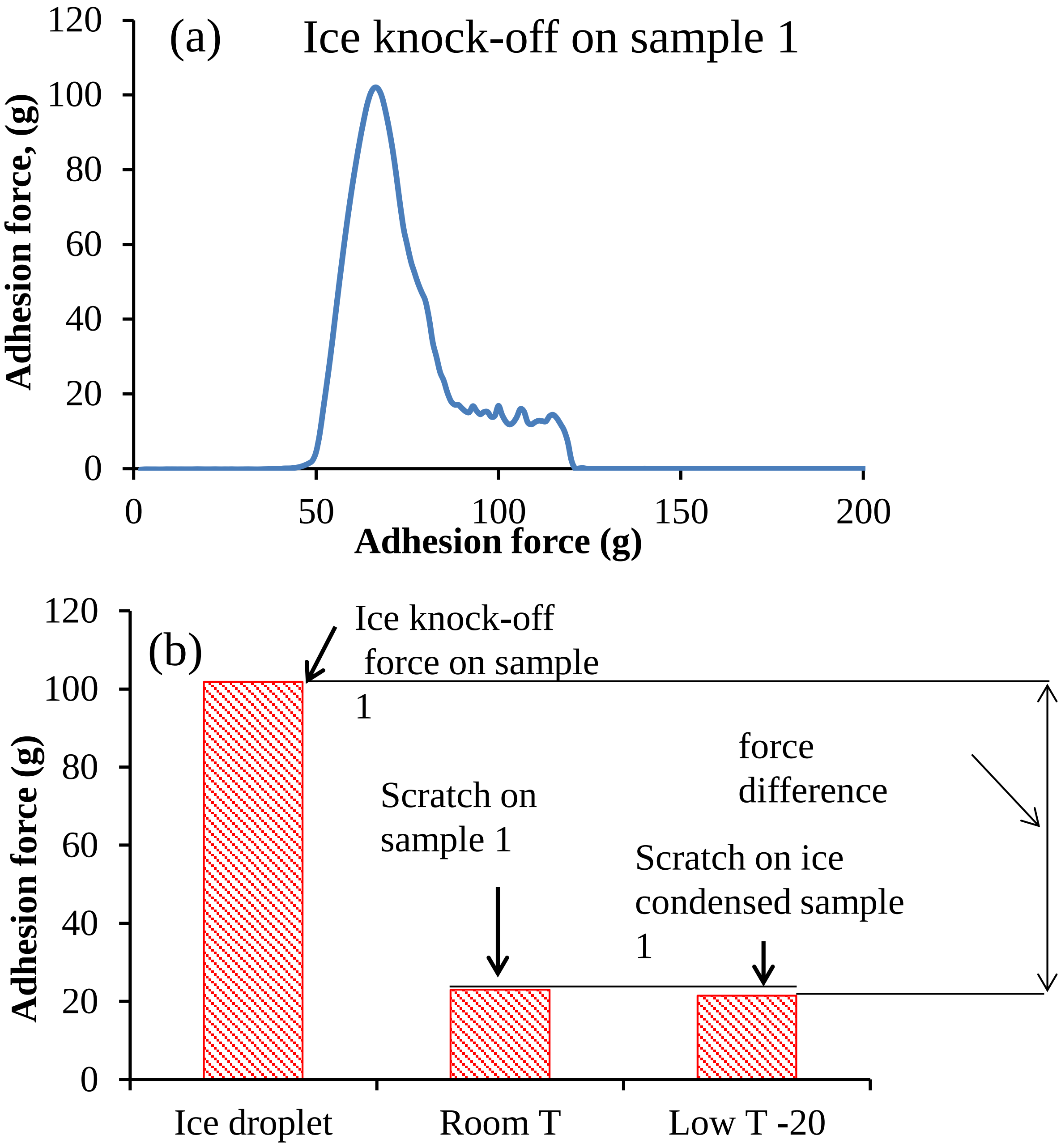

Figure 4.7. Adhesion forces of knocking off an ice droplet, scratching the sample 1 surface, and scratching the ice/frost condensed on the sample 1 surface, showing the ice/frost weakly sit on the surface and has a negligible effect on the measured adhesion force.

Typical knock-off force curves of the flat surface (sample 1) and the micropillared surface (sample 4) were plotted in Figure 4.6 e-f. The lateral and normal forces (F_x and F_z) increased at the moment of the probe touching the solid droplet and the forces dropped to zero suddenly after it reached the maximum forces, indicating the detachment of droplets from the surfaces. The appearance of F_z is because of a finite elasticity of the testing system, which is closely coupled with F_x during the knock-off process. Note that the tail force for F_z in Figure 4.6f is resulted from the lifting of the probe right after the frozen droplet was knocked off. The probe was still in contact with the knocked-off droplet; when the probe was lifted up in the Z-direction, there was a sliding resistance, giving this tail force for F_z. It is not related to the adhesion of frozen oil droplet. In the following, we used the lateral shear force F_x to characterize the adhesion force of frozen oil droplets. The examination of the detached surface (Figure 4.6c) suggested an interfacial or adhesive failure[190-192] at the interface of the sample 1. However, the detached surface (Figure 4.6d) revealed that an oil spot was left after the knock-off test, indicating the failure mode is different from the adhesive failure observed on the flat sample 1. It is likely that some oil may have penetrated into the interstitial spacing of the micropillars during the freezing, causing partial cohesive failure at the interface. To investigate the possible influence of the freezing time on the adhesion force of the frozen droplet, we varied the freezing time from 30 min to 90 min at -25°C on the sample 4. Figure 4.8 shows that increasing the freezing time led to larger knock-off force, indicating a stronger adhesion of the frozen oil on the substrate. These data revealed that the adhesion of the frozen oil on micropillared surface is time-dependent. We also noticed that when the freezing time was < 60 min, the adhesive failure dominated the separation of frozen oil droplets and substrate. After that point, the adhesion forces reached a stable level and the detachment model was transferred to be cohesive.

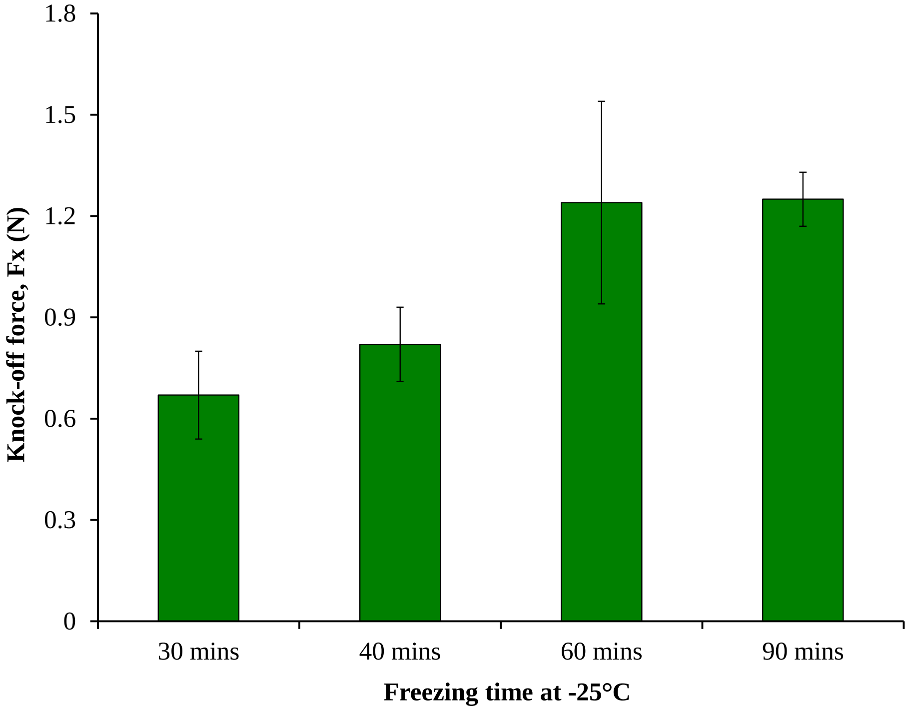

Figure 4.8. Effect of freezing time on the frozen oil knock-off force F_x on the micropillared surface (sample 4) at -25°C.

The lateral knock-off forces of the frozen oil droplets adhered on the five different surfaces were shown in Figure 4.9. To remove the frozen oil droplet on the oleophilic surface (sample 1) required a knock-off force of 1.32 N, while a small amount of FDTS blended into PDMS reduced the knock-off force to 1.02 N (sample 2), which corresponds to improved oleophobicity by reducing surface energy (Figure 4.9). The fabricated superoleophobic micropillars reduced the frozen oil adhesion forces even further. The knock-off forces were reduced to 0.75, 0.67, and 0.89 N on the superoleophobic micropillar the samples 3, 4 and 5. The lowest adhesion force was on the surface with the highest oil CA (sample 4), and was 0.67 N. This is almost half of the adhesion on the sample 1, verifying that a structured surface can reduce the adhesion force significantly.

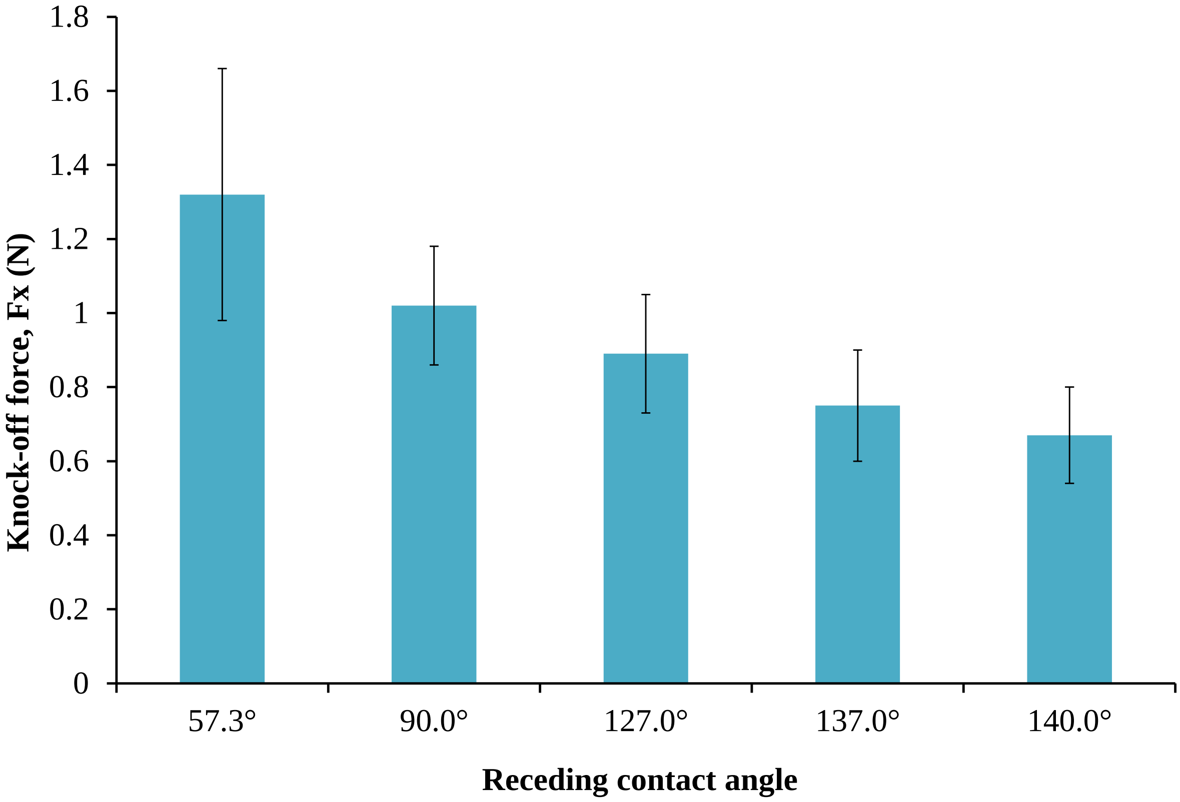

Figure 4.9. Frozen oil knock-off forces versus receding oil contact angle on the five samples of varied oleophobicity.

The real contact area of the frozen oil and its substrate surface appears to be one of the essential factors, affecting the adhesion strength of the micropillared surfaces. In the ideal Cassie-Baxter state, the oil droplet sits on top of the micropillars without penetrating into the grooves. In practice, there is always a certain extent of penetration. Thus, the real contact between oil droplet and surface can be divided into two parts: lateral contact and vertical contact, as illustrated in Figure 4.10. The top view of the oil droplet on a micropillar surface is shown in Figure 9a, indicating that the lateral contact area is the surface area of the top end of micropillars in direct contact with the oil droplet. Figure 4.10b shows the side view of the droplet sitting on micropillars as well as a partial penetration into the cavities. The real contact area between the oil droplet and flat/micropillar-covered surface is composed of the horizontal and vertical contact areas, which can be written as $S_t = S_h + S_v$, where S_t is the total contact area between oil droplet and surfaces, S_h is the overall horizontal contact area and S_v is the vertical contact area.[186]

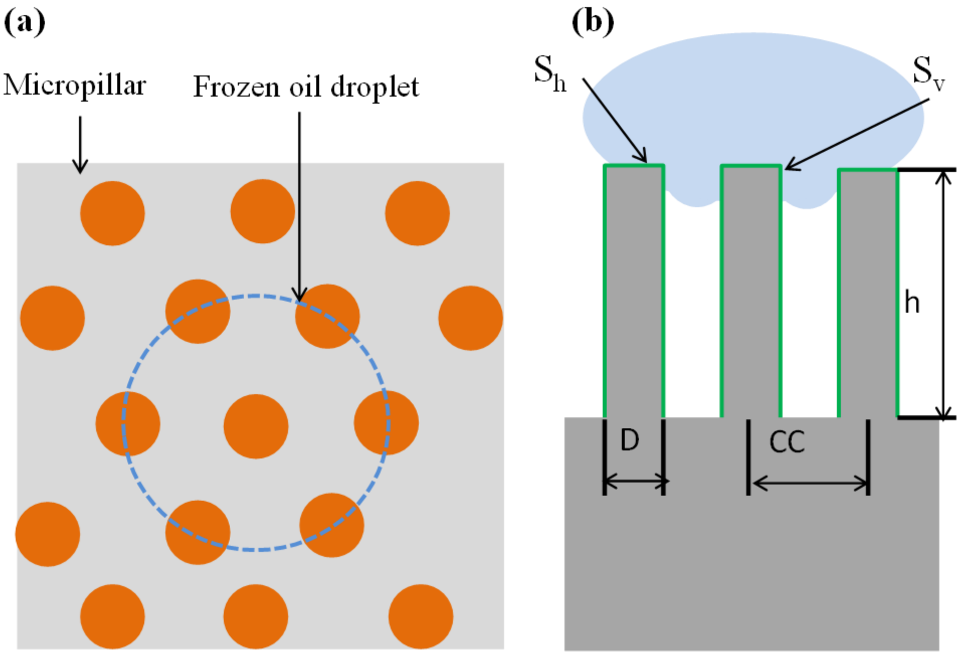

Figure 4.10. (a) Schematic explanation of horizontal contact and (b) vertical contact between oil droplet and solid surface interfaces.

The horizontal contact area S_h can be defined in following equations:[115]

$$S_{h-\mathrm{Wenzel}} = \pi(r)^2 \qquad \text{Equation 4.5}$$

or

$$S_{h-\mathrm{Cassie}} = N\pi\left(\frac{D}{2}\right)^2 \qquad \text{Equation 4.6}$$

in which, r is the radius of the frozen oil droplet and D is the diameter of the micropillars. Equation 4.5 describes the horizontal contact area of the oil droplet, and micropillars at the Wenzel state are simply the size of the oil droplet. This is because in Wenzel state oil droplet flows into grooves and reaches the bottom of the micropillars so that the entire lateral area beneath the droplet is in contact. The vertical contact area is the surface area of the micropillars' walls in contact with the oil droplet. The vertical contact area is defined in Equation 4.7:[37]

$$S_v = \pi D \sum_{i=1}^{N} h_i \qquad \text{Equation 4.7}$$

in which h_i is the penetration depth at each interstitial spacing among the micropillars, h is the maximum penetration depth, i.e. the height of the micropillars, N is the number of the micropillars in contact with the droplet. Equation 4.7 indicates three different oil stages on micropillars: a. Wenzel state, $S_v = N\pi Dh$; b. Cassie-Baxter state, $S_v = 0$; c. Cassie-Wenzel state (partial penetration), $0 < S_v = \pi D \sum_{i=1}^{N} h_i < N\pi Dh$. Practically, it is very difficult to calculate the real contact area in the Cassie-Wenzel state because the penetration depth of the oil droplet is hard to detect.

To a first approximation, we consider the oil droplet was in the Cassie-Baxter state, beading up without penetrating into the groove. The adhesion strengths of the frozen oil on the FDTS blended PDMS micropillars were estimated by dividing the measured knock-off force F_x with the horizontal contact area which was calculated by equation 4.6 and listed in Table 4.4. It reveals that the adhesion strengths of frozen oil decreased with reducing the work of adhesion. The frozen oil adhesion strength of the oleophilic sample 1 and oleophobic sample 2 are 95.8 kPa and 91.9 kPa, respectively. In contrast, the adhesion strengths on micropillars are less than half of those on the flat surfaces, showing the pronounced effect of the micropillars. Even though the adhesion on the three micropillared surfaces appears to be very similar, a more careful examination revealed that the adhesion decreased as the oil CA increased for these three micropillar surface.

Table 4.4 The calculation of horizontal contact area between frozen droplet and micropillars.

sample ID	Aspect ratio	Contact line (mm) (liquid state)	Contact line (mm) (solid state)	Nominal contact area (mm^2)	Lateral contact with micropillars (m^2)	Adhesion strength (kPa)
sample 1	-	4.0±0.18	4.19±0.05	13.78±0.35	-	95.8
sample 2	-	3.4±0.02	3.76±0.05	11.10±0.31	-	91.9
sample 3	1.5	2.7±0.06	2.78±0.08	6.07±0.33	$2.02\times10^{-6}\pm4.0\times10^{-8}$	37.1
sample 4	3.0	2.6±0.08	2.67±0.06	5.60±0.25	$1.87\times10^{-6}\pm3.6\times10^{-8}$	35.9
sample 5	4.5	2.9±0.07	3.00±0.08	7.07±0.36	$2.35\times10^{-6}\pm5.0\times10^{-8}$	37.8

It is interesting to note that the adhesion strength did not always drop with the increasing aspect ratios: 37.1 kPa for sample 3 (aspect ratio 1.5), 35.9 kPa for sample 4 (aspect ratio 3.0), and 37.8 kPa for sample 5 (aspect ratio 4.5). This phenomenon is similar to the change of oil CAs with the aspect ratio, and can be explained by the possible partial penetration of oils into grooves or a transition state from the Cassie to Cassie-Wenzel composite state. It might be worthwhile to further discuss the wetting of micropillars. The wetting transition from the Cassie state to Wenzel state is due to the movement of the meniscus toward the bottom of the interstitial spacing among the pillars as illustrated in Figure 4.10. At the beginning, the liquid droplet sits on the top of the pillars. With time, the meniscus may sag and start to wet the wall of pillars; it may even depin from the corner of pillars and penetrate into interstitial spacing to fully wet the pillars (the Wenzel state). Even though the exact wetting transition mechanism is hard to know, the relatively small CAH (see Table 4.2) suggested that the oil droplets may have only sagged into the cavities partially instead of the depinning.[94,97] The critical CA θ_C of the transition from Cassie state to Cassie-Wenzel composite state can be determined by equation 4.8.

$$\cos\theta_C = (\Phi_S - 1)/(r - \Phi_S) \qquad \text{Equation 4.8}$$

where Φ_S is defined as the fraction of solid-liquid interface and the roughness r is defined as,

$$r = \frac{4\pi RH}{\sqrt{3}CC^2} + 1 \qquad \text{Equation 4.9}$$

R, H and CC denote the micro pillars' radius, height and center-to-center spacing, respectively.[11]

$$\Phi_S = \frac{\text{textured area}}{\text{whole area}} = \frac{2}{\sqrt{3}}\frac{\pi R^2}{CC^2} \qquad \text{Equation 4.10}$$

The calculated critical CA θ_C is 124° which is smaller by $\Delta\theta = 17$ degrees than the oil contact angle on the sample 3 (141°). The critical contact angle of the sample 4 was calculated to be 105°, which is smaller by $\Delta\theta = 41$ degrees than the measured static contact angle (146°). Since $(\Delta\theta)_4 > (\Delta\theta)_3$, the extent of partial penetration on sample 4 is less than that on sample 3. As a consequence of this difference, the sample 4 shows both the largest oleophobicity (as shown in Table 4.2) and lowest frozen oil adhesion strength; however, this trend did not continue with sample 5 of the largest aspect ratio of 4.5. The highest adhesion strength of the sample 5 was likely because of to the deformation of micropillars because the aspect ratio is larger than the critical aspect ratio. The micropillars may have been deformed under the weight of oil droplet, causing the formation of interlocks between oil and micropillars.

To obtain insights into the oleophobicity and frozen oil adhesion, we further explore the possible relationship between the measured adhesion strength of frozen oil droplets and the thermodynamic work of adhesion. For this, the work of adhesion is calculated from the measured oil CA using the Young-Dupre equation. Figure 4.11 plots the measured adhesion strength vs the calculated work of adhesion. Overall, the frozen oil adhesion increased with the work of adhesion; however, the relationships for the flat and micropatterned surfaces are quite different. The oleophilic flat PDMS shows the largest frozen oil adhesion strength and work of adhesion.

The blended FDTS results in the oleophobicity and the reduction of contact area. In the marked segment for flat surfaces, the blended FDTS was used to reduce the adhesion, the adhesion strength increased nearly linearly with work of adhesion; a simple linear fitting gives a slope of 0.19 and intercept of 84.0 kPa. The marked segment for the micropillar surfaces where the amount of blended FDTS is the same while the aspect ratios are different. In this regime, the adhesion strength is also proportional to the work of adhesion; a slope of 0.42 and intercept of 32.3 kPa of the linear fitting are obtained. These comparative analyses suggest that the addition of micropillar at the surface alters the relationship between the measured adhesion strength and the work of adhesion. It is apparent that the measured adhesion strength increased more rapidly with the work of adhesion for the micropillared surfaces than that for the flat surfaces. Thus, there is a possible synergetic effect between the use of FDTS chemistry and micropillar on the reduction of frozen oil adhesion, which needs to be further explored in future studies.

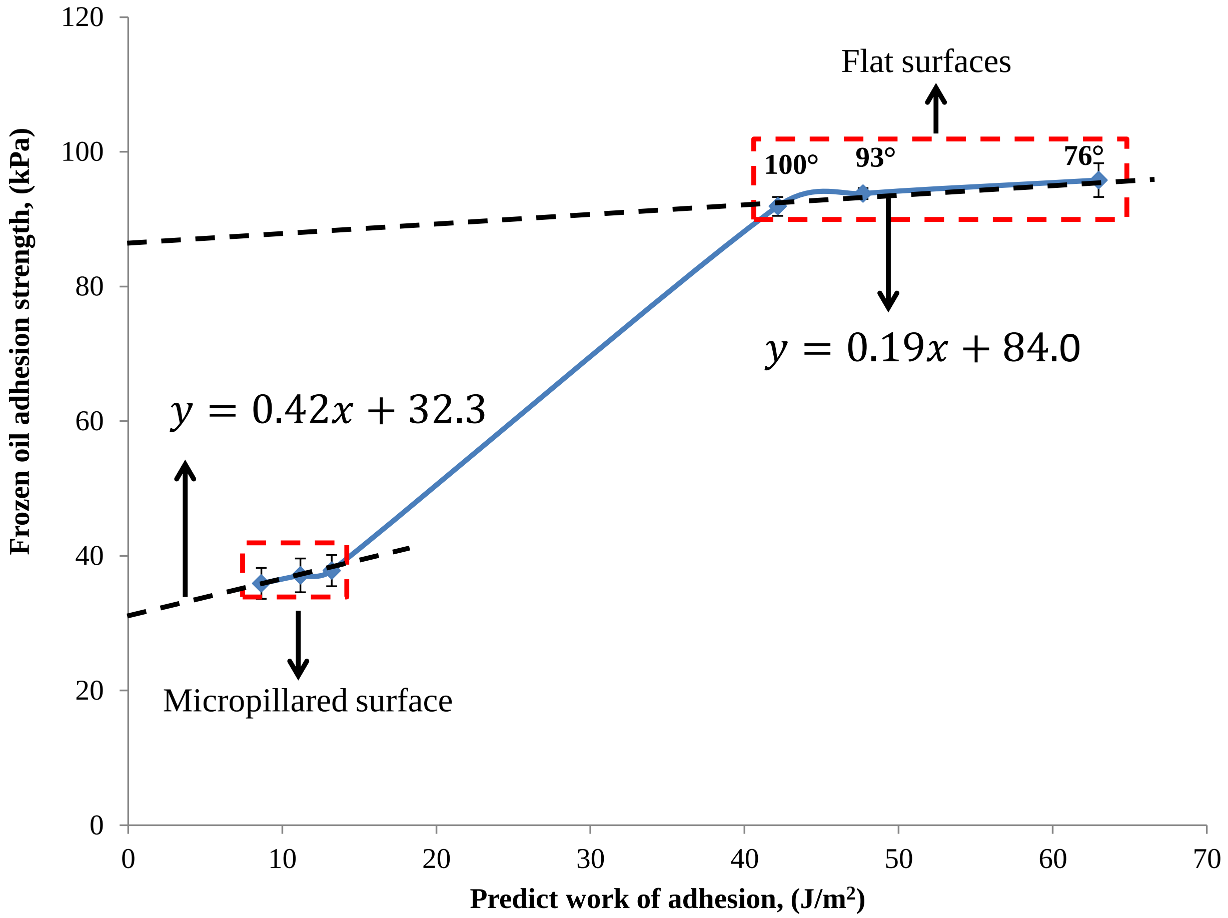

Figure 4.11. Relationship between the calculated work of adhesion and the frozen oil adhesion strength. The dashed lines are the linear-fittings of the flat surfaces and micropillared surfaces.

4.4 Conclusions

In summary, surfaces with varying oleophobicity have been fabricated through a FDTS blending approach and mold transfer technique. The oleophobicity was studied in terms of the static, advancing/receding, and the CAH. Knock-off tests were performed to characterize the frozen oil adhesion forces, which were used to calculate the adhesion strengths to evaluate the effects of oleophobicity on frozen oil adhesion strength. The oleophilic neat flat PDMS shows the smallest oil CA of 76° and the highest frozen oil adhesion strength of 95.8 kPa, while the adhesion strength on the most oleophobic micropillared surface was only 35.9 kPa with the highest oil CA of 146°. The decrease in the adhesion strength is related to the reduction of contact area between frozen oil droplets and oleophobic surfaces, which was achieved by the surface energy reduction and construction of micropillars. The relationship between oleophobicity and frozen oil adhesion has been investigated for the first time showing an overall trend of the higher oleophobicity giving lower adhesion strength of frozen oil and suggesting a possible synergetic effect of utilizing the FDTS chemistry and micropillars on the reduction of frozen oil adhesion strength.

Chapter 5. Development of Electrically Conductive–Superoleophobic Micropillars at Surface for Reducing Oil Adhesion at Low Temperatures

5.1. Introduction

The performance of instruments working with oils such as engines, oil pumps, oil pipelines, and devices using oil lubricants are heavily affected by oil adhesion.[44-46,193] When oil becomes viscous or even frozen at cold regions, the oil adhesion to surfaces will increase, leading to excess energy consumption and even serious problems such as clogging, instrument malfunction or accidents.[43,194,195] In order to prevent such problems, it is necessary to explore effective methods to reduce the frozen oil adhesion. Oleophobicity has been regarded as one of the most important factors for oil adhesion at room temperature, suggesting that superoleophobic surfaces can reduce oil adhesion.[174,176,196-198] However, there are a limited number of studies on oil adhesion at low temperatures especially when the oil is frozen; the scientific understanding is far behind the need of the industry development. Thus, it is crucial to investigate the effects of oleophobicity on frozen oil adhesion at sub-zero temperatures[199] and develop techniques that could potentially mitigate the negative effects of the frozen oil and even actively de-freeze the oil.

The extensive studies of ice adhesion reduction and de-icing provide literature and inspiration for work on reducing the adhesion of frozen oil.[200-203] It was reported that superhydrophobic micro/nanostructures can significantly delay the ice formation and reduce the adhesion strength because the superhydrophobic structures are highly water repellent, preventing the formation of ice nuclei and reducing the contact between ice and substrate effectively.[204-206] Both passive and active strategies have been utilized to remove accumulated ice.[51-53] In the passive

---

*This chapter has been published in *Applied Surface Science* **2016**, *389*, 623-631.

strategy, ice is mechanically separated from the surface (such as knocking-off the ice); the critical factor is to reduce the surface energy thereby reducing the contact between ice and substrate.[54-56] Thus far, many works have been reported on the use of superhydrophobic structures to delay ice formation and reduce ice adhesion because water droplets bead up on superhydrophobic structures to minimize the contact areas so as to delay the ice formation and reduce ice adhesion.[50, 57] Guo *et al.*[52] reported that it took more than 3 hours for the ice to accumulate on superhydrophobic nanohair/micro ratchet hierarchical structures, showing the significant ice delaying property on nanostructures. Davis *et al.*[52] studied the effects of hydrophobicity on ice adhesion strength and found that the ice adhesion strength was significantly reduced on self-clearing surfaces with high hydrophobicity and low contact angle hysteresis. In the active strategy, extra thermal or electric energy is applied on ice accumulated surfaces.[204, 207, 208] DC power melting is regarded as one of the most efficient approaches for de-icing.[58-60] Volman et al.[59] reported using graphene thin film as a conductor to melt the ice. We hypothesize that similar strategies of controlling the surface chemistry and structure can be exploited to mitigate oil adhesion. Oils are also a good liquid to model the general unfreezing process since they have low surface tension and are non-conductive.

We have explored the effects of surface chemistry and structures on frozen oil adhesion in our previous work by blending trichloro 1*H*, 1*H*, 2*H*, 2*H*-perfluorooctyl silane (FDTS) with polydimethylsiloxane (PDMS) and constructing micropillars.[197] The results showed that the adhesion strength of the frozen oil was reduced significantly on superoleophobic micropillars compared to the flat surface. In this work, we report our development of electrically conductive superoleophobic micropillars for actively reducing oil adhesion or even de-freezing through applying DC current onto the microstructures. For this, we employed the conductive polymer composites (CPCs) of Ag flakes/epoxy polymer composites because of their adjustable resistance and good processability.[139-141, 209-212] The electrical resistivity of composite micropillars was modulated by the amount of conductive fillers so as to change the effect of local surface heating. The thermal effect of DC current on surface was also compared with the heating effect from hot air to demonstrate that the construction of electrically conductive micropillars is effective for reducing the adhesion of frozen oil.

5.2. Materials and Methods

5.2.1 Materials

A silicon micropillar master mold (SU-8-25, Microchem Co., Newton, MA, USA) with the parameters of 10 μm × 68 μm × 25 μm (diameter × height × center-center spacing) was used as the first mold to fabricate polydimethylsiloxane (PDMS: $(C_2H_6OSi)_n$, Sylgard 184, Dow Corning Co. USA) microholes, curing agent (Dow Corning Co. USA), epoxy (diglycidyl ether of bisphenol A, DERTM 322, DOW chemical company, USA), cure agent for epoxy (triethylenetetramine, TETA, DOW chemical company, USA) , silver flakes (Ag flakes, Aldrich), trichloro (1*H*, 1*H*, 2*H*, 2*H*-perfluorooctyl) silane (FDTS, $CF_3(CF_2)_7(CH_2)_2SiCl_3$, 97%, Sigma–Aldrich Chemicals, USA), diiodomethane droplets (10 μl, CH_2I_2, 99%, freezing point: 5.4 °C, Sigma–Aldrich Chemicals, USA).

5.2.2 Epoxy & Ag Flakes Composites Micropillars Fabrication

To fabricate PDMS microholes, 6 g PDMS elastomer and 0.6 g curing agent were mixed at a ratio of 10:1. The mixture was poured onto the micropillar mold and was transferred into an oven after completely degassing. The sample was cured under 90°C for 1h and was then peeled from the silicon mold gently for future use. The procedures for making epoxy/Ag flakes composite micropillars are as follows: first, a certain amount of Ag flakes (weight percentage: 45%, 50%, 55%, 60% and 65%) were added into the 1 g epoxy. To facilitate the dispersion of Ag flakes in the epoxy, 10 μl ethanol was added into the composite to make it less viscous. The composite was mixed by using a mixer (ARE-310, THINKY Corporation, USA) at a 2000 rpm for 10 min. Next, the cure agent of epoxy was added to the above composite with a weight ratio of 0.13 to epoxy. Then the composite and the cure agent were mixed at 2000 rpm for 2 min. The homogenized mixture was poured onto the PDMS micro-holes negative mold, degassed and cured for 1 h at 90°C. Before use, the prepared PDMS microholes were coated with FDTS, $CF_3(CF_2)_7(CH_2)_2SiCl_3$ via vapour deposition. The FDTS coating reduced the adhesion between PDMS surface and epoxy, so that the PDMS can be easily peeled off from the cured epoxy. X-ray Photoelectron Spectroscopy (XPS, monochromatic Al Ka X-ray source, Thermo Scientific Alpha) was used to analyze the atomic composition of the surface. The microstructures of the obtained samples were characterized using an optical profiler (MFP-D WLI 3D surface profilometer, Rtec Instruments Inc, USA) to measure the height of the micropillars. The prepared periodic micropillar arrays were observed by field emission scanning electron microscopy (FE-SEM, LEO-Ultra, GEMINI, Germany). All of the samples were deposited with a thin layer of Au (thickness of 40 nm) to enhance conductivity of the micropillars before SEM testing.

5.2.3 Measurement of Wettability at Room Temperature

Oil contact angle (CA) measurements were carried out at room temperature using an optical sessile drop system. The CAs were collected after the droplet settled for 5 s after diiodomethane droplets were gently placed onto the surfaces. The contact angle was determined by fitting the profile using a custom-made LabVIEW program. The measurement of rolling-off angles was performed via the tilting method. The tilting tests were carried out 5 s later, following the addition of 10 μl diiodomethane droplets placed onto the samples. During the tilting process, one end of the glass slide was kept immobile and the other side was raised at a tilting rate of 1 °/s. The advancing and receding contact angles were recorded when the droplet started to roll down as the glass slide was gradually tilted. The rolling-off angles were recorded using an optical contact angle system at the moment that the droplets started to slide down.

5.2.4 Surface Adhesion Measurement

The surface adhesion force of the oil droplet on the prepared Ag flakes/epoxy micropillars were measured by the microindentation instrument. The oil droplet was held by a glass semi-sphere which came to contact with micropillars at a constant speed of 1 μm/s. Then, the holder carried the oil droplet upward with a constant speed of 1 μm/s until the droplet detached from the substrate. The detaching process was monitored in real time by a video camera. Each test was repeated 3 times on three different samples.

5.2.5 The Frozen Oil Adhesion Force Measurements

The frozen oil adhesion was measured by knock-off tests in a custom-built cooling system equipped in the Universal Materials Tester (UMT, UNMT-2MT, by Center for Tribological Inc.). This cooling system contains two main parts: (I) a coolant control system consisting of a temperature controller (ranging from -20 °C to 100 °C, Thermo Scientific C10, dimensions: 10.0 cm × 17.0 cm × 16.0 cm), as well as a coolant container and pump (ThermoScientic K10, dimensions: 19.0 cm × 35.0 cm × 37.0 cm) to supply circulating coolant (antifreeze, Recohem Inc.) to cool down a thermoelectric cooling chamber; (II) thermoelectric cooling chamber (able to reach as low as –40 °C) (Model 1198E925, Horus, Techmologies Inc. dimensions: 16.5 cm × 12.5 cm × 8.0 cm) consisting of a Peltier plate surrounded with insulating silicon foam walls to achieve a steady temperature of –25 °C. To freeze the oil droplet, the sample was tightly attached onto the Peltier plate and then a 10 μl oil droplet was placed gently. After that, the whole system was cooled down to –25 °C. The knock-off test was performed in UMT at the same time applying 1 A DC current on the sample for 2, 3 and 5 minutes. The effect of hot air on the frozen oil adhesion was measured when the surface was heated up to –5 °C by blowing hot air toward the droplet. The melting behaviours of the frozen oil droplet were recorded in the same system and the separating droplet was measured through the tilting angle test.

5.3. Results and Discussion

5.3.1 Fabrication of Epoxy/Ag Flakes Composite Micropillars

Epoxy/Ag flakes composite micropillars were fabricated by a two-step mold transfer approach (Figure 5.1a) established in our previous work.[199,213] First, PDMS microholes were fabricated from a silicon micropillar mold. Then the PDMS microholes were coated with a thin layer of FDTS through the vapour deposition method (Figure 5.1a). The prepared PDMS microholes were used as a secondary mold to construct epoxy/Ag flakes composite micropillars. The uncured epoxy/Ag flakes mixture was poured onto the PDMS microholes; after degassing, they were cured at an elevated temperature of 90 ºC for 1 h. Once cured, the secondary mold was removed. The micropillar samples were examined by SEM showing that the original hexagon structures were successfully replicated to the epoxy/Ag composites (Figure 5.1b). There are Ag flakes dispersed homogeneously on the surface of the micropillars (at the Ag flakes weight fraction of 65%, Figure 5.1b and c) In order to get an overall view of the micropillar arrays, they were scanned by an optical profilometer. It can be seen that the constructed composite micropillars are well aligned (Figure 5.1d). The *x–y* profile shows the micropillars are within the average height and center-center space of 68 μm and 25 μm, respectively, showing a good transfer of the micropillar structure from the silicon mold to the Ag/epoxy composite.

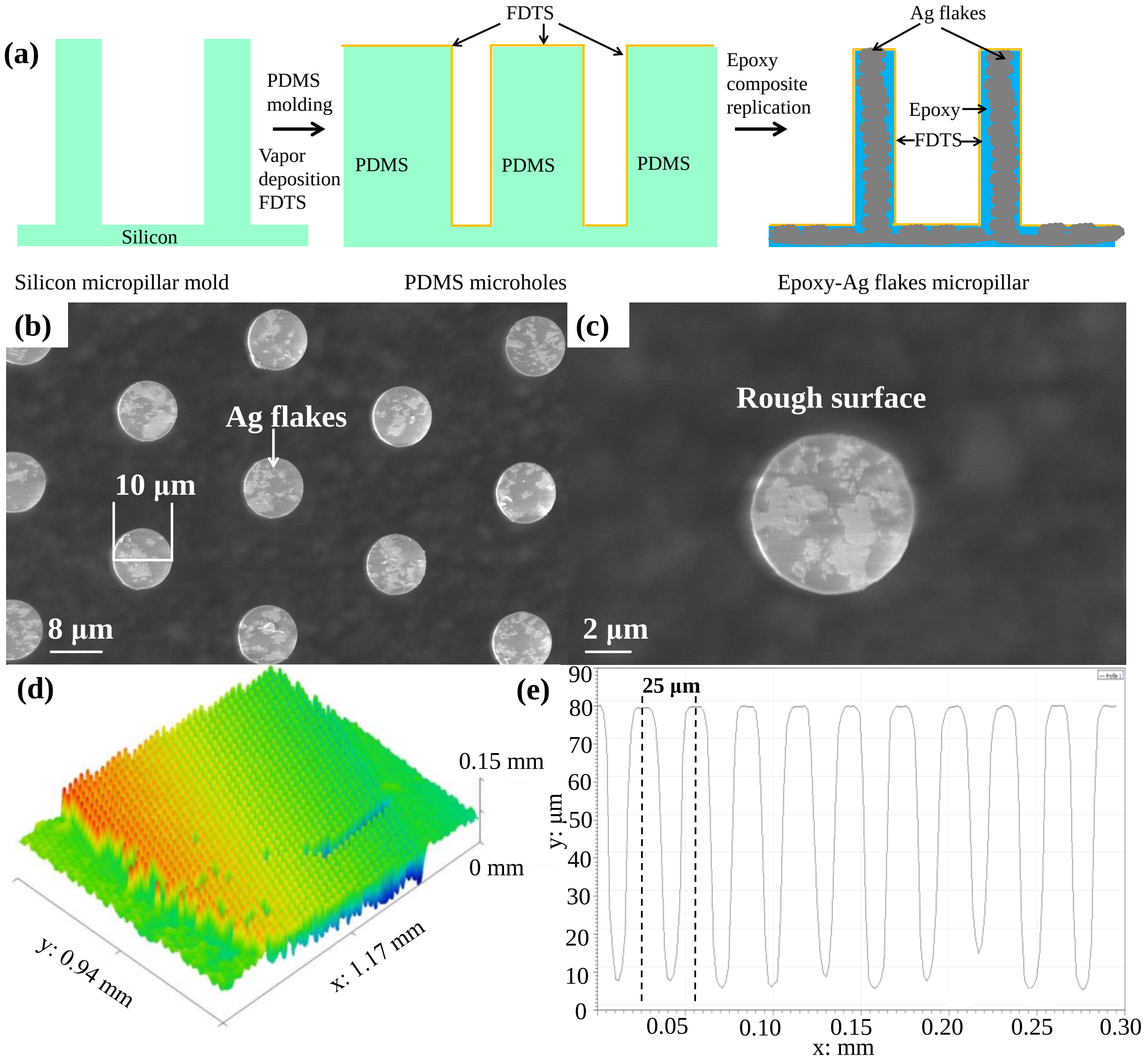

Figure 5.1. (a) Schematic illustration of fabricating epoxy/Ag flakes composite micropillars by a two–step pattern transfer approach with FDTS coated on epoxy/Ag flakes micropillars; (b) top view SEM image of the epoxy/Ag flakes composite (65 wt% Ag flakes) micropillars. The arrow pointed to Ag flakes dispersed homogeneously on the surfaces of the micropillars forming conductive pathways; (c) SEM image of single micropillar surface indicating some Ag flakes stayed on the surface of micropillars during the pattern transfer process; (d) three dimensional structure of epoxy/Ag flakes micropillar arrays observed with an optical profilometer; (e) the x–y profiles of the micropillars.

A thin monolayer of FDTS was expected to bond to the surface of epoxy/Ag flakes micropillars during the second step of the pattern transfer process where the FDTS was coated by vapour deposition on the mold of PDMS microholes to reduce the adhesion between PDMS and epoxy. It has been known that the Si–Cl functional groups of FDTS can react with –OH to form Si–O bonds.[214-216] Also, Si–Cl functional groups can react with H_2O in the air to become Si–OH; and the Si–OH functional groups can form networks through a condensation reaction.[216-218] In this study, epoxy DER 322-a bisphenol A diglycidylether (with –OH functional group) was used as the base and DEH 24-triethylenetetramine was used as the curing agent to fabricate the Ag flakes-epoxy composite micropillars. As illustrated in Figure 5.2a, during the epoxy curing, additional –OH functional groups were formed after the curing agent was added, which are supposed to react with FDTS in the presence of H_2O moisture in the air and form cross-linked networks (Figure 5.2b).

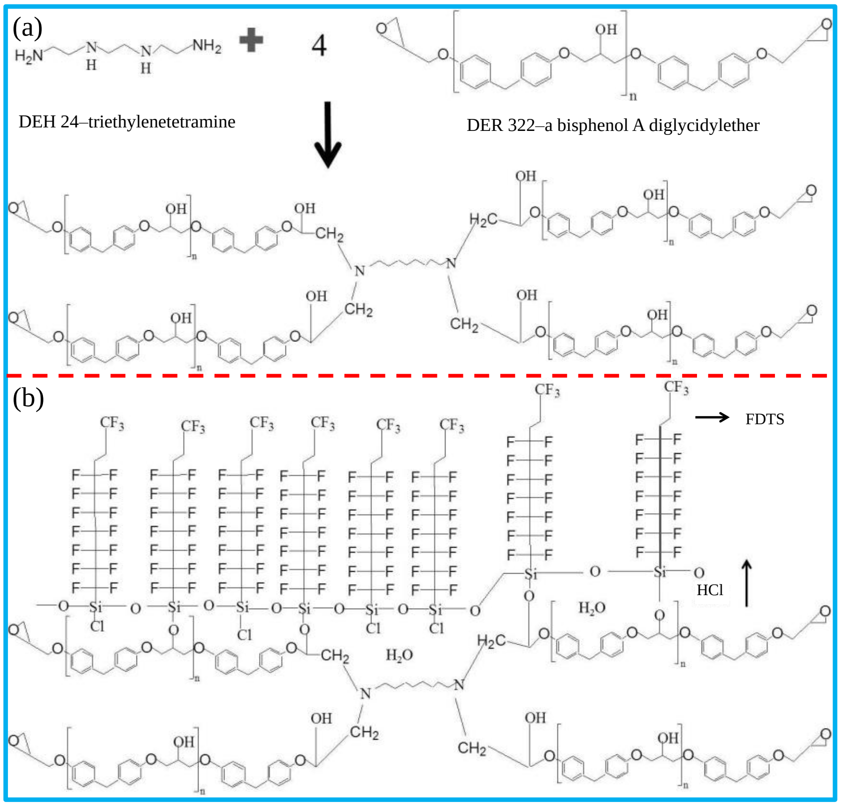

Figure 5.2. (a) Curing mechanism of epoxy DER 322–a bisphenol A diglycidylether and DEH 24–triethylenetetramine;[44] (b) FDTS bonded with epoxy lowering the surface energy.

The FDTS coated on the micropillar surface was verified by X-ray photoelectron spectroscopy (XPS) tests. As shown in Figure 5.3, strong fluorine peaks at 700 eV and 835 eV (Figure 5.3) were detected as expected.[174] The peaks of C and Si were also found in the spectrum. The concentration of fluorine at the surface was calculated at around 45%. These results indicate that during the pattern transfer process, part of the coated FDTS on the PDMS microholes reacted with epoxy and bonded to the surface. The formed monolayer of FDTS played an important role in reducing the surface energy of the micropillars so as to make it oleophobic and self-cleaning as investigated below.

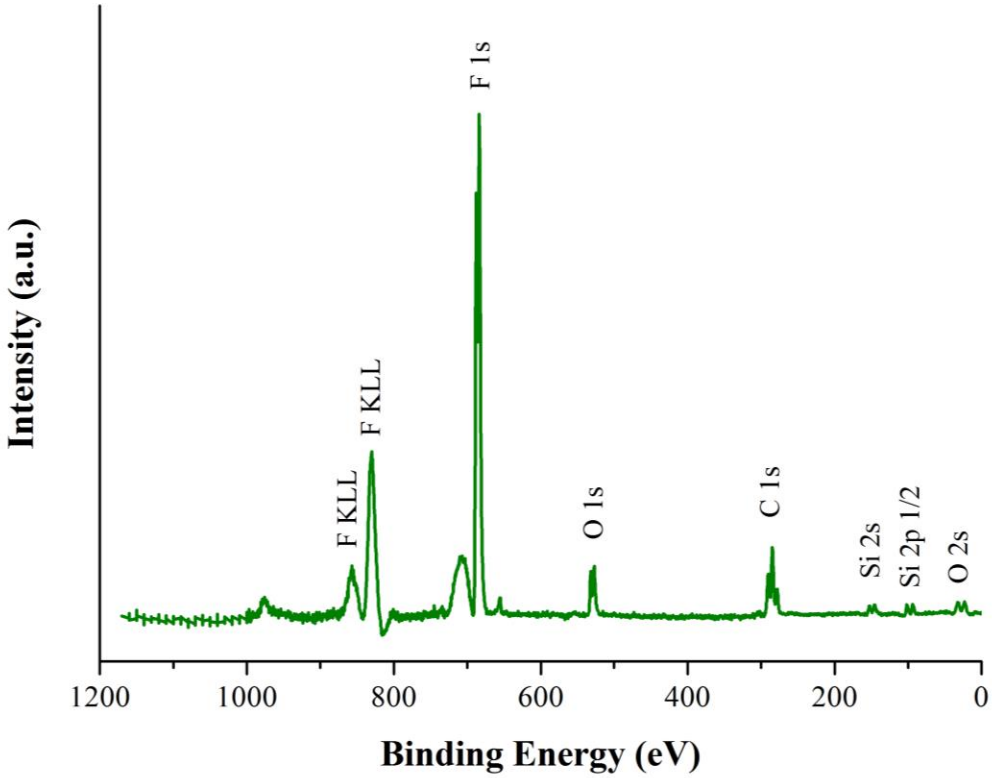

Figure 5.3. XPS spectrum showing strong peaks associated with fluorine element to verify that FDTS was embedded into the epoxy/Ag flakes micropillars surface during the second step of pattern transfer process.

5.3.2 Oleophobicity, Electrical Resistance and Low Adhesion Properties

To evaluate oleophobicity and self-cleaning properties, oil contact angle (CA), advancing contact angle (Adv.), receding contact angle (Rec) and rolling-off angle were measured by the sessile drop system at room temperature; the results are shown in Figure 5.4a. Oil contact angles on prepared composite micropillars were all larger than 140º. With an increase of Ag flakes to 65 wt%, the oil CA decreased slightly and the smallest CA was measured of 141º implying that the amount of Ag flakes was not a critical factor for the oleophobicity. To explore the self-cleaning property of these fabricated composite micropillars, rolling-off angle was first calculated using the equation proposed by Furmidge:[219]

$$\left({}^{mg}/_{w}\right) sin\alpha = \gamma_{lv}(cos\theta_{rec} - cos\theta_{adv}) \qquad \text{Equation 5.1}$$

In which, m is the weight of the liquid droplet, g is the gravitational constant, w is the width of the droplet perpendicular to the drop sliding direction, α is the rolling-off angle, γ_{lv} is the surface tension of the tested liquid, and θ_{rec} and θ_{adv} are the receding and advancing contact angles (CA). This equation describes the correlation between α and CA in terms of the dimensionless factor$(cos\theta_{rec} + cos\theta_{adv})$. The calculated rolling-off angles are 16º, 17º, 17º, 18º and 20º. In comparison, the measured rolling-off angles are10º, 11º, 12º, 12º and 13º, which are close to the calculated values. The high contact angels and small rolling-off angles verified that the as-prepared surfaces are self-cleaning.

The electrical resistance is an important parameter of the developed micropillars, which is tailored by the amount of Ag flakes. The relationship between the resistance and the content of Ag flakes in composite micropillars was investigated. Both the resistances of the flat surface and the micropillars were measured using a four probe source meter with the results shown in Figure 5.4b. A relatively large resistance of 877 Ω was obtained on the surfaces of samples containing 45 wt% Ag flakes; there is no noticeable difference in measured contact resistance between the flat surface and micropillars. By increasing the content of Ag flakes, a remarkable reduction of the resistances was obtained between 45-60 wt% Ag flakes, suggesting that the upper limit of the percolation threshold of epoxy/Ag flakes composite micropillars is around 60 wt%. Further increasing the weight fraction of Ag flake from 60 % to 65% had an insignificant effect on the resistance.

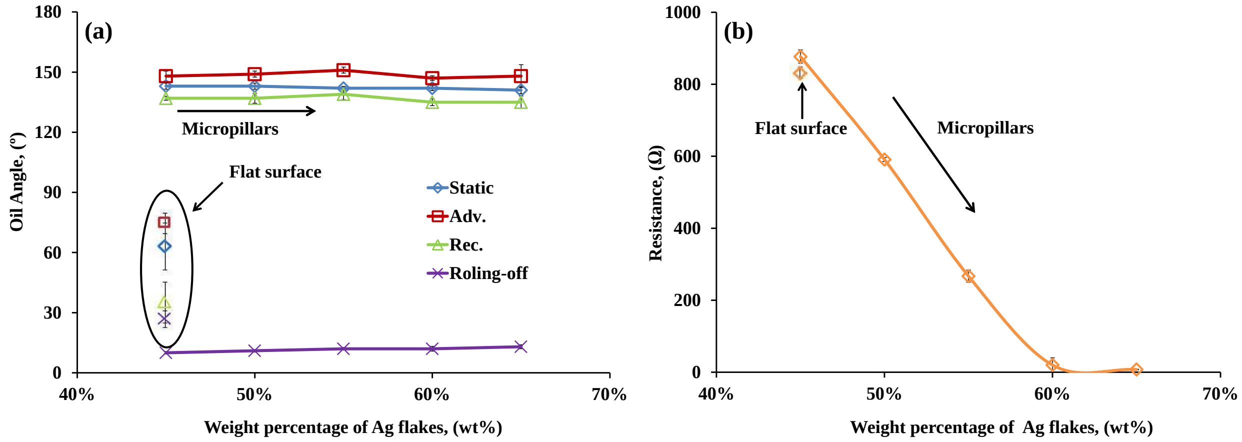

Figure 5.4. (a) Oil contact angle (CA), advancing contact angle (Adv.), receding contact angle (Rec.) and rolling–off angle as a function of the content of Ag flakes; (b) the effects of Ag flakes on the electrical resistance.

The surface adhesion of the oil droplet on the conductive micropillars was first studied at room temperature. The adhesion forces were measured on the composite micropillars by first bringing a hanging droplet using a micro-indentation instrument in which the oil droplet was hung on the bottom section of the regular hemispherical probe as shown in Figure 5.5. At the starting point, a notable contact between the droplet and substrate was established by bringing the droplet to the surface (Figure 5.5a). The droplet holder was then moved upward, causing a decrease in contact area between droplet and substrate (Figure 5.5b) until a finite contact spot was reached (Figure 5.5c). Beyond this point, the droplet detached from the surface (Figure 5.5d) without any residues on the substrate. The force was monitored during the separation process. Figure 5.5e is one typical force curve, showing the forces increasing with time and suddenly dropping at the detachment. The force at the peak point is the maximum force that needs to be overcome in order to detach the oil droplet from the prepared surface; it is directly related to droplet adhesion at the surface. This maximum droplet adhesion force was measured on micropillared surfaces with various fractions of Ag flakes, as shown in Figure 5.5f. At the lowest content of Ag flakes (45 wt%), the measured adhesion force was 0.064 mN while the adhesion force rose from 0.069 mN to 0.082 mN when the fractions of Ag flakes increased from 50 wt% to 65 wt% (Figure 5.5e). The increase in the adhesion forces reflects the slight decrease in the surface oleophobicity. Overall, the adhesion forces on the micropillared surface were small, in comparison with those on the flat surface where the oil droplets spread and were not be able to be detached from the surface. Those observations verified that the constructed epoxy/Ag flakes micropillars have low surface adhesion to oils and excellent self-cleaning property, suggesting their potential for de-freezing.

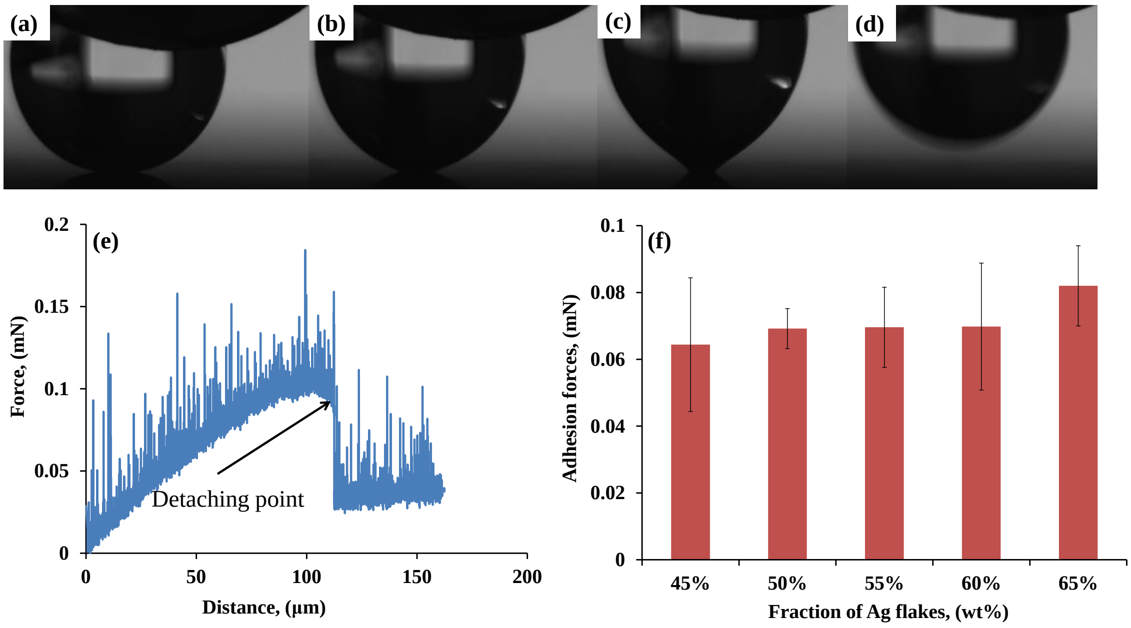

Figure 5.5. (a) to (d) optical images of the droplet contacting and detaching from the surface of the composite micropillars; (e) one typical force curve of detaching the droplet from the composite micropillars; (f) the measured adhesion forces from the prepared samples with varying Ag flakes fractions from 45% to 65%.

5.3.3 Effects of Oleophobicity and Resistance on Frozen Oil Separation

For de-freezing, the conductive micropillars were activated by passing electrical current so as to induce the Joule heating effect on each individual pillars. To investigate the effects of passing electrical current on the adhesion of frozen oil on micropillared surface, as illustrated in Figure 5.6a, the oil droplet was frozen at –25 ºC in a sealed chamber which is controlled by the thermoelectric temperature controller. To quantitatively characterize the adhesion of the frozen droplet, the droplet was knocked off from the surface. In the knock-off experiments (Figure 5.6b), a gap distance of 0.1mm between the probe and substrate surface was kept to avoid scratching the substrate surface. The probe moved horizontally to knock off the frozen oil droplet at a constant speed of 0.1 mm/s. In this study, two different heat sources were utilized: the "bottom-up" heating (Figure 5.6c) caused by DC current flowing through conductive micropillars and the "top-down" heating (Figure 5.6d) from the hot air applied over the droplet. In Figure 5.6c, a DC current flowed from right to left. Thus, the right side of the sample was heated up first because of the current density at right side is larger than the left side. It was observed that the right side of the droplet melted first; the solid-solid contact changed into solid-liquid contact, and the melting line (dash line in Figure 5.6c) moved gradually with continuously applied DC current (Figure 5.6c). The melted droplet sat on the surface without wetting the micropillars. This way is expected to be more efficient at reducing the adhesion of frozen oil because the joule-heating is directly applied to the interface between the frozen droplet and the surface. In contrast, applying heat from hot air will melt the outer layer of the droplets before moving to the interface (Figure 5.6d).

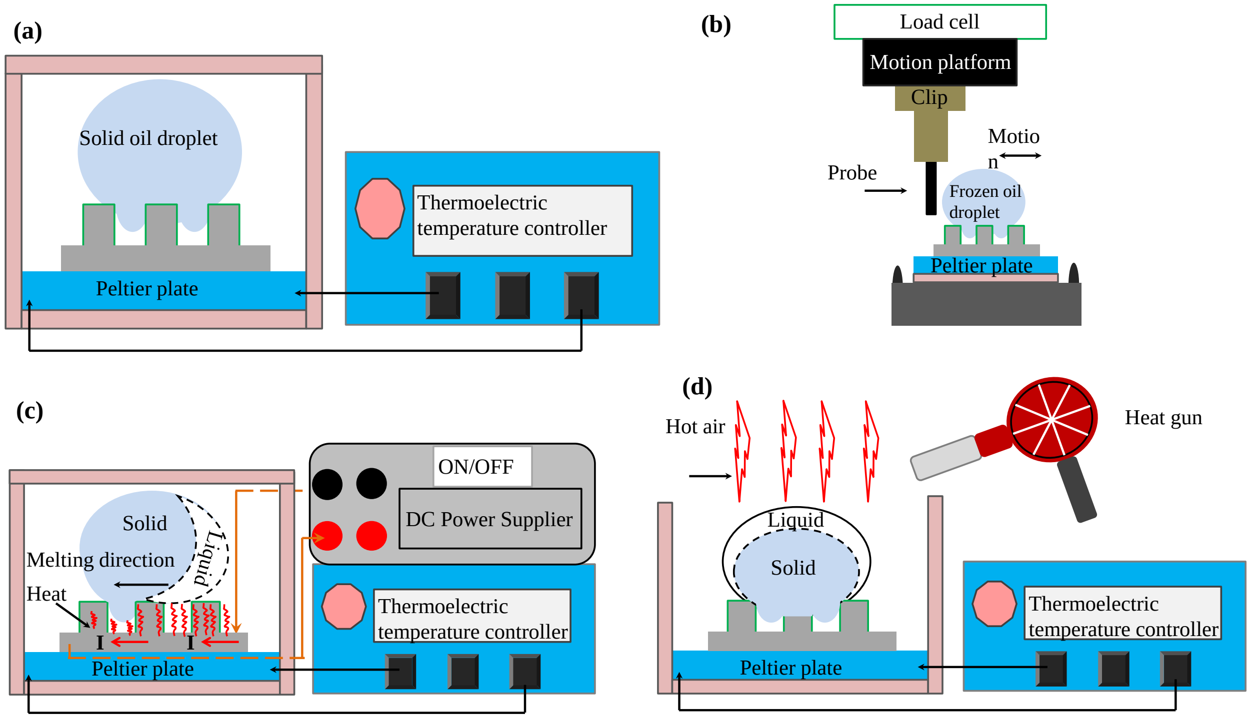

Figure 5.6. (a) the oil droplet frozen on the surface of micropillars with a slight penetration in a closed chamber controlled by a Peltier plate; (b) experiment set–up of knocking–off frozen oil droplet; (c) schematics of the oil droplet melting when a DC current passed the micropillars and the melted droplet retrieved to Cassie state; (d) schematics for the hot air melting method of a frozen oil droplet.

The knock-off forces of the frozen oil droplet from both flat and micropillared samples were measured and compared after a certain period of passing the DC current. Figure 5.7a is a typical knock-off force curve on the micropillared surface at –25 ºC without passing electrical current; the oil was fully frozen and the force sharply decreased to 0 once the droplet was knocked off. Figure 5.7b is a typical knock-off force curves on the same micropillared sample which was heated up to by passing the current. The frozen droplet partially melted at the interface and the knock-off force curve became broaden and decreased gradually. The maximum force during the knock-off process was used and labeled as “knock-off force”.

Tests were performed on three types of samples to demonstrate the effect of surface heating in terms of the knock-off force after passing the 1A DC electrical current for 2 min: epoxy/Ag flakes (45 wt%) composite flat surface, epoxy/Ag flakes composite micropillars with 45 wt% and 65 wt% Ag flakes. Figure 5.7c shows the knock-off force of the frozen droplet on the flat surface is 0.72 N while the knock-off force on the micropillared surface was reduced by more than 4 times at only 0.15 N, suggesting that high oleophobicity caused by the micropillars has a remarkable effect on reducing oil adhesion. Figure 5.7d compares the knock-off force on the composite micropillars with 45 wt% and 65 wt% Ag flakes. After applying 1A DC current for 2 min, the adhesion force on composite micropillars with 45 wt% Ag flakes was 0.15 N while the adhesion force on composite micropillars with 65 wt% Ag flakes was 0.42 N. The micropillars containing 45 wt% Ag had a higher electrical resistance (as shown in Figure 5.4b) and can deliver a larger amount of heat, thus were more effective in reducing the adhesion between the frozen droplet and the surface. The epoxy/Ag flakes composite micropillars sample with 45 wt% Ag flakes was chosen in the following detailed studies. We examined the effect of surface temperature on the knock-off force and compared it with “top-down” heating from the hot air.

The relationship between surface temperature and DC current time was plotted in the in-set figure in Figure 7e indicating the surface temperature increased when the DC current time was prolonged. As shown in Figure 5.7e, the force required to knock off the frozen oil droplet at –25 ºC was 0.4 N; the knock-off force was reduced to 0.15 N and 0.05 N when the sample surface was heated up to -18 ºC and -15 ºC, respectively. When the surface was heated up to –10 ºC, the knock-off force was almost zero, implying that the frozen oil can be removed from the surface very easily without fully melting. The hot air induced frozen oil adhesion reduction was performed on the same sample. Even though the surface was heated up to –5 ºC, the knock-off force was still measurable at 0.03 N. These results indicate the heating effect from DC current is indeed much more effective than blowing hot air.

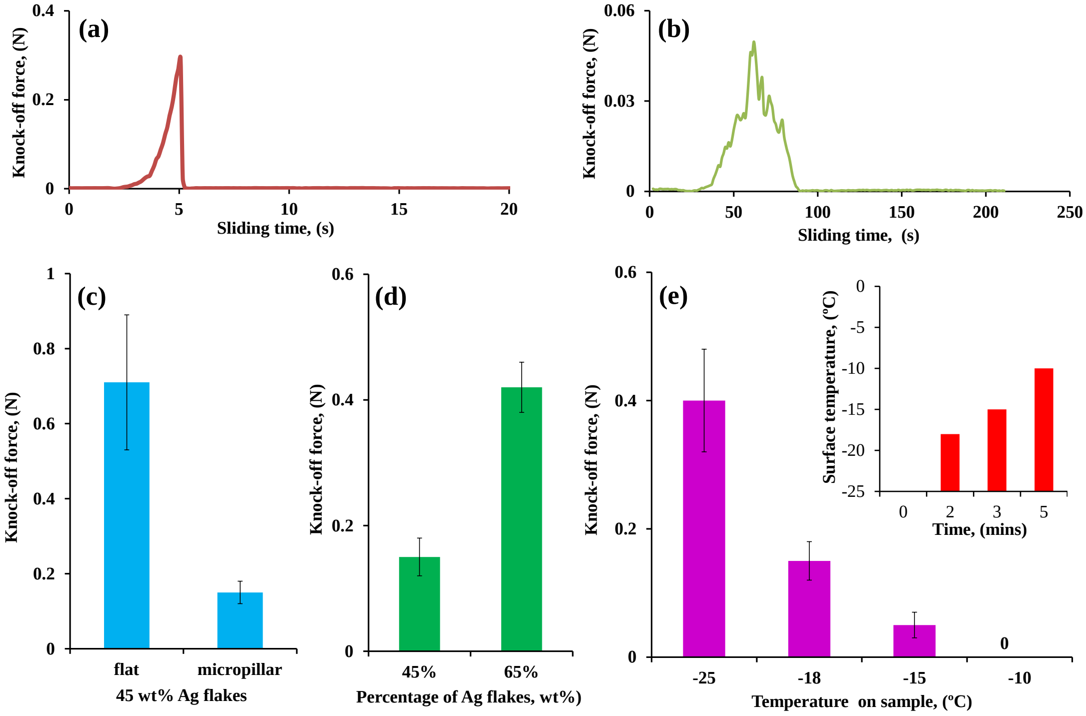

Figure 5.7. (a) typical force curve of knocking off a frozen droplet at –25ºC (b) typical force curve of knocking off a frozen droplet on the surface heated up to –15 ºC by applying DC current; (c) the effects of micropillar–enabled oleophobicity and (d) the effect of surface electrical conductivity on frozen oil adhesion reduction after applying 1 A DC current for 2 mins; (e) the decrease of the knock-off force as a function of surface temperature increasing via the 1 A DC current and the in-set figure illustrates the surface temperature as a function of time. Note that the knock-off force reached zero at the surface temperature of –5ºC when applying the hot air.

To obtain further insights into the effectiveness of de-freezing by passing currents to the conductive micropillars, the surface melting process of frozen oil droplet on micropillars with 45 wt% Ag flakes was observed by an optical microscope. Instead of beading up on the micropillars, the frozen oil droplet showed an elliptical shape at –25 ºC (Figure 5.8a). This is because the liquid oil droplet partially penetrated into the micropillars and spread slightly during the freezing process. After DC current was applied on the substrate, the frozen oil droplet started to melt at the surface from right to left (Figure 5.8b). The dash line in Figure 8b is the liquid-solid boundary between liquid oil and frozen oil droplet, indicating the melting direction of the frozen oil droplet. In addition, the shape of the droplet changed from elliptical-like shape to spherical-like shape (Figure 5.8b) because of the liquid surface tension. This phenomenon became more apparent when more and more of the frozen droplet was melted (Figure 5.8c) and the droplet beaded up on the micropillars, recovering its superoleophobic state after it completely melted (Figure 5.8d). After the oil droplet completely melted, the self-cleaning property was checked by measuring the rolling-off angle. As illustrated in Figure 5.8e, the liquid oil droplet slid off from the surface at the tilting angle of 19º which is slightly larger than the initial rolling-off angle at room temperature. This might be because of the water moisture depositing on the micropillars and forming a thin layer of frost which prohibited the sliding of oil droplet on the micropillars. Aside from this minor difference, this result shows that the melted oil droplet can be easily rolled off from a superoleophobic micropillar surface after passing the current.

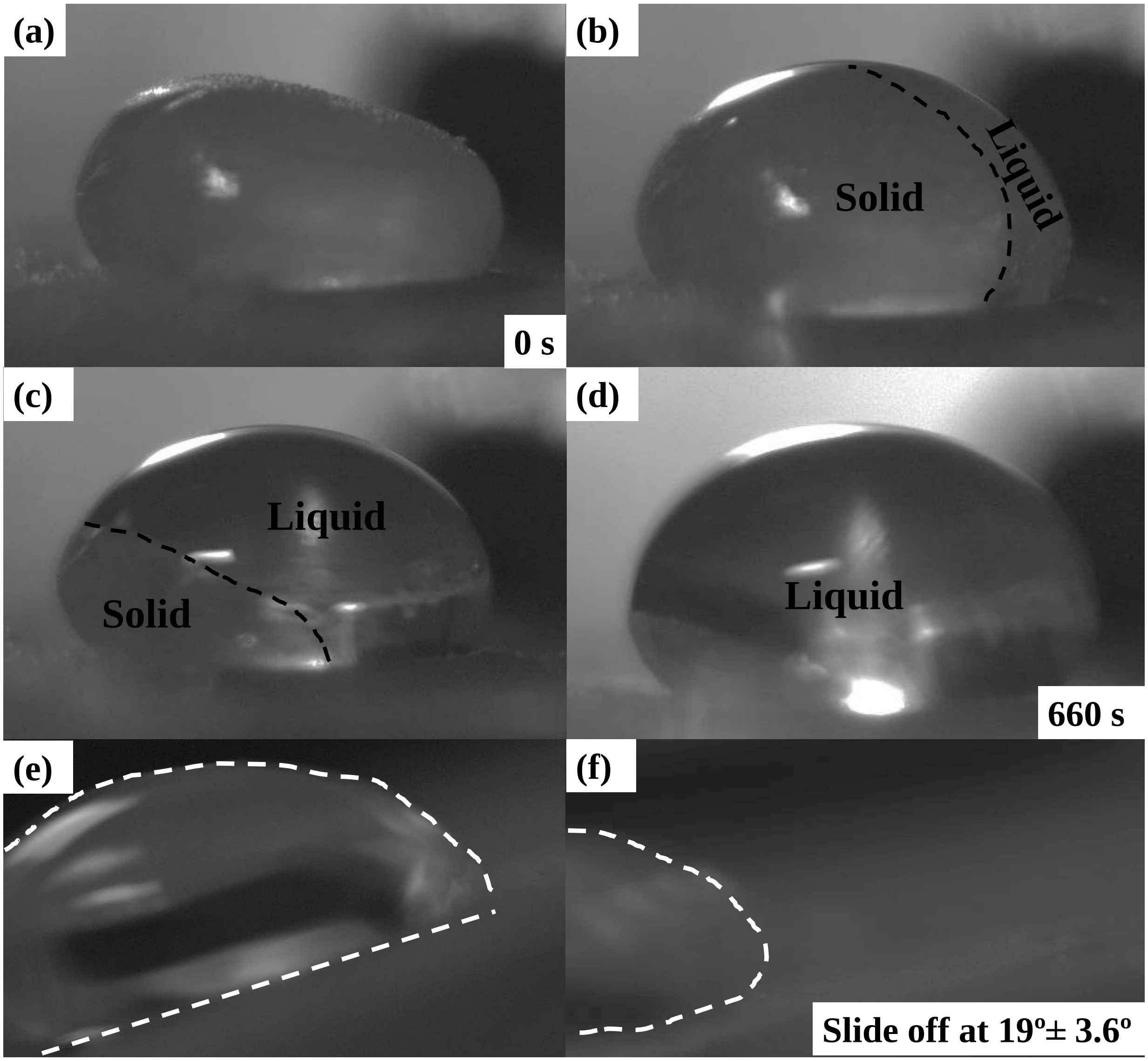

Figure 5.8. A sequence of optical images showing the melting process of frozen oil droplet after applying 1 A DC current from the initial frozen state (a) to completely-melted state (b) after applying the current; the frozen oil droplet was heated up from the bottom; and melting moved from right to left (b) to (c) corresponding to the direction of current flow; (d) the melted droplet beaded up; (e) the melted liquid droplet started to move when the substrate was tilted to a certain angle and then (f) slid off from the substrate at a roll-off angle of about 19º.

5.4. Conclusions

In summary, we reported the development of electrically conductive and superoleophobic micropillars for oil adhesion reduction at low temperatures. Micropillars were constructed from epoxy/Ag flakes composites via a two-step pattern transfer method. Superoleophobicity and self-cleaning properties were obtained by the micropillars and the embedded monolayer of FDTS on the surface of micropillars. The surface adhesion property was evaluated via the separation of a liquid droplet from micropillar surface showing the adhesion force to be as low as 0.069 mN. The electrical conductivity was originated from the added Ag flakes; the measured resistance decreased significantly by adding more Ag flakes. The DC current induced heating effect was found to be more significant on samples with high resistance and better oleophobicity; the larger the resistance and oleophobicity, the better it reduced the frozen oil adhesion. DC current induced melting is “bottom-top” melting and the solid-solid contact transferred into solid-liquid immediately reducing the frozen oil adhesion. In contrast, hot air melting is “top-bottom” melting and the solid-solid contact remained until the melting reached the bottom retaining the frozen oil adhesion. Thus DC current has better effects on reducing frozen oil adhesion than hot air. After the frozen oil droplet melted completely, it readily rolled-off from the surface. The research findings demonstrate an innovative type of materials-conductive-superoleophobic micropillars to help meet the needs for eliminating the ice/frozen oil from the surfaces in frigid areas.

Chapter 6. Durable Microstructured Surfaces: Combining Electrical Conductivity with Superoleophobicity

6. 1. Introduction

Electrically conductive materials with certain structures play a crucial role in both human and industry activities in the field of smart sensors,[61] actuators,[220] energy storage,[62] electromagnetic shielding,[63] light emitting diodes,[221] and so on. During the past decades, metallic devices with patterned structures have been widely used owing to their particular electrical conductivity.[67] However, metallic devices have lagged behind in practical applications because of their apparent disadvantages such as poor mechanical properties,[68] ease of corrosion,[73] and difficulty in constructing complex micro-/nanostructures.[222-225] Meanwhile, the rapid growth of microelectronics requires miniaturized structures with multiple functionalities (e.g., durability,[222, 223] stretchability,[69-72] flexibility,[72] and chemical stability[225, 226]. Therefore, polymer elastomers with remarkable elasticity,[76] processability,[77] and chemical stability[78] are regarded as promising alternative materials. Nevertheless, most elastomers are electrically nonconductive.[225] Hence, initial attempts have centered on patterning metallic structures on elastomers surface, but the weak adhesion and incompatibility between metals and elastomers limit their applications.[228-230]

To address this problem, various studies have been performed such as surface energy reduction,[231] etching,[232, 233] and conductive polymer composites (CPCs) fabrication.[79-81] Among these, CPCs integrate the advantages of both conductive fillers and polymer matrix

---

*This chapter has been published in *ACS Applied Material & Interfaces* **2016**, *31*, 9901-9910.

stretchable,[212] wear-resistant,[135] and chemically stable natures.[81] Polydimethylsiloxane (PDMS), as a typical elastomer, plays an important role in CPCs systems due to its distinctive properties, including biocompatibility,[140] mechanical flexibility,[70] and ease of structure construction.[140] Though PDMS is insulating, the transformation between insulation and conduction can be achieved by adding conductive fillers.[139] Niu et al.[140] developed microstructured PDMS-based electrical conductive composites by mixing 83.2 wt % of silver flakes into PDMS with a resulting conductivity of around 2×10^{-4} S/m. This large amount of added conductive fillers may aggregate causing high viscosity, poor mechanical properties, and fluidity as well as the high manufacturing cost.[234] To retain the properties of elastomers and reduce the usage of conductive fillers, Xu and Zhu[135] reported a highly conductive and stretchable conductor with conductivity of 81.3 S/m by embedding Ag nanowires into flat PDMS.

The rapid progression of microelectronics expands their applications to many fields[138, 141, 235] such as smart textiles[235] in which the surfaces are easily contaminated by water and oily liquids; thereby water/oil repellent surfaces are highly desired for anticontamination and antisticking properties.[138, 141, 235] The fabrication of superhydrooleophobic surfaces follows the rules of surface energy reduction and micro-/nanopatterns construction.[20, 30, 236] Fluoropolymers with a high ratio of $-CF_3$ and $-CF_2$ functional groups are reported to have much lower surface tension and are broadly used to reduce the surface energy.[20, 174, 199] Patterned structures such as micro-/nanopillars[174, 237] and overhang structures[199] have been constructed to obtain superoleophobicity. However, these superoleophobic materials are insulating, which cannot be used in electronics directly.[23] Thus, there is an increasing need for the development of advanced materials with surfaces that are both electrically conductive and superoleophobic.[234, 235] Wang et al.[137] reported the fabrication of conductive and superhydrooleophobic fabrics modified by fluoropolymers showing an oil contact angle of 156°. Das et al.[141] studied the effects of carbon nanofibers (CNFs) on the conductivity and superoleophobicity of composites. The nanocomposites were transferred from oleophobic to superoleophobic as the content of CNFs increased to 60 wt % with the conductivity of 1×10^3 S/m. Although electrical conductivity can be achieved by blending conductive fillers into polymer elastomers, the high loading of conductive fillers influences their mechanical performances and leads to high manufacturing cost.[138, 141, 235]

In this article, we report the development of multifunctional microstructured surfaces that are electrically conductive and superoleophobic. Our systems have three unique advantages: (1) the oleophobicity was constructed on Ag nanowires and Ag flakes embedded microstructures; (2) our systems require fewer amounts of conductive fillers; (3) our systems are mechanically durable and stretchable conductivity was achieved. They are designed and fabricated through embedding Ag flakes (SFs) and Ag flakes/Ag nanowires (SNWs) hybrid conductive fillers into the microstructures of the trichloroperfluorooctylsilane (FDTS)-blended PDMS via a modified pattern transfer approach. The surface patterning and migration of FDTS in the PDMS blend were exploited to deliver the superoleophobicity, which is a desirable property for inhibiting the surface contamination by water and oily liquids. In comparison to the common way to disperse conductive fillers into polymers or coating on flat surfaces, a much less amount of the conductive fillers is needed for delivering conductivity in this study, since only the surface microstructures are needed to be filled. The possible synergetic effects of using both SFs and SNWs were exploited by varying the SFs/SNWs ratio in the hybrid conductive fillers: the SFs are cost-effective and have been widely used in electrically conductive polymer composites, while SNWs are innovative nanomaterials having high aspect ratio and forming conductive networks readily.

We found that a significant improvement of the conductivity was obtained by using Ag nanowires to bridge or connect the Ag flakes so as to form a more effective electrical pathways. These conductive fillers were found to bond strongly with microstructures and retain surface properties under a high scratching load. The relationship between the applied strains and the resistances was further investigated on both SFs and SFs/SNWs embedded microstructured FDTS-blended PDMS surfaces that showed highly stretchable and reversible electrical properties.

6.2 Experiments Section

6.2.1. Materials

Polydimethylsiloxane (PDMS, Sylgard 184) and curing agent were purchased from Dow corning and were used as PDMS base and hardener, respectively. The weight ratio of PDMS to curing agent was 10:1. Trichloro (1*H*,1*H*,2*H*,2*H*-perfluorooctyl)silane (FDTS, 97%), glycerol ($\gamma = 64.0$ mJ/m^2), formamide ($\gamma = 58.0$ mJ/m^2), and silver flakes (SFs) were purchased from Sigma-Aldrich. Silver nanowires (SNWs, SLV-NW-90, average dimensions of diameter × length, 90 nm × 25 μm) were purchased from Blue Nano. Isopropanol (IPA, 99%, Aldrich) was used as a solvent to disperse SFs and SNWs. FDTS was used as surface energy reduction agent to functionalize PDMS, SFs, and SNWs with oil repellent properties. SFs and SNWs were utilized to modify the surface with electrical conductivity. Sand papers (80 coarse, Garnet sand paper, Mastercraft, Canada) were used as the template to make microstructures and embed conductive fillers into FDTS blended PDMS. All materials were used as received without any further treatment.

6.2.2 Sample Fabrication

To prepare SFs and SNWs embedded electrically conductive and superoleophobic (ECS) microstructured PDMS, four different amounts of SFs were dispersed into 1 g of isopropanol forming SFs suspensions with varying concentrations (66.7, 83.30, 100.0, and 125.0 mg/mL) followed by vortexing. Different amounts of SNWs were added into SFs to prepare the 125.0 mg/mL solution with SNWs fractions of 2%, 5%, 8%, and 11% by weight, respectively. 400 μL of the solution was deposited onto the sand paper using an autopipet (10–100 μL, Fisher Scientific). Sand paper was utilized as received. Isopropanol suspension containing SFs and SWNs was spread on the sand paper, fully wetting it and carrying SFs and SNWs into the bottom of the cavities. After the isopropanol fully evaporated, 6 g of FDTS-blended PDMS solution was poured onto the dried surface. Then the samples were moved into a desiccator for degassing. During the degassing process, air bubbles were eliminated and FDTS-blended PDMS solutions flowed into the cavities of the sand paper and the gaps between SFs and SNWs. This leads to the SFs being embedded into the bulk FDTS-blended PDMS solutions forming strong bindings. Then the samples were put into an oven for curing at 90 °C for 1 h. After curing, the samples were gently peeled from the sand paper, obtaining the conductive fillers modified FDTS-blended PDMS microstructured hierarchical surfaces with electric conductivity–superoleophobicity. The surface coverage of SFs and SFs/SNWs of prepared samples is shown in Table 6.1. The length of the prepared samples ranged from 45 to 49 mm, while the width ranged from 17 to 19 mm.

Table 6.1 Surface coverage of SFs and SFs/SNWs embedded microstructured samples via pattern transfer approaches.

Conductive fillers	SFs (mg)	Surface coverage (mg/mm^2)	Thickness of composite layer (μm)
Silver flakes (SFs)	26.67	$3.0 \times 10^{-2} \pm 1.4\times 10^{-3}$	20.2 ± 0.6
	33.33	$4.0 \times 10^{-2} \pm 2.0\times 10^{-3}$	28.5 ± 1.2
	40.00	$5.0 \times 10^{-2} \pm 3.0\times 10^{-3}$	29.8 ± 1.0
	50.00	$6.0 \times 10^{-2} \pm 2.8\times 10^{-3}$	30.0 ± 1.1
Silver flakes (SFs) and silver nano wires (SNWs)	SFs/SNWs (%)	Surface coverage (mg/mm^2)	Thickness of composite layer (μm)
	98/2	$6.0 \times 10^{-2} \pm 2.8\times 10^{-3}$	30.0 ± 1.0
	95/5	$6.0 \times 10^{-2} \pm 2.5\times 10^{-3}$	30.0 ± 0.9
	92/8	$6.0 \times 10^{-2} \pm 3.2\times 10^{-3}$	30.0 ± 1.3
	89/11	$6.0 \times 10^{-2} \pm 3.8\times 10^{-3}$	30.0 ± 1.5

6.2.3 Method

Surface morphologies of SFs and SNWs embedded ECS PDMS samples were investigated via field emission scanning electron microscopy (FE-SEM, LEO-Ultra, GEMINI, Germany). The durability of the conductive fillers embedded PDMS surfaces was evaluated by performing sliding tests in an universal material tester (UMT, UNMT-2MT, by Center for Tribological Inc.) with varied preloads from 0.5 N to 8.0 N. The friction forces and coefficient of friction were recorded. All of the sliding tests were done at room temperature with the sliding speed of 0.1 mm/s and were tested on three different points on each sample of the three prepared samples. Stretching tests were performed using UMT. The sample was installed between the moving stage and the sample gripper. The UMT pulled the sample until different strains were reached. The resistance measurements were taken via a two-point probe system and a source meter (Keithley 2440 5A source meter, Keithley Instruments Inc.) at various strains while applying the stretch test. These measurements were tested on two different points on each sample of the three prepared samples.

The oleophobicity of the as-prepared samples was characterized by measuring the static oil contact angles which were performed in a sessile drop system. The liquid probes selected for the oleophobicity test were glycerol and formamide. The oil contact angles were collected from three different spots on three samples. The contact angle was calculated by fitting profiles using a custom-made LabVIEW program. The resistances of SFs and silver NWs embedded FDTS-blended PDMS microstructured samples were measured via a two-point probe system and a source meter. The parameters for measuring the resistance were 100 μA for current and 10.5 V for voltage. The resistance of the samples was measured at three different points on three separated samples.

6.3. Results and Discussion

The surface morphology of the sand paper used as a template in this study is shown in Figure 6.1a. The size of the micropapillae-like microstructures was around 100 μm and resembles the surface structures of the lotus leaf at the microscale. More detailed information on the sand paper surface was obtained from optical profiles with a scanning area of 1.11 mm × 0.89 mm (length × width). Figure 6.1b is the three-dimensional (3D) image of the sand paper surface showing that micropapillae with different heights are distributed in the selected area with the maximum height of 57 μm. This can be verified from *x-y* profiles (Figure 6.1c), where three significant peaks and multiple small peaks can be seen on the surfaces. With this microstructure, sand paper was used as a mold to transfer patterns to elastomers. Additionally, sand paper is oleophilic and can be readily wetted by oily liquids such as isopropanol. Thus, the conductive fillers can deposit on it during the wetting process.

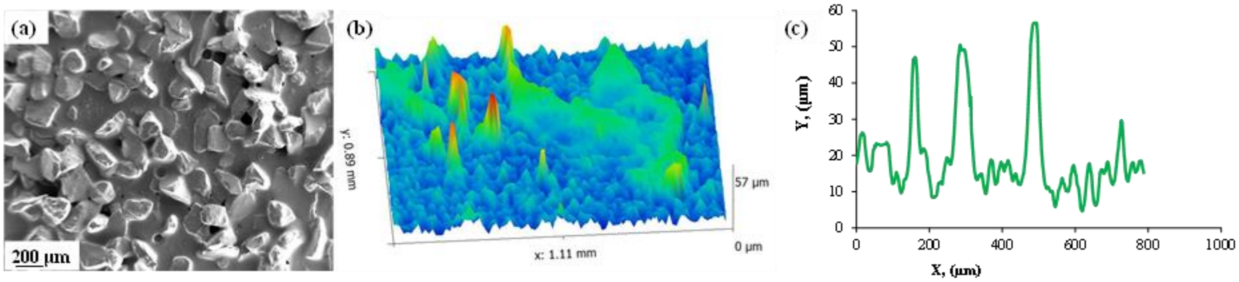

Figure 6.1. (a) SEM images of surface morphology of the sand paper with micropapillae structure; (b) three dimensional (3D) surface profile of the sand paper surface took by optical profilometer indicating, the different height micropapillae; (c) x-y profiles of the sand paper provides the height variations of these micropapillae.

The microcontact printing method (μCP)[79] has been reported to be one of the most common and efficient approaches for integrating conductive fillers to patterned polymer surfaces. However, it involves fabrication of patterned elastomers, surface etching, microcontact steps and also requires specific etching solvent. In this study, we developed a technique to integrate the conductive fillers onto the microstructured surface in one step. To achieve this goal, mold transfer is applied due to its high efficiency and simple procedures. Although the mold transfer has been widely reported, there was little literature on hybrid surfaces with conductive fillers. In this paper, PDMS was chosen as the elastomer to transfer the structures from the sand paper. The procedures for preparing the SFs and SFs/SNWs embedded microstructured FDTS-blended PDMS surface were the same. SFs/SNWs embedded microstructured FDTS-blended PDMS surfaces were chosen as example to illustrate the fabrication process (Figure 6.2). First, the SFs/SNWs were dispersed into isopropanol forming conductive fillers suspension. Then the suspension was drop-coated onto the sand paper (Figure 6.2a). The isopropanol suspension wetted and spread on oleophilic sand paper, carrying the SFs/SNWs and depositing them onto the valleys after the evaporation of isopropanol (Figure 6.2b). Then the FDTS-blended PDMS resin was poured onto the SFs/SNWs coated mold; the resins penetrate and stuck to the conductive networks during the degassing process (Figure 6.2c). After curing, the microstructures and SFs/SNWs were transferred onto the FDTS-blended PDMS surface. The embedded conductive fillers made the surface rougher and formed secondary micro-/nanostructure (Figure 6.2d).

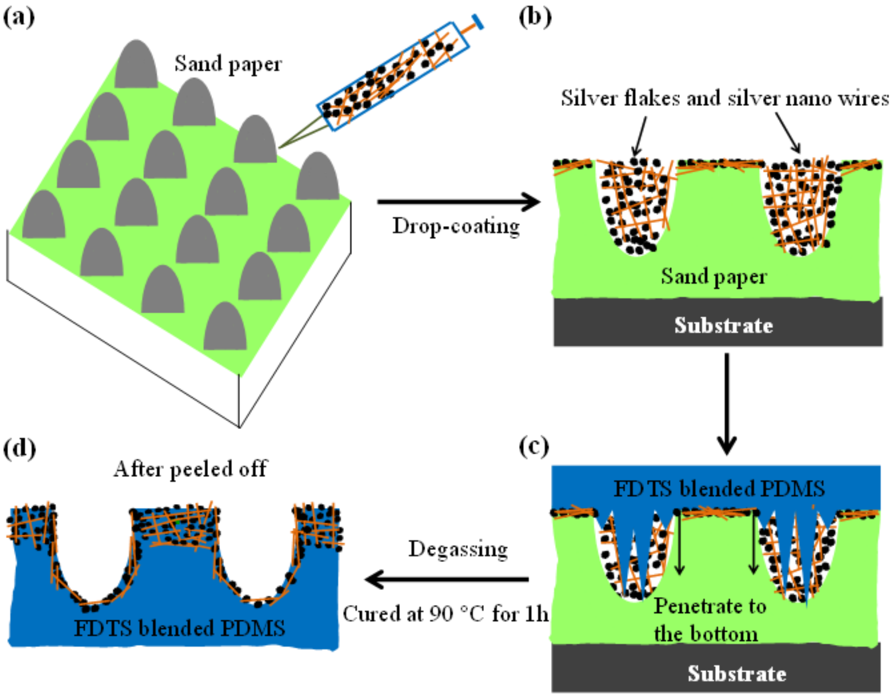

Figure 6.2. The schematic illustration of the fabrication of SFs/SNWs embedded FDTS-blended PDMS hierarchical structure: (a) SFs/SNWs were drop-coated onto sand paper, (b) SFs/SNWs coated the micropapillae after the evaporation of isopropanol, (c) FDTS-blended PDMS elastomers penetrated into the bottom of the cavities and stuck to the conductive networks during degassing, (d) SFs/SNWs embedded into FDTS-blended PDMS and the hierarchical microstructured surfaces were obtained after it cured and simply peeled off from the mold.

Furthermore, we noticed that these SNWs not only were embedded in the surface but also went to the bulk of PDMS (Figure 6.3 a, b), forming a conductive composite interfacial layer. SNWs were also covered by a thin layer of FDTS blended PDMS at the interface (Figure 6.3c);

thereby the SNWs were strongly held on the surface resulting in high conductivity. The FDTS migrated to the surface during the curing process, resulting in antiwetting property which was reported in our previous study.[174,199] This microstructure is quite similar to the surface of the lotus leaf which is composed of many waxy micropapillae covered with nanoprotrusions. The microstructured surfaces fabricated by the mold transfer and conductive fillers modification approach mimicked the hierarchical structures of the lotus leaf to a certain extent.

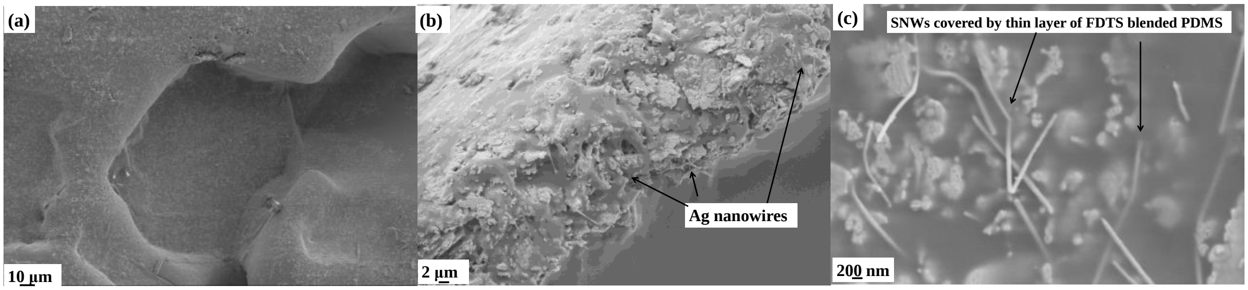

Figure 6.3. (a) SEM image of the top-view and (b) cross-sectional view of SFs/SNWs embedded FDTS-blended PDMS microstructured surface, showing that the SFs and SNWs were not only embedded at the surface but went into the bulk PDMS to a depth around 30 µm; (c) the SNWs were covered by a thin layer of FDTS blended PDMS (top-view).

The surface profiles of these microstructured surfaces were studied via SEM and optical profilometer, and the results were shown in Figure 6.4. The overall structure of FDTS-blended PDMS thin film has a significant amount of microgrooves or bumps (Figure 6.4a). Surface profiles of this surface were shown in Figure 6.4b and Figure 6.4c, with the significant valleys (varying from 10–20 µm) and micropeaks (several micrometers high) distributed on the surface indicating that the microstructures were transferred successfully. Figure 6.4 d–f showed the dependence of surface topology on the surface coverage of these conductive fillers. With an increasing coverage of embedded conductive fillers, the surface becomes rougher and rougher. The arithmetic mean surface roughness (R_a) and root-mean-square roughness (R_q) are used to describe the variation of the surface height. The values of R_a and R_q for Figure 5.4d are 6.89 and 9.62 μm, respectively, which are smaller than those of Figure 6.4e (with R_a and R_q of 8.51 and 12.38 μm, respectively). The R_a and R_q values in Figure 6.4f are slightly lower than those of Figure 6.4e due to the replacement of SFs by 11 wt % of SNWs. Figure 6.4 g–i are the corresponding SEM images of the surface morphologies of Figure 6.4 d–f. Figure 6.4g shows that at low surface coverage (3.0×10^{-2}mg/mm^2) the surface is not smooth and a secondary structure was constructed by the buried SFs without overlapping. With an increase of the surface coverage of SFs, the surface becomes rougher (Figure 6.4h). When the surface coverage of SFs was increased to 6.0×10^{-2} mg/mm^2, SFs started to overlap and form compact conductive composites layer. In order to further improve the conductivity, four different ratios of SNWs were used (2, 5, 8, and 11 wt %) at the surface coverage of 6.0×10^{-2} mg/mm^2. As it can be seen from Figure 6.4i, the SNWs are spread widely on the surface at the ratio of 11%, forming networks to connect or bridge the SFs. As a consequence, more conductive pathways were formed, compared to the pure SFs embedded surfaces.

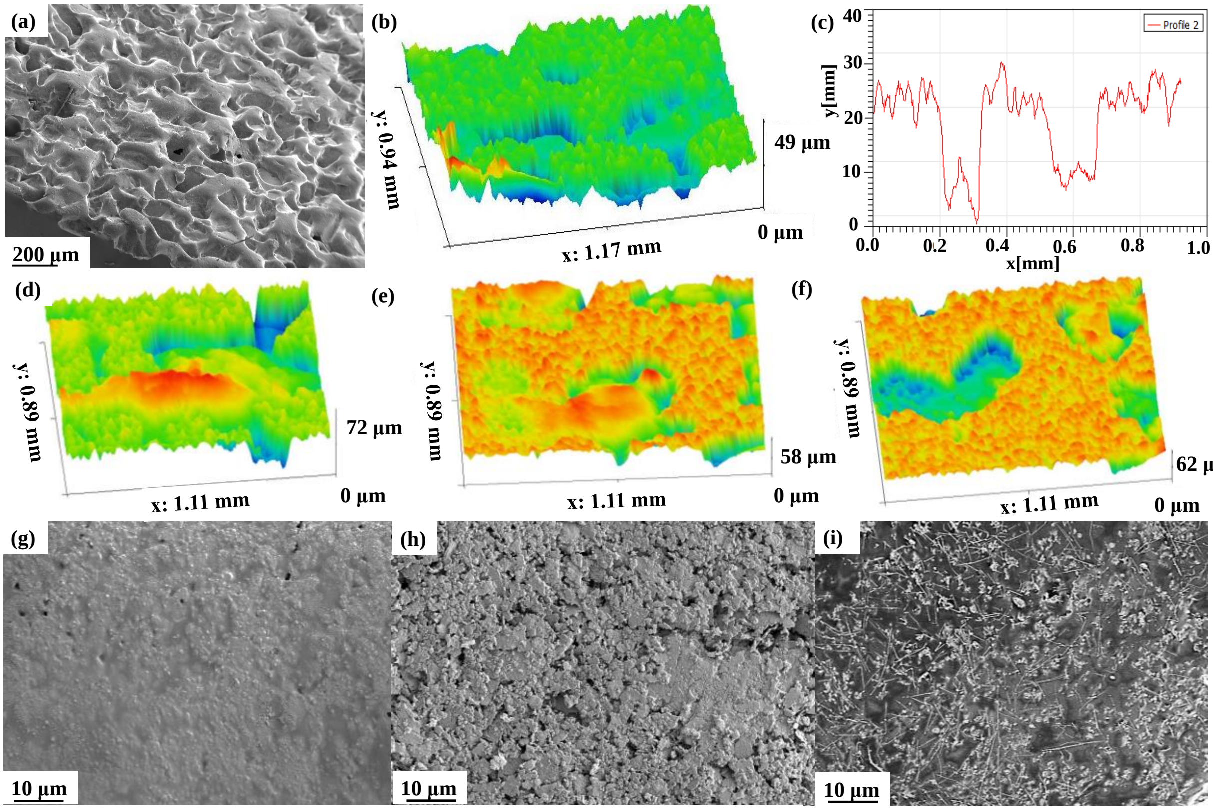

Figure 6.4. (a) SEM image of the overall structure of FDTS-blended PDMS microstructure from sand paper *via* mold transfer method; (b) the 3D surface profile of the obtained surface in (a); (c) the x-y profiles of obtained FDTS-blended PDMS microstructured surface; (d) to (f) are the 3D surface profiles of SFs embedded FDTS-blended PDMS microstructure surfaces at the coverage of 3.12 × 10^{-2} mg/mm^2, 5.94 × 10^{-2} mg/mm^2 and the 3D surface profile of SFs/SNWs embedded FDTS-blended PDMS at the SNWs ratio of 11%, respectively; (g) to (i) are the corresponding SEM images of surface morphologies in (d) to (f).

In order to quantitatively characterize the electrical conductivity, the electrical resistivity and conductivity were determined using the following equations:

$$\rho = R\frac{A}{L}\ (\Omega \cdot m) \qquad \text{Equation 6.1}$$

$$\sigma = \frac{1}{\rho}(S \cdot m) \qquad \text{Equation 6.2}$$

in which ρ is the resistivity, σ is conductivity. A, L and R are the cross-sectional area, length and the measured conductive resistance of the prepared samples. To determine the percolation of SFs embedded surfaces, a series of the samples have been fabricated at varied surface coverage from 1.0×10^{-2} mg/mm^2 to 6.0×10^{-2} mg/mm^2 (Figure 6.5); the percolation was found to be about 3.0×10^{-2} mg/mm^2. Above this percolation value, the conductivity increased from 5.14×10^3 S·m to 1.12×10^5 S·m as the surface coverage of SFs increased to 6.0×10^{-2} mg/mm^2.

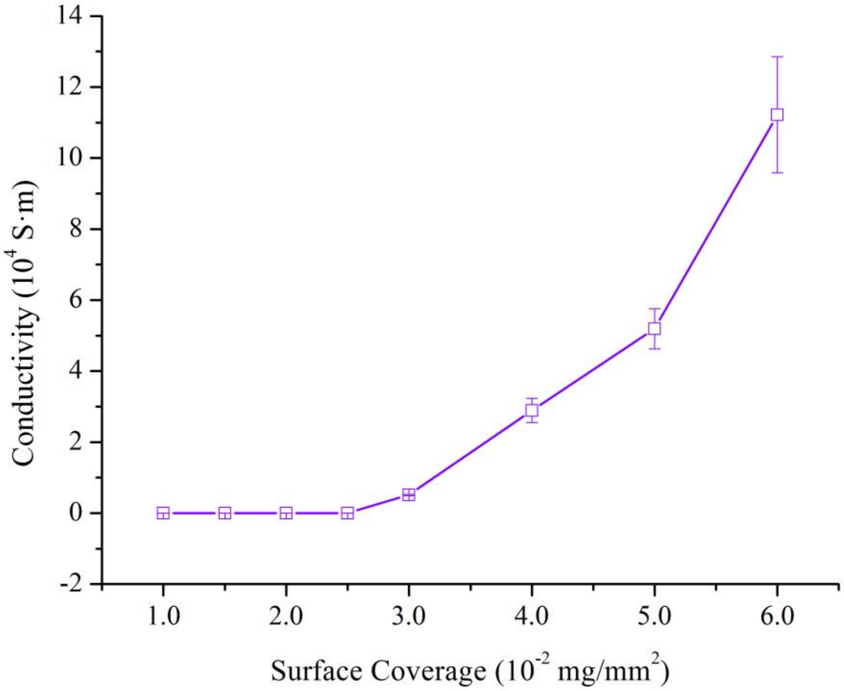

Figure 6.5. The dependence of conductivity on the surface coverage of SFs (Ag flakes). There is a turning-point at the surface coverage of 3.0×10^{-2} mg/mm^2 which is estimated as a percolation value of the SF_S for the conductive surface.

The effects of surface coverage of SFs and fraction of SNWs on the conductivity are plotted in Figure 6.6a and b, respectively. It can be seen that the surface coverage of conductive fillers has a significant influence on the conductivity. The constructed conductive samples were used as part of the electric circuits to light up the LED bulbs. As shown in Figure 6.6a, all of the bulbs can be lighted. At low conductivity, the bulb was lighted up with faint yellow because of the low electron density while it turned into bright white at high conductivity. These results imply that continuous conductive pathways for the migration of electrons have been formed; and the more the SFs were buried into the PDMS surface, the higher the conductivity was (Figure 6.6a).

Since Ag nanowires have much larger aspect ratio than Ag flakes, conductive pathways can be easily formed by Ag nanowires. By use of these high aspect ratio conductive fillers, the conductivity can be increased remarkably. Figure 6.6b illustrates the effect of different amounts of SNWs on conductivity with weight fractions of 2%, 5%, 8%, and 11% of SFs. Only 2 wt % of SNWs was used with the resulting conductivity of 1.17×10^5 S/m which was slightly higher than the largest conductivity of SFs embedded samples (Figure 6.6b). At this fraction, the bulb showed a bright white color indicating the high conductivity of such surface. The conductivity continued to rise with the increasing fraction of SNWs, and the largest conductivity, 3.07×10^5 S/m, was obtained at the highest fraction of SNWs (11%). The morphologies of SFs and SNWs are shown in Figure 6.6c and Figure 6.6d; the SFs are at the microscale, while the SNWs are several micrometers in length with the diameter of around 100 nm resulting in high aspect ratios. The conductivity differences between neat SFs and SFs/SNWs in polymer matrix can be explained from the aspect of the conductive pathway morphologies.[80, 81] Conductive fillers with low aspect ratio, such as SFs, are randomly distributed in the polymer matrix resulting in the less arranged conductive pathways. In contrast, the high aspect ratio conductive fillers SNWs can bridge the SFs and form segregated conductive network pathways.[80, 81] These network pathways provide sufficient channels for the motion of electronics, leading to high conductivity.

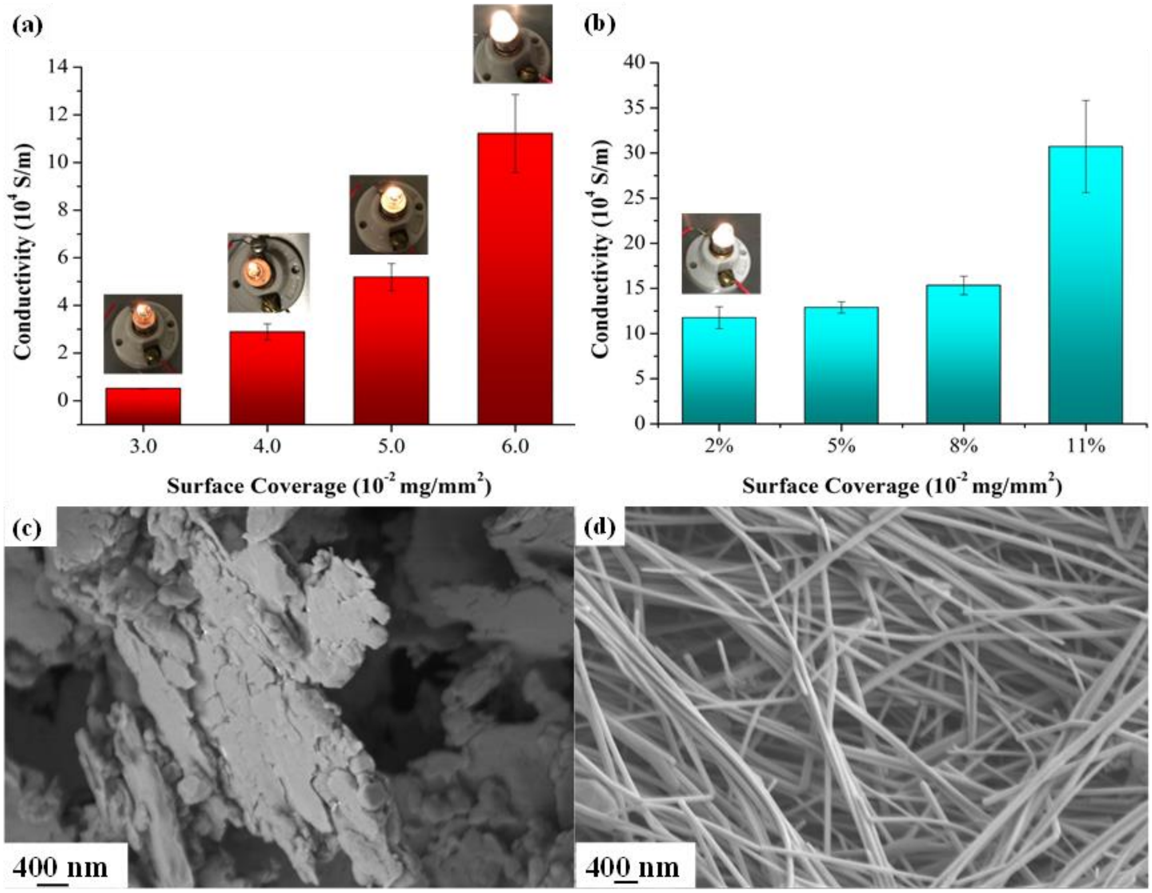

Figure 6.6. The conductivity of (a) SFs embedded and (b) SFs/SNWs embedded FDTS blended PDMS hierarchical microstructure surfaces; (c) and (d) are SEM images of SFs and SNWs respectively.

To verify the connections between pure SFs and SFs/SNWs hybrid fillers, the angle resolved backscatter characterization was performed and shown in Figure 6.7. Because metal has better electron reflectivity than polymer, the bright areas in Figure 6.7a are the overall conductive pathways formed by SFs/SNWs hybrid conductive fillers while the dark areas are PDMS matrix. These bright areas were well connected, confirming the conductive pathways constructed on the microstructured surfaces were obtained successfully. To further investigate the connection between SFs and SNWs, a high magnification image was shown in Figure 6.7b. The SNWs distributed on the surface forming networks, which can easily be observed, as seen in the marked areas in Figure 6.7b. These networks ensure the electrons pass through much more easily. Also, these networks connected the dispersed SFs resulting in the new electron pathways. The networks and the pathways formed by SNWs and SFs are responsible for the higher conductivity compared with the system only using SFs. Although it is beyond the scope of this work, it is worthwhile to note that the SFs/SNWs could be more stable under electrical current in comparison to the electrical networks formed solely by the SNWs, since the SNWs have small diameter and are subject to failures or breakup due to the joule heating effect or other instabilities.[236, 237]

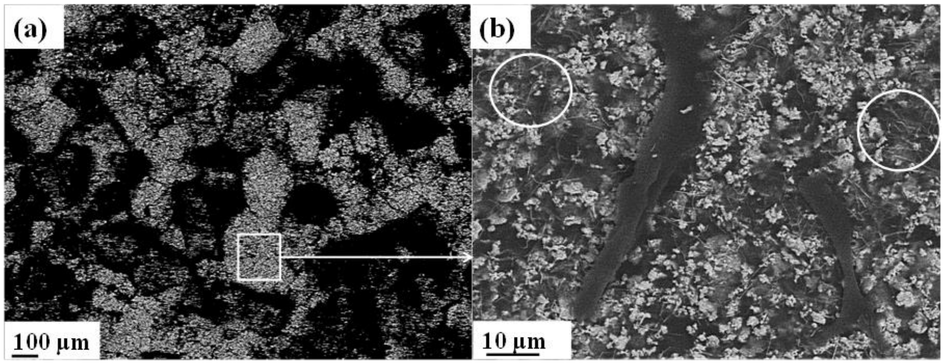

Figure 6.7. (a) angle resolved backscatter analysis of the conductive pathways formed *via* SFs and SNWs at a Ag NWs weight fraction of 11%; (b) high resolution analysis of the marked area in (a) showing that SNWs connect SFs resulting in the conductive networks.

The durability of the bonded conductive layer on PDMS is a major concern for its potential application. To evaluate the durability, friction/scratch tests were performed by sliding a probe across the surfaces at different preloads.[240] Comparative studies were carried on SFs embedded flat FDTS-blended PDMs surfaces (Figure 6.8a–c) and SFs embedded FDTS-blended PDMS microstructured surfaces (Figure 6.8d–g). The same amount of SFs (6.0×10^{-2} mg/mm^2) was coated on glass and sand paper for the flat and microstructured PDMS in order to make a comparison. After curing, FDTS-blended PDMS was gently peeled from the substrate for tests. As it shows in Figure 6.8a, the SFs were embedded into FDTS-blended PDMS, but lots of SFs residues were left on the glass slide. When performing friction test (with a preload of 0.5 N), two significant friction traces were found on the surface (Figure 6.8b). After further examination such as gently pressing the tape onto SFs embedded surface, considerable amounts of SFs were observed on the tape after it was detached from the surface (Figure 6.8c). This is because the SFs coated onto glass slide formed compact layers, preventing the penetration of FDTS-blended PDMS elastomer. The loose connection between SFs and PDMS led to an unconsolidated conductive layer. When performing the friction test, the top loose layer was scratched off. On the contrary, all of the SFs were buried into FDTS-blended PDMS after it peeled from the sand paper (Figure 6.8d and Figure 6.8e), since the microstructures of sand paper allowed the FDTS-blended PDMS to penetrate to SFs. The PDMS filled the gaps between conductive fillers resulted in a strong bonding between the conductive fillers and PDMS matrix. These strong interactions are responsible for the durability of the conductive fillers on top of FDTS-blended PDMS. There were no friction traces left on SFs embedded microstructure surface under the preload as high as 8.0 N (Figure 6.8f). Figure 5.8g shows the typical friction traces at each preload (from 0.5 N to 8.0 N), indicating the surface properties retained the same through the sliding process.

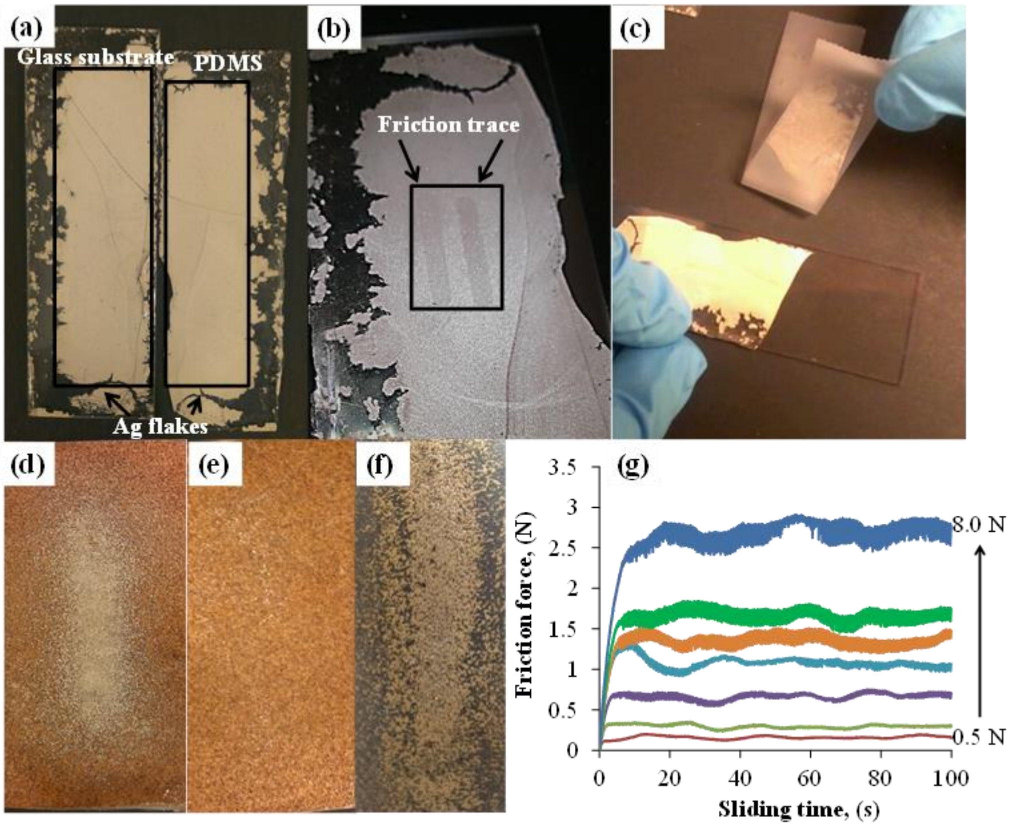

Figure 6.8. Durability comparison of the bonded conductive layer on flat FDTS-blended PDMS (a-c) vs microstructured FDTS-blended PDMS surface (d-g). (a) Optical images showing SFs on both the glass substrate and the peeled PDMS , (b) two friction traces left on the flat surface after sliding tests under the preload of 0.5 N, (c) removing of SFs by tape from the flat surface, (d) SFs coating on the sand paper, (e) optical image of the sand paper after the PDMS was peeled off, showing all SFs were transferred to the PDMS surface, (f) the obtained SFs embedded microstructured FDTS-blended PDMS surface, (g) the friction traces showing stable trends under varied preloads (from 0.5 N to 8.0 N) to verify the good bonding between SFs and microstructured FDTS-blended PDMS.

Note that there was a slight surface deformation when the probe slid across the samples because of the possible plastic deformation of FDTS-blended PDMS.[241] At the high preloads, there might be some discontinuous contacts during the sliding, which resulted in the fluctuation of the friction force forces.[242] Overall, the friction force appeared to linearly increase with the preload. To verify this, the coefficient of the friction was calculated and plotted in Figure 6.9. The coefficient of friction leveled at a stable value of 0.30 implies the buried conductive fillers bonded well to FDTS-blended PDMS without being scratched off from the surfaces.

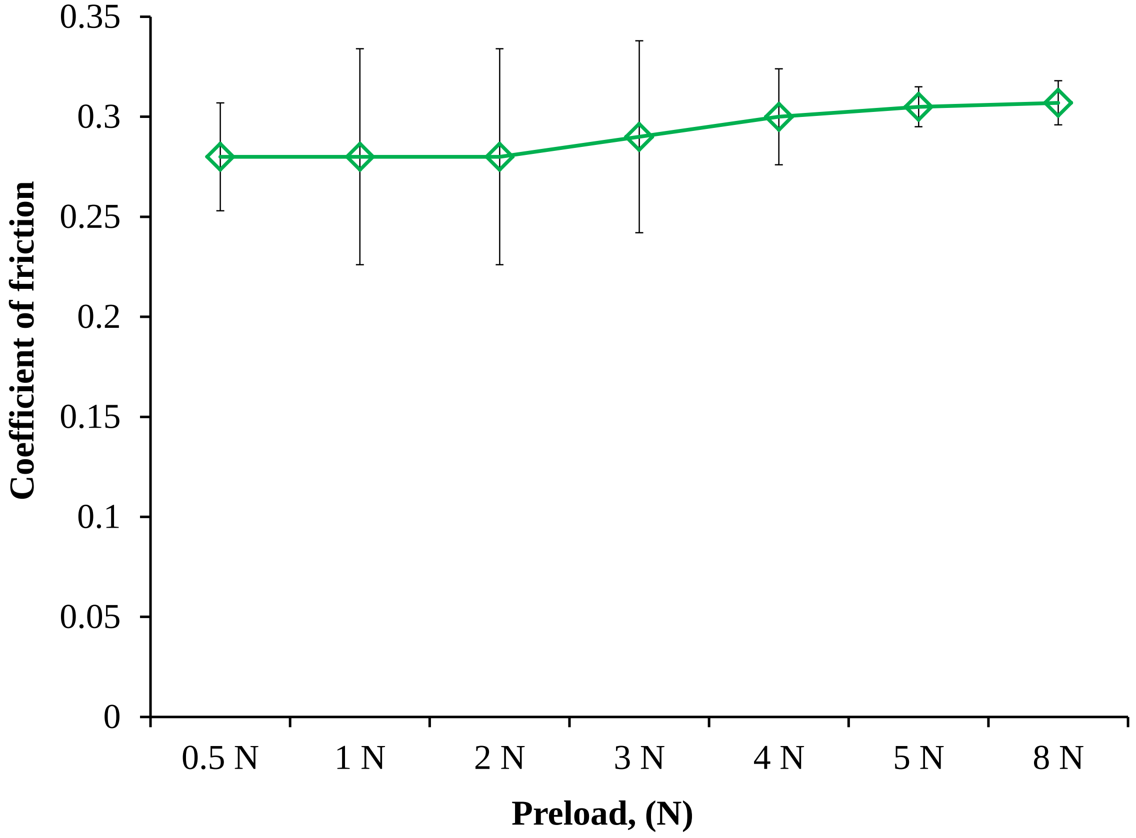

Figure 6.9. The coefficient of friction as a function of the preload. The coefficient of friction remained roughly constant with increasing preload, suggesting the good durability of the microstructured PDMS surfaces embedded with SFs.

After determining that the conductive fillers bonded strongly with FDTS-blended PDMS matrix, the stretchability of the samples was further tested (under the strain ranging from 0 to 40%) to get insights into their potential application in stretchable devices. Figure 6.10a and b describe the variation for resistance as a function of the applied strain of the microstructured FDTS-blended PDMS containing SFs and SFs/SNWs hybrid conductive fillers, respectively. Resistances were recorded at the same time as strain was applied. The data points in the figures were the average values of the resistances under varied strains while the solid curves were fitted by the following power-law relationship:

$$R = a + b \times \varepsilon^{c} \qquad \text{Equation 6.3}$$

in which, ε is the strain applied on samples, a is the vertical intercept, b is the slope and c is the power exponent. The parameters of each curve are listed in Table 6.2.

Table 6.2 The parameters of the fitted power-law of strain-resistance.

Conductive fillers	Surface coverage (mg/mm^2)	Parameters	Values	Standard Error
Ag flakes (SFs)	3.0×10^{-2}	a	21.4	2.40
		b	2465.9	827.90
		c	2.8	0.28
	4.0×10^{-2}	a	3.7	0.30
		b	523.5	68.43
		c	2.5	0.11
	5.0×10^{-2}	a	2.6	0.32
		b	405.9	262.23
		c	3.2	0.50
	6.0×10^{-2}	a	0.9	0.30
		b	72.0	25.94
		c	2.0	0.32
Ag flakes/Ag nanowires (6.0×10^{-2} SFs/SNWs)	98%/2%	a	0.7	0.07
		b	67.9	11.10
		c	2.1	0.13
	95%/5%	a	0.6	0.11
		b	53.6	12.05
		c	2.0	0.20
	92%/8%	a	0.6	0.03
		b	104.6	18.94
		c	2.8	0.17
	89%/11%	a	0.3	0.03
		b	12.8	2.39
		c	1.6	0.13

For all of the samples, the resistance increased almost exponentially with the increased strain, though it experienced a sharp increase at low surface coverage of SFs, when compared with resistances of high surface coverage (Figure 6.10a). Furthermore, the resistances of the sample with the surface coverage of 3.0×10^{-2} mg/mm^2 rise slightly at the range from 5% to 25%.

When the strain exceeds 25%, the resistance shows a remarkable increase; likely the applied stress stretched the electrical pathways to be partially disconnected. This is more significant when the strain rose to 30% (Figure 6.10a). Similar trends were observed on the samples with higher SFs coverage surfaces, but the amplitude of resistance increasing with the strain was smaller. The power exponents of the fitted power-law in Figure 6.10a are around 3.0. Figure 6.10b shows the resistance vs strain curves of SNWs/SFs hybrid filler modified surfaces. The overall trend is similar to the SFs modified FDTS-blended PDMS surfaces, with a power exponent of around 2, suggesting the resistances of the samples with SFs were more strongly influenced by the applied strains than those with SFs/SNWs. To explain these observations, the effect of strain on the change of the conductive pathways was illustrated in Figure 6.10 c and d. SFs overlapped in the elastomer, forming randomly conductive pathways at original state. Some overlapped SFs lose their connections due to the applied stress, causing discontinuities in conductive pathways, which lead to the increase in resistance. When high aspect ratio SNWs was added, additional conductive networks were formed and SFs were connected by the SNWs. Although the same strain applied on SNWs/SFs embedded FDTS-blended PDMS surface causes the separation of SFs, most of the SNWs were still under connections and the networks were not destroyed, which results in a slight increase in resistances (Figure 6.10d). Furthermore, we performed cyclic tests on SNWs/SFs embedded samples and found that after releasing the strains the resistances returned to almost same values before stretching (Figure 6.10e), implying the prepared samples are well stretchable. There is a small mechanical hysteresis observed in stress-strain loop of Ag flakes/Ag nanowires embedded PDMS microstructures, suggesting a slight plastic deformation of the microstructured PDMS may have occurred during the stretching. (Figure 6.10f).

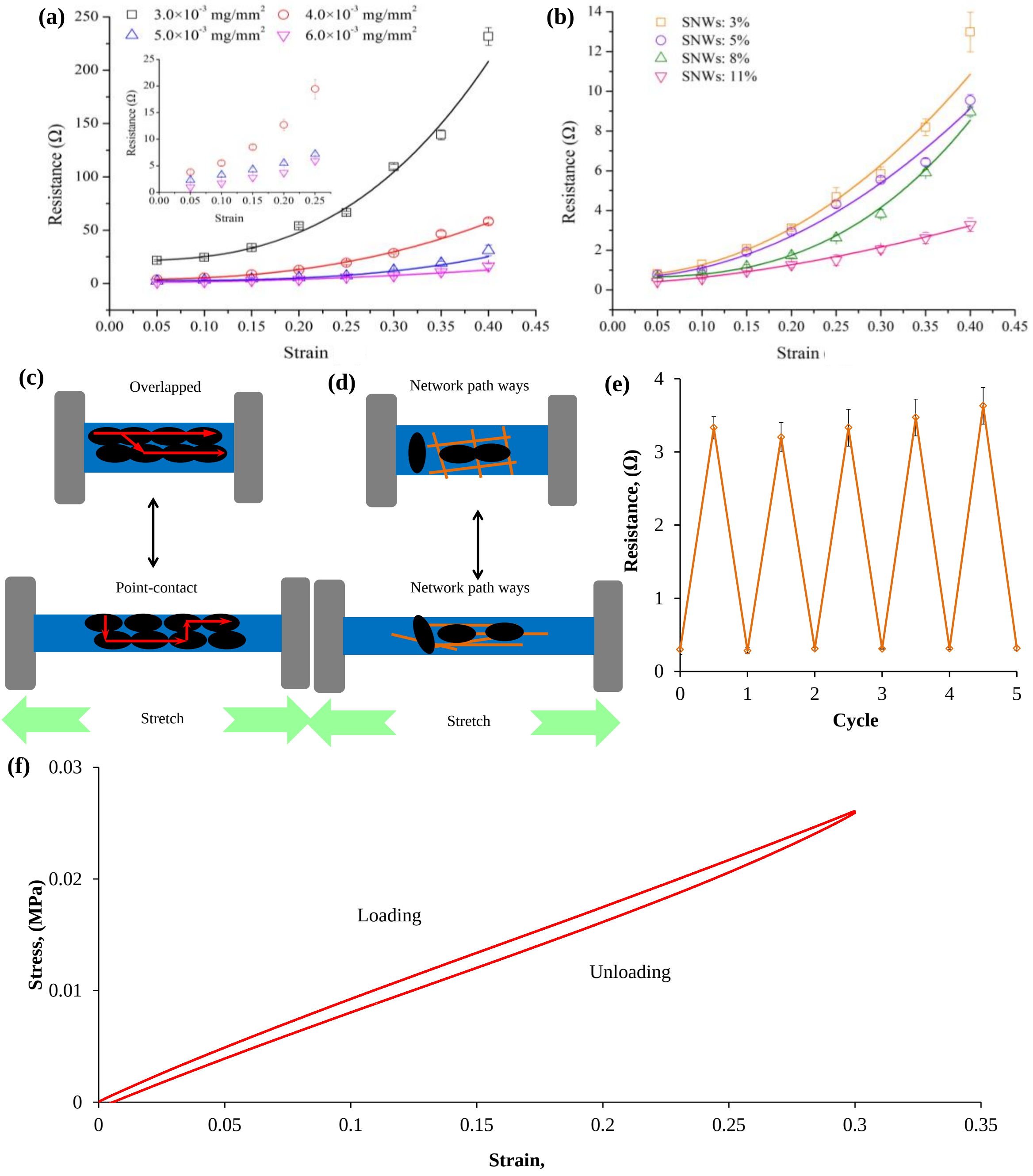

Figure 6.10. The effect of strain on the electrical resistance of (a) Ag flakes (SFs) embedded oleophobic microstructured surface with varied surface coverage, and (b) Ag flake/nanowires (SFs/SNWs) embedded oleophobic microstructured surface of a constant surface coverage of 6.0×10^{-2} mg/mm^2 with varied SFs/SNWs ratios; (c) and (d) are the schematic illustration of the effect of strain on conductive pathways of (a) and (b) ; (e) the cyclic stretching tests on SFs/SNWs embedded FDTS-blended microstructured surfaces. In (a) and (b) each data points were repeated three times on three separated samples and the error bars were the standard deviation. At the low strains, the error bars were too small to be shown. (f) the stress vs. strain curves of SFs/SNWs embedded micro-structures. There is little hysteresis during the loading-unloading stretching tests.

Oleophobicity is an important issue, closely related to the surface cleaning, antisticky, and anticorrosion properties desired for the protection of the surface from contamination and prolonging the service life of the material. In this section, we examined the effect of adding conductive fillers on surface oleophobicity. The oleophobicity of SFs and SFs/SNWs embedded FDTS-blended PDMS microstructured surface was characterized using oil contact angles (Figure 6.11). Results showed that the prepared samples are highly oleophobic; the contact angles for both formamide and glycerol were larger than 120°. In terms of glycerol, the largest contact angle was 150° at the lowest SFs surface coverage of 3.0×10^{-2} mg/mm^2 (Figure 6.11a). A slight decrease of glycerol contact angle was observed with increasing the SFs surface coverage (Figure 6.11a). At the highest surface coverage (6.0×10^{-2} mg/mm^2) glycerol contact angle was 146° which was only 4° smaller than the largest contact angle. This result indicated a negligible effect of SFs surface coverage on the oleophobicity. The same trend was found for the contact angles of formamide on SFs embedded microstructure surfaces. Note that the contact angles of formamide were slightly smaller than glycerol contact angles, since the surface tension of formamide is smaller than glycerol. The effect of adding SNWs on the oil contact angles of the microstructured surfaces is shown in Figure 6.11b. It is interesting to note that the oil contact angles first increased and then dropped. At the starting point with only 2% of SNWs, the contact angles of glycerol and formamide were 137° and 126°, respectively. When the fraction of SNWs was increased to 5%, the oil contact angle increased to 144° (glycerol) and 136° (formamide). Likely the smallness of SNWs made the Ag flake coating layer less dense (more PDMS surface would be exposed), resulting in an enhanced oleophobicity or larger oil contact angles. However, continuing to increase the fraction of SNWs would cause the surface to be highly covered by the conductive fillers (both SFs and SNWs); it became difficult for the PDMS resin to penetrate through the thicker SFs/SNWs layer, resulting in smaller oil contact angles. Overall, the influence of adding Ag nanoparticles on the oleophobicity of microstructured surface is minimal in comparison to its dramatic influence of the surface conductivity.

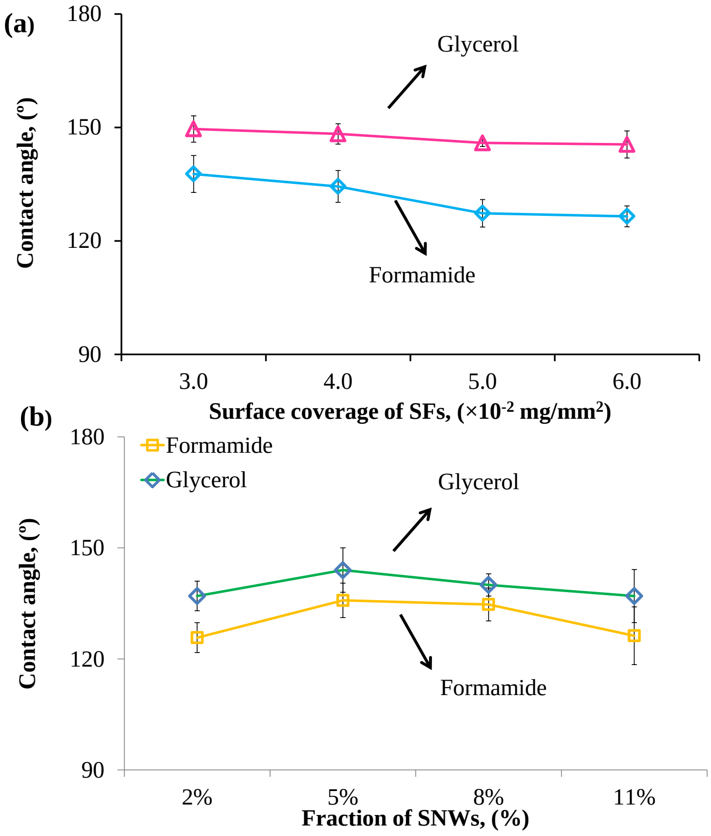

Figure 6.11. (a) The effect of Ag flakes (SFs) surface coverage on the oil contact angles of microstructured surfaces, (b) the effect of the fraction of nanowires (SNWs) on the oil contact angles with a constant surface coverage of Ag flakes and SNWs of 6.0 × 10^{-2} mg/mm^{2} with varied SFs/SNWs ratios.

After we have studied the effects of surface coverage of SFs on conductivity, stretchability and oleophobicity, the as-prepared samples were used to reduce frozen oil adhesion by applying DC current. As shown in Figure 6.12, the knock-off force increased with the increase of SFs surface coverage. At the lowest SFs surface coverage, the resistance was measured of 18 Ω and the obtained knock-off of the oil droplet was 0.33 N after applied 1 A DC current for 2 mins. The knock-off force increased to 0.63 N, when the surface resistance decreased to 1 Ω. This is because with the decreasing of surface resistance, the generated of thermal heat becomes less. As a result it requires larger force to knock of the frozen oil droplet. In the other hand, larger surface coverage of SFs caused the decrease of oleophobicity, thereby at the large surface coverage the knock-off force increased. As a consequence, with the decreasing of resistance and oleophobicity, the knock-off force becomes larger due to the less generated thermal heat. This conclusion matches well with the work in previous chapter.

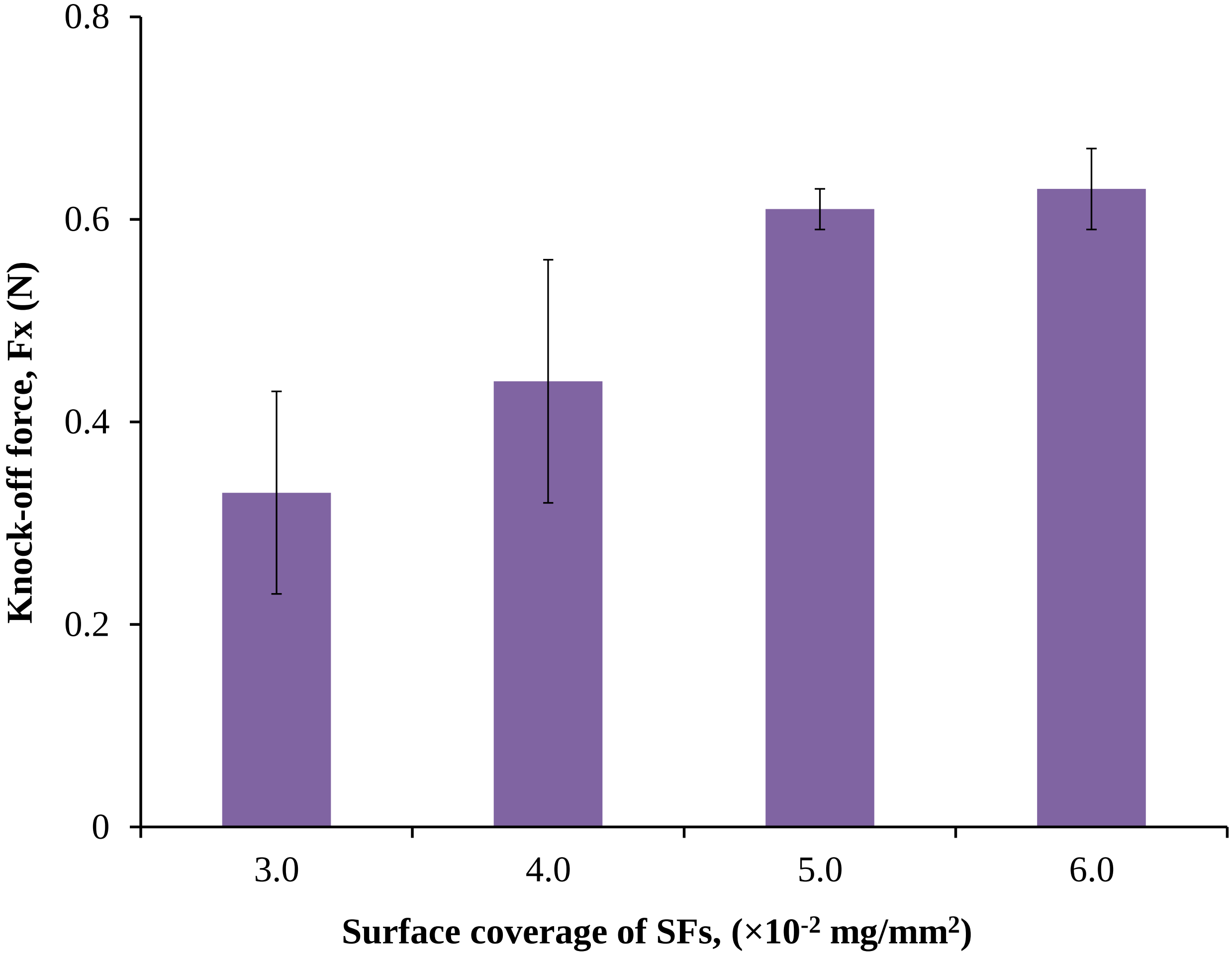

Figure 6.12. The effects of surface coverage of SFs on frozen oil adhesion reduction after applying 1 A DC current for 2 mins.

6.4 Conclusions

In summary, durable, stretchable, electrically conductive, and superoleophobic hierarchical microstructures have been successfully developed by embedding silver fillers into FDTS-blended PDMS surface during the pattern transfer process. Results showed that highly conductive surface was obtained at a relatively low surface coverage of conductive fillers; the conductive percolation of SFs inlaid surfaces was 3.0×10^{-2} mg/mm^2. Conductivity was enhanced by using SNWs to replace some SFs. The SNWs formed conductive networks more effectively than the overlapped structure formed by pure SFs. Sliding tests demonstrated that these conductive fillers had strongly bonded into FDTS-blended PDMS microstructure and were stable at the sliding preload of 8.0 N. The applied strain on SFs embedded samples caused the poor connection of SFs leading to the increase of resistance, while the high aspect ratio SNWs retained the good connections resulting in only a slight increase of resistance. Furthermore, the conductive microstructured surfaces are highly stable after cycled stretch tests. FDTS migrated to the surface to reduce the surface energy, contributing to the observed superoleophobicity. Frozen oil adhesion reduction tests were performed on SFs embedded PDMS microstructured surfaces by applying DC current indicating the decreasing of resistance leading to the large adhesion force. The integrated multifunctional properties could be helpful for the development of multifunctional smart conductive devices and can be used to reduce frozen oil adhesion.

Chapter 7. Conclusions and Future Work

7.1 Summary of Contributions and Concluding Remarks

The objectives of this research thesis were to develop multifunctional superhydro-oleophoobic microstructures and investigating their surface properties on frozen oil adhesion reduction. To achieve these objectives, we first developed a high efficient method for robust bio-inspired superhydro-oleophobic microstructure fabrication through blending fluoropolymer into polymer elastomer and using a pattern transfer approach which addressed the problems in other common approaches. Thereafter, surface chemistry and structure effects on frozen oil adhesion reduction were studied comprehensively on micro-structured surfaces with varying oleophobicity. Two different superoleophobic-conductive micro-structured surfaces were constructed and the effects of conductive fillers on oleophobicity, conductivity and frozen oil adhesion reduction were explored. The concluding remarks of this research project were demonstrated in four sections:

(1) Fundamental Study of Superhydro-oleophobic Microstructures Development

Two different approaches (vapor deposition coating FDTS and blending FDTS into PDMS) were compared in superhydro-oleophobic micropillar fabrication in terms of surface morphology, surface energy, water and oils contact angles and surface chemistry composition. Although these two methods resulted in the surfaces becoming enriched with FDTS with similar surface composition and surface energy, the vapor deposition caused a rough surface with defects, while blending FDTS into PDMS maintained a smooth surface. Experimental and theoretical results of water and oils contact angles showed that FDTS blending into PDMS was much more efficient than vapor deposition approach on fabrication superhyro-oleophobic micropillars. Furthermore, the increased content of FDTS in PDMS did not significantly enhance olephobicity due to FDTS aggregation. However, one prerequisite for the blending method to be effective is that there is no chemical reaction between FDTS and the polymer resin.

(2) The Effects of Surface Chemistry and Structure on Frozen Oil Adhesion Reduction

After we have established using the FDTS blended PDMS composite system to fabricate superoleophobic structures *via* pattern transfer approach, further investigations on the effects of surface chemistry and structure on frozen oil adhesion reduction were carried out on flat/micropillared surfaces with varied oleophobicity. Knock-off tests were performed on a variety of surfaces ranging from oleophilic to superoleophobic to obtain the relation between oleophobicity and frozen oil adhesion. The result correlated well with the calculated results from the Dupre-Yong equation, showing that the frozen oil adhesion was reduced significantly when the surface was superoleophobic. The relationship between oleophobicity and frozen oil adhesion has been investigated for the first time, showing an overall trend of higher oleophobicity causing reduced adhesion strength of frozen oil, suggesting a possible synergetic effect of utilizing FDTS chemistry and micropillars to reduce the frozen oil adhesion strength.

(3) Investigation of Oleophobicity and Resistance on Frozen Oil Adhesion Reduction

Although the relation between surface chemistry, structure and frozen oil adhesion was studied through the previous sections, there is a need of an active approach to reduce frozen oil adhesion or frozen oil de-melting in high efficiency. Borrowing the ideas from de-icing, Joule heating generated by DC current could be utilized. With this in mind, we developed a new method to fabricate superoleophobic irregular microstructures with electrical conductivity. Superoleophobic-conductive micropillars were fabricated via a two steps pattern transfer approach by using Ag flakes/epoxy composites. Both the static and dynamic contact angles on composite micropillars with varied Ag flakes ratios were measured to evaluate the self-cleaning and surface adhesion properties. The Ag flakes ratio in epoxy had a significant effect on oleophobicity while the resistance decreased dramatically with increasing Ag flakes. DC current induced melting is “bottom-top” melting, and the solid-solid contact transferred into solid-liquid immediately reducing the frozen oil adhesion. The larger the resistance and oleophobicity, the better it reduced the frozen oil adhesion.

(4) Durable Electrically Conductive and Superoleophobic Microsurfaces Development

Though blending a certain amount Ag flakes in epoxy can change the surface from insulating to conductive, the large amount of conductive fillers would cause a rapid increase in cost and sacrifice the mechanical properties, and also make it hard to adjust the conductivity. To solve this problem, Ag flakes and Ag flakes/ Ag nanowires were embedded into the surface of the FDTS blended PDMS microstructure. With the increasing amount of these embedded conductive fillers, the conductivity increased rapidly while the oleophoobicity decreased gradually reaching at a flat stage with oil contact angles around 130º. The durability of these conductive fillers with substrate was evaluated by scratch tests, showing a robust bonding. Furthermore the relation of stretchability and reversibility were characterized showing that the Ag flakes/ Ag nanowires embedded microsurface has better mechanical and electrical performances.

7.1.1 List of Peer-reviewed Journal Publications

- **Zihe Pan**, Tianchang Wang, Shaofan Sun, Boxin Zhao. Durable Micro-structured Surfaces: Combining Electrical Conductivity with Superoleophobicity. *ACS Applied Materials & Interfaces* **2016**, *8*, 1795−1804.
- **Zihe Pan**, Wei Zhang, Andrew Kowalski, Boxin Zhao. Oleophobicity of Biomimetic Micro-patterned Surfaces and Its Effect on the Adhesion of Frozen oil. *Langmuir*, **2015**, *31*, 9109-9110.
- **Zihe Pan**, Hamed Shahsavan, Wei Zhang, Fut K Yang, Boxin Zhao. Superhydro-oleophobic Bio-inspired Polydimethylsiloxane Micropillared Surface via FDTS Coating/Blending Approaches. *Applied Surface Science*, **2015**, *324*, 612-620.
- **Zihe Pan**, Tianchang Wang, Yikang Zhou, Boxin Zhao. Development of Electrically Conductive–Superoleophobic Micropillars for Reducing Surface Adhesion of Oil at Low Temperatures. *Applied Surface Science*, **2016**, *389*, 623-631.
- Wei Zhang, **Zihe Pan**, Fut K Yang, Boxin Zhao. A Facile In-Situ Approach to Polypyrrole Functionalization through Bio-Inspired Catechols. *Advanced Functional Materials*, **2015**, *25*, 1588-1597.
- Shaofan Sun, **Zihe Pan**, Fut K Yang, Yudong Huang, Boxin Zhao. A transparent silica colloidal crystal/PDMS composite and its application for crack suppression of metallic coatings. *Journal of Colloid and Interface Science*, **2016**, *46*, 136-143.
- Shaofan Sun, **Zihe Pan**, Wei Zhang, Fut K Yang, Yudong Huang, Boxin Zhao. Acid treatment of silver flake coatings and its application in the flexible electrical circuits. *Journal of Material Science: Materials in Electronics*. **2016**, *27*, 4363-4371.
- Wei Zhang, Fut Kuo Yang, **Zihe Pan**, Jian Zhang, Boxin Zhao. Bio-inspired Dopamine

Functionalization of Polypyrrole for Improved Adhesion and Conductivity. *Macromolecular Rapid Communication*, **2014**, *35*, 350-354.

7.2 Future Work

This research work has demonstrated using FDTS blended PDMS polymer composite and the pattern transfer approach to fabricate multifunctional superoloephobic microstructures. Their surface chemistry and structure effects on frozen oil adhesion reduction were comprehensively studied. However, there are still additional questions that need to be explored in future study, which could promote the understanding of frozen oil adhesion reduction.

(1). In Chapter 2, we demonstrated that FDTS was blended into PDMS as a surface tension reduction agent to reduce the surface energy of the composite system. Although FDTS was found to migrate to the surface of PDMS, the aggregation and distribution of FDTS at the interface and the effects on other properties such as viscosity, transparency should be explored to help understand the role of FDTS in PDMS. In order to figure out these problems AFM, FTIR, UV-Vis, etc. are suggested to be used to comprehensively study the aggregation and migration behaviors of FDTS in PDMS and the effects on surface morphology.

(2). Surface chemistry and structure are regarded as two of the most crucial factors in developing superoleophobic surfaces and their synergetic effects on frozen oil adhesion reduction were studied in Chapter 3 showing the important function of micropillars. As numerous works published on anti-icing indicate that anti-icing can be achieved by ice-delay and ice adhesion reduction, the hierarchical structures were regarded as the most effective approach. Inspired by the work of anti-ice, the fabrication of hierarchal superoleophobic nano/microstructures shows its necessity in delaying the oil freezing and reduces the frozen oil adhesion. The mechanism of using hierarchical nano/microstructure to delay oil freezing should be investigated.

(3). Although we have developed electrically conductive and superoleophobic micropillars and studied the effects of conductive resistance and oleophobicity on frozen oil adhesion reduction and de-icing of frozen oil, more works are still needed such as thermal dissipation in the frozen oil. The generated Joule heating from the electrically conductive and superoleophobic surfaces from the applied DC current was used to melt the frozen oil and its dissipation with circumstance, sample its self, frozen oil, and the cooling chamber should be well known during the melting process. Once the thermal dissipation is established, the de-freezing process can be effectively controlled. Thus, both simulations and experiments are recommended to precisely control the de-freezing process. Furthermore, the temperature effect on polymer structures should be considered because most polymers are not thermally stable and can be destroyed at high temperature. As a consequence, the resistance of the sample should be well controlled to adjust the generated Joule heating.

(4). To reduce the usage of conductive fillers, maintain the properties of polymer matrix and ease the adjustment of material properties, a thin layer of conductive fillers were embedded into the FDTS blended PDMS microstructure surface in the pattern transfer process. With this method, a flexible, electrically conductive, superolephobic microstructure was developed by using very small amount of conductive fillers. This sort of material fits our research purpose and also is of great importance for solving the potential problems of dusty/oily species contamination, poor chemical stability etc. in many applications such as artificial skin and transparent battery electrodes. Our preliminary results showed that the fabricated material was conductive with superoleophobicity but not transparent. Thus for the future work on this field, it is important to develop flexible, electrically conductive, superoleophobic and transparent material to broaden its applications in biomimetics, self-cleaning, battery electrodes etc.

References

(1). Sun, T.; Feng, L.; Gao, X.; Jiang, L. Bioinspired Surfaces with Special Wettability. *Acc. Chem. Res.* **2005**, *38*, 644–652.

(2). Dorrer, C.; Rühe, J. Some Thoughts on Superhydrophobic Wetting. *Soft Matter* **2009**, *5*, 51–61.

(3). Xue, Z.; Liu, M.; Jiang, L. Recent Developments in Polymeric Superoleophobic Surfaces. *J. Polym. Sci. Pol. Phys*. **2012**, *50*, 1209–1224.

(4). Nishimoto, S.; Bhushan, B. Bioinspired Self–cleaning Surfaces with Superhydrophobicity, Superoleophobicity, and Superhydrophilicity. *RSC Adv*. **2013**, *3*, 671.

(5). Nakajima, A.; Hashimoto, K.; Watanabe, T. Recent Studies on Super–Hydrophobic Films. *Monatshefte fÜr Chemie*, **2001**, *132*, 31–41.

(6). Quéré, D. Wetting and Roughness. *Annu. Rev. Mater. Res.* **2008**, *38*, 71–99.

(7). Liu, K.; Jiang, L. Bio–inspired Self–cleaning Surfaces. *Annu. Rev. Mater. Res.* **2012**, *42*, 231–263.

(8). Jung, Y. C.; Bhushan, B. Wetting Behavior of Water and Oil Droplets in Three–phase Interfaces for Hydrophobicity–philicity and Oleophobicity–philicity, *Langmuir* **2009**, *25*, 14165–14173.

(9). Liu, K.; Yao, X.; Jiang, L. Recent Developments in Bio–inspired Special Wettability. *Chem. Soc. Rev*. **2010**, *39*, 3240–32455.

(10). Ma, M.; Hill, R. M. Superhydrophobic Surfaces. *Curr. Opin. Colloid Interface Sci*. **2006**, *11*, 193–202.

(11). Wenzel, N. R. Resistance of Solid Surfaces to Wetting by Water. *Ind. Eng. Chem.* **1936**, *28*, 988–994.

(12). Cassie, A. B. D.; Baxter, S. Wettability of Porous Surfaces. *Trans. Faraday Soc.* **1944**, *40*, 546–551.

(13). Feng, L.; Song, Y.; Zhai, J.; Liu, B.; Xu, J.; Jiang, L.; Zhu B. Creation of a Superhydrophobic Surface from an Amphiphilic Polymer. *Angew. Chem.* **2003**, *115*, 824–826.

(14). Jin, H.; Feng, X.; Feng, L.; Sun, T.; Zhai, J.; Lin, T.; Jiang, L. Superhydrophobic Aligned Polystyrene Nanotube Films with High Adhesive Force. *Adv. Mat.* **2005**, *17*, 1977–1981.

(15). Jafari, R.; Menini, R.; Farzaneh, M.; Superhydrophobic and Icephobic Surfaces Prepared by RF–sputtered Polytetrafluoroethylene Coatings. *Appl. Surf. Sci.* **2010**, *257*, 1540–1543.

(16). Momen, G.; Farzaneh, M.; Facile Approach in the Development of Icephobic Hierarchically Textured Coatings as Corrosion Barrier. *Appl. Surf. Sci.* **2014**, *299*, 41–46.

(17). Cao, L.; Price, T. P.; Weiss, M.; Gao, D.; Super Water– and Oil–Repellent Surfaces on Intrinsically Hydrophilic and Oleophilic Porous Silicon Films. *Langmuir* **2008**, *24*, 1640–1643.

(18). Carlborg, C. F.; van der Wijingaart, W. Sustained Superhydrophobic Friction Reduction at High Liquid Pressures and Large Flows. *Langmuir* **2010**, *27*, 487–493.

(19). Jiang, T.; Guo, Z.; Liu, W. Biomimetic superoleophobic surfaces: focusing on their fabrication and applications *J. Mater. Chem. A*, **2015**, *3*, 1811–1827.

(20). Tuteja, A.; Choi, W.; Ma, M.; Mabry, J. M.; Mazzella, S. A.; Rutledge, G. C.; McKinley, G. H.; Cohen, R. E. Designing Superoleophobic Surfaces. *Science* **2007**, *318*, 1618–1622.

(21). Zhao, H.; Law, K. Y.; Sambhy, V.; Fabrication, Surface Properties, and Origin of Superoleophobicity for a Model Textured Surface. *Langmuir* **2011**, *27*, 5927–5935.

(22). Kang, S. M.; Kim, S. M. Kim, H. N.; Kwak, M. K.; Tahk, D. H.; Suh, K. Y. Robust superomniphobic surfaces with mushroom–like micropillar arrays. *Soft Matter*. **2012**, *8*, 8563–8568.

(23). Darmanin, T.; Guittard, F.; Amigoni, S.; de Givenchy, E. T.; Noblin, X.; Kofman, R.; Celestini, F.; Superoleophobic behavior of fluorinated conductive polymer films combining electropolymerization and lithography. *Soft Matter* **2011**, *7*, 1053–1057.

(24). Wang, D.; Wang, X.; Liu, X.; Zhou, F. Engineering a Titanium Surface with Controllable Oleophobicity and Switchable Oil Adhesion. *J. Phys. Chem. C* **2010**, *114*, 9938–9944.

(25). Tsujii, K.; Yamamoto, T.; Onda, T.; Shibuichi S. Super Oil–repellent Surfaces. *Angew. Chem. Int. Ed. Engl.* **1997**, *36*, 1011–1012.

(26). Hoefnagels, H. F.; Wu, D.; de With, G.; Ming, W. Biomimetic Superhydrophobic and Highly Oleophobic Cotton Textiles. *Langmuir* **2007**, *23*, 13158–13163.

(27). Liu, Y.; Xiu, L.; Hess, D. W.; Wong, C. P. Silicon surface structure–controlled oleophobicity. *Langmuir*, **2010**, *26*, 8908–8913.

(28). Coffinier, Y.; Galopin, E.; Szunerits, S.; Boukherroub, R. Preparation of Superhydrophobic and Oleophobic Diamond Nanograss Array. *J. Mater. Chem.* **2010**, *20*, 10671–10675.

(29). Wu, W.; Wang, X.; Wang, D.; Chen, M.; Zhou, F.; Liu, W.; Xue, Q. Alumina Nanowire Forests *via* Unconventional Anodization and Super–repellency Plus Low Adhesion to Diverse Liquids. *Chem. Commun*. **2009**, *7*, 1043–1045.

(30). Choi, W.; Tuteja, A.; Chhatre, S.; Mabry, J. M.; Cohen, R. E.; McKinley, G. H. Fabrics with Tunable Oleophobicity. *Adv. Mater.* **2009**, *21*, 2190–2195.

(31). Zimmermann, J.; Rabe, M.; Artus, G. R. J.; Seeger, S. Patterned Superfunctional Surfaces Based on a Silicone Nanofilament Coating. *Soft Matter* **2008**, *4*, 450–452.

(32). Cao, L.; Gao, D. Transparent Superhydrophobic and Highly Oleophobic Coatings. *Faraday Discussions*. **2010**, *146*, 57–65.

(33). Steel, A.; Bayer, I.; Loth, E. Inherently Superoleophobic Nanocomposite Coatings by Spray Atomization. *Nano Letter* **2009**, *9*, 501–505.

(34). Im, M.; Im, H.; Lee, J. H.; Yoon, J. B.; Choi, Y. K. A Robust Superhydrophobic and Superoleophobic Surface with Inverse–trapezoidal Microstructures on a Large Transparent Flexible Substrate. Soft Matter **2010**, *6*, 1401–1404.

(35). Bunker, B. C.; Carpick, R. W.; Assink, R. A.; Thomas, M. L.; Hankins, M.G.; Voigt, J. A.; Sipola, D.; de Boer, M. P.; Gulley, G. L. The Impact of Solution Agglomeration on the Deposition of Self–assembled Monolayer. *Langmuir* **2000**, *16*, 7742–7751.

(36). Frtitz, J. L.; Owen, M. J. Hydrophobic Recovery of Plasma–treated Polydimethylsiloxane. *J. Adhesion* **1995**, *54*, 33–45.

(37). Bodas, D.; Khan–Malek, C. Formation of More Stable Hydrophilic Surfaces of PDMS by Plasma and Chemical Treatments. *Microelectron. Eng*. **2006**, *83*, 1277–1279.

(38). Hong, S. M.; Kim, S. H.; Kim, J. H.; Hwang, H. I. Hydrophilic surface modification of PDMS using atmospheric RF plasma. *J. Phys.: Conf. Ser*. **2006**, *34*, 656–661.

(39). Karatum, O.; Steiner III, S. A.; Griffin, J. S.; Shi, W.; Plata, D. L. Flexible, Mechanically Durable Aerogel Composites for Oil Capture and Recovery. *ACS Appl. Mater. Interfaces* **2016**, *8*, 215−224.

(40). Xia, F.; Jiang, L. Bio–Inspired, Smart, Multiscale Interfacial Materials. *Adv. Mater.* **2008**, *20*, 2842–2858.

(41). Huang, Y.; Liu, M.; Wang, J.; Zhou, J.; Wang, L.; Song, Y.; Jiang, L. Controllable Underwater Oil–Adhesion–Interface Films Assembled from Nonspherical Particles. *Adv. Funct. Mater.* **2011**, *21*, 4436–4441.

(42). Wu, D.; Wu, S.; Chen, Q. D.; Zhao, S.; Zhang, H.; Jiao, J.; Pirsol, J. A.; Wung, J.; Sun, H.; Jiang, L. Facile Creation of Hierarchical PDMS Microstructures with Extreme Underwater Superoleophobicity for Anti–oil Application in Microfluidic Channels. *Lab Chip*, **2011**, *11*, 3873–3879.

(43). Fogliaa,T. A.; Nelsona, L. A.; Dunnb, R. O.; Marmer W. N. Low–Temperature Properties of Alkyl Esters of Tallow and Grease. *JAOCS* **1997**, *74*,951–955.

(44). Jayadas, N. H.; Nair, K. P. Coconut Oil as Base Oil for Industrial Lubricants—Evaluation and Modification of Thermal, Oxidative and Low Temperature Properties. *Tribol. Int.* **2006**, *39*, 873–878.

(45). Prowse,T. D.; Furgal, C.; Chouinard, R.; Melling, H.; Milburn, D.; Smith S. L. Implications of Climate Change for Economic Development in Northern Canada: Energy, Resource, and Transportation Sectors. *Ambio* **2009**, *38*, 272–281.

(46). Martínez–Palou, R.; Mosqueira, M. d. L.; Zapata–Rendón, B.; Mar–Juárez, E.; Bernal–Huicochea, C.; de la Cruz Clavel–López, J.; Aburto, J. Transportation of Heavy and Extra–heavy Crude Oil by Pipeline: A Review. *J. Petrol. Sci. Eng.* **2011**, *75*, 274–282.

(47). Buckley, J.S.; Liu, Y. Some Mechanisms of Crude Oil–brine–solid Interactions. *J. Petrol. Sci. Eng.* **1998**, *20*. 155–160.

(48). Meuler, A. J.; Smith, J. D.; Varanasi, K. K.; Mabry, J. M.; McKinley, G. H.; Cohen, R. E. Relationships Between Water Wettability and Ice Adhesion. *ACS Appl. Mater. Interfaces.* **2010**, *2*, 3100–3110.

(49). Guo, P.; Zheng, Y.; Wen, M.; Song, C.; Lin, Y.; Jiang, L. Icephobic/Anti–icing Properties of Micro/nanostructured Surfaces. *Adv. Mater.* **2012**, *24*, 2642–2648.

(50). Guo, P.; Wen, M.; Wang, L.; Zheng, Y.; Strong Anti–ice Ability of Nanohair Over Micro–ratchet Structuring. *Nanoscale*, **2014**, *6*, 3917–3920.

(51). Chanda, J.; Ionov, L.; Kirillova, A.; Synytsk, A. New Insight into Icing and De–icing Properties of Hydrophobic and Hydrophilic Structured Surfaces Based on Core–shell Particles. *Soft Matter* **2015**, *11*, 9126–9134.

(52). Laforte, J.L.; Allaire, M.A.; Laflamme, J. State–of–the–art on Power Line De–icing. *Atmos. Res.* **1998**, *46*, 143–158.

(53). Parent, O.; Ilinca, A. Anti–icing and De–icing Techniques for Wind Turbines: Critical Review. *Cold Reg. Sci. Technol*. **2011**, *65*, 88–96.

(54). Wang, L.; Wen, M.; Zhang, M.; Jiang, L.; Zheng, Y. Ice–phobic Gummed Tape with Nano–cones on Microspheres. *J. Mater. Chem. A* **2014**, *2*, 3312–3316.

(55). Wang, Y.; Xue, J.; Wang, Q.; Chen, Q.; Ding, J. Verification of Icephobic/anti–icing Properties of a Superhydrophobic Surface. *ACS Appl. Mater. Interfaces* **2013**, *5*, 3370–3381.

(56). Chen, J.; Luo, Z.; Fan, Q.; Lv, J.; Wang, J. Anti–ice Coating Inspired by Ice Skating. *Small* **2014**, *10*, 4693–4699.

(57). Davis, A.; Yeong, Y. H.; Steele, A.; Bayer, I. S.; Loth, E. Superhydrophobic Nanocomposite Surface Topography and Ice Adhesion. *ACS Appl. Mater. Interfaces* **2014**, *6*, 9272–9279.

(58). Jiang, X.; Fan, S.; Zhang, Z.; Sun, C.; Shu, L. Simulation and Experimental Investigation of DC Ice–melting Process on an Iced Conductor. *IEEE Trans. Power Delivery* **2010**, *25*, 919–929.

(59). Personne, P.; Gayet, Y.F. Ice Accretion on Wires and Anti–icing Induced by Joule Effect. *J. Appl. Meteorol*. **1988**, *27*, 101–114.

(60). Petrenko, V.F.; Sullivan, C.R.; Kozlyuk, V. Variable–resistance Conductors (VRC) for Power–line De–icing. *Cold Reg. Sci. Technol.* **2011**, *65*, 23–28.

(61). Lee, B. Y.; Heo, K.; Bak, J. H.; Cho, S. U.; Moon, S.; Park, Y. D.; Hong, S. Scalable Assembly Method of Vertically–Suspended and Stretched Carbon Nanotube Network Devices for Nanoscale Electro–Mechanical Sensing Components. *Nano Lett.* **2008**, *8*, 4483–4487.

(62). Herrmann, S.; Ritchie, C.; Streb, C. Polyoxometalate–Conductive Polymer Composites for Energy Conversion, Energy Storage and Nanostructured Sensors. *Dalton Trans.* **2015,** *44*, 7092–7104.

(63). Yan, D. X.; Pang, H.; Li, B.; Vajtai, R.; Xu, L.; Ren, P. G.; Wang, J. H.; Li, Z. M. Structured Reduced Graphene Oxide/Polymer Composites for Ultra–Efficient Electromagnetic Interference Shielding. *Adv. Funct. Mater.* **2015,** *25*, 559–566.

(64). Chen, Z.; Ren, W.; Gao, L.; Liu, B.; Pei, S.; Cheng, H. M. Three–Dimensional Flexible and Conductive Interconnected Graphene Networks Grown by Chemical Vapour Deposition. *Nat. Mater*. **2011**, *10*, 424–428.

(65). Gray, D. S.; Tien, J.; Chen, C. S. Conductivity Elastomeric Electronics. *Adv. Mater.* **2004**, *16*, 393–397.

(66). Khosla, A.; Gray, B. L. Preparation, Characterization and Micromolding of Multi–walled Carbon Nanotube Polydimethylsiloxane Conducting Nanocomposite Polymer. *Mater. Lett.* **2009**, *63*, 1203–1206.

(67). Ho, Y. H.; Chen, K. Y.; Liu, S. W.; Chang, Y. T.; Huang, D. W.; Wei, P. K. Transparent and Conductive Metallic Electrodes Fabricated by Using Nanosphere Lithography. *Org. Electron.* **2011,** *12*, 961–965.

(68). Song, L.; Myers, A. C.; Adams, J. J.; Zhu, Y. Stretchable and Reversibly Deformable Radio Frequency Antennas Based on Silver Nanowires. *ACS Appl. Mater.Interfaces* **2014,** *6*, 4248–4253.

(69). Rogers, J. A.; Someya, T.; Huang, Y. Materials and Mechanics for Stretchable Electronics. *Science* **2010**, *327*, 1603–1607.

(70). Jiang, T.; Huang, R.; Zhu, Y. Interfacial Sliding and Buckling of Monolayer Graphene on a Stretchable Substrate. *Adv. Funct. Mater.* **2014**, *21*, 396–402.

(71). Zhang, R.; Baxendale, M.; Peijs, T. Universal Resistivity–Strain Dependence of Carbon Nanotube/Polymer Composites. *Phys. Rev. B* **2007**, *76*, 195433.

(72). Jiang, Y.; Xi, J.; Wu, Z.; Dong, H.; Zhao, Z.; Jiao, B.; Hou, X. Highly Transparent, Conductive, Flexible Resin Films Embedded with Silver Nanowires. *Langmuir* **2015**, *31*, 4950–4957.

(73). Veleva, L.; Valdez, B.; Lopez, G.; Vargas, L.; Flores, J. Atmospheric Corrosion of Electro–Electronics Metals in Urban Desert Simulated Indoor Environment. *Corros. Eng., Sci. Technol.* **2008**, *43*, 149–155.

(74). Siegel, A. C.; Bruzewicz, D. A.; Weibel, D. B.; Whitesides G. M. Microsolidics: Fabrication of Three–Dimentional Metallic Microstructures in Poly(dimethylsiloxane). *Adv. Mater*. **2007**, *19*, 727–733.

(75). Hidber, P. C.; Helbig, W.; Kim, E.; Whitesides, G. M. Microcontact Printing of Palladium Colloids: Micron–Scale Patterning by Electroless Deposition of Copper. *Langmuir* **1996,** *12*, 1375–1380.

(76). Won, Y.; Kim, A.; Yang, W; Joeng, S.; Moon, J. A Highly Stretchable, Helical Copper Nanowire Conductor Exhibiting a Stretchability of 700%. *NPG Asia Mater.* **2014**, *6*, doi:10.1038/am.2014.88.

(77). Lee, S.; Shin, S.; Lee, S.; Seo, J.; Lee, J.; Son, S.; Cho, H. J.; Algadi, H.; Al–Sayari, S.; Kim, D. E.; Lee, T. Ag Nanowire Reinforced Highly Stretchable Conductive Fibers for Wearable Electronics. *Adv. Funct. Mater.* **2015**, *25*, 3114–3121.

(78). Chen, L. F.; Huang, Z. H.; Liang, H. W.; Gao, H. L.; Yu, S. H. Three–Dimensional Heteroatom–Doped Carbon Nanofiber Networks Derived from Bacterial Cellulose for Supercapacitors. *Adv. Funct. Mater.* **2014**, *24*, 5104–5111.

(79). Sengupta, R.; Bhattacharya, M.; Bandyopadhyay, S.; Bhowmick, A. K. A Review on the Mechanical and Electrical Properties of Graphite and Modified Graphite Reinforced Polymer Composites. *Prog. Polym. Sci.* **2011**, *36*, 638–670.

(80). Jiang, H.; Moon, K.; Li, Y.; Wong, C. P. Surface Functionalized Silver Nanoparticles for Ultrahigh Conductive Polymer Composites. *Chem. Mater.* **2006**, *18*, 2969–2973.

(81). Pang, H.; Xu, L.; Yan, D. X.; Li, Z. M. Conductive Polymer Composites with Segregated Structures. *Prog. Polym. Sci.* **2014**, *39*, 1908–1933.

(82). Fassler, A.; Majidi, C. Liquid–Phase Metal Inclusions for a Conductive Polymer Composite. *Adv. Mater.* **2015**, *27*, 1928–1932.

(83). Ding, H.; Guo, y.; Leung, S. N. Development of Thermally Conductive Polymer Matrix Composites by Foaming–assisted Networking of Micron– and Submicron–scale Hexagonal Boron Nitride. *J. Appl. Polym. Sci.* **2016**, DOI: 10.1002/APP.42910.

(84). Rwei, S. P.; Ku, F. H.; Cheng, K. C. Dispersion of Carbon Black in a Continuous Phase: Electrical, Rheological, and Morphological Studies. *Colloid Polym. Sci.*, **2002**, *280*, 1110–1115.

(85). Bonn, D.; Eggers, J.; Indekeu, J.; Meunier, J.; Rolley, E. Wetting and Spreading. *Rev. Mod. Phy*. **2009**, *81*, 739–805.

(86). Chen, D.; Tan, L.; Liu, H.; Tang, F.; Hu, J.; Li, Y. Fabrication of Fast–Absorbing and Quick–Drying Wool Fabrics with Good Washing Durability. *ChemSusChem*. **2010**, *3*, 1031–1035.

(87). Wong, J. X. H.; Yu, H. Z. Preparation of Transparent Superhydrophobic Glass Slides: Demonstration of Surface Chemistry Characteristics. *J. Chem. Educ*. **2013**, *90*, 1203−1206.

(88). Huh, C.; Mason, S. G. Effects of Surface Roughness on Wetting (theoretical). *J. Colloid Interface Sci.* **1977**, *60*, 11–38.

(89). Gao, L.; Macarthy, T. J. The "Lotus Effect" Explained: Two Reasons Why Two Length Scales of Topography Are Important. *Langmuir*. **2006**, 22, 2966–2967.

(90). Marmur, A. Contact Angle Hysteresis on Heterogeneous Smooth Surfaces. *J. Colloid. Interface. Sci.* **1996**, 168, 40–46.

(91). de Gennes, P. G. Granular Matter: A Tentative View. *Rev. Mod. Phys. Sci.* **1985**, 57, 827–863.

(92). Bhushan, B. Bioinspired Structured Surfaces. *Langmuir*, **2012**, *28*, 1698–1714.

(93). Nosonovsky, M.; and Bhushan, B. Biomimetic Superhydrophobic Surfaces: Multiscale Approach. *Nano letter*, **2007**, *7*, 2633–2637.

(94). Liu, B.; Lange, F. F. Pressure Induced Transition Between Superhydrophobic States: Configuration Diagrams and Effect of Surface Feature Size. *J. Colloid, Interface. Sci*. **2006**, *298*, 899–909.

(95). Ran, C.; Ding, G.; Liu, W.; deng, Y.; and Hou, W. Wetting on Nanoporous Alumina Surface: Transition between Wenzel and Cassie States Controlled by Surface Structure. *Langmuir*, **2008**, *24*, 9952–9955.

(96). Lafuma, A.; Quere, D. Superhydrophobic States. *Nat. Mater.* **2003**, *2*, 457–460.

(97). Bartolo,D.; Bouamirrene, F.; Verneuil, E.; Buguin, A.; Silberzan, P.; Moulinet, S. Bouncing or Sticky Droplets: Impalement Transitions on Superhydrophobic Micropatterned Surfaces. *Euophys. Lett.* **2006**, *74*, 299–305.

(98). Koch, K.; Barthlott, W. *Philosophical transactions Series A, Mathematical, physical, and engineering sciences*. **2009**, *28*, 1487–509.

(99). Drelich, J.; Chibowski, E. Superhydrophilic and Superwetting Surfaces: Definition and Mechanisms of Control. *Langmuir*, **2010**, *21*, 18621–18623.

(100). Bauer, U.; Bohn, H. F.; Federle, W. Harmless nectar source or deadly trap: *Nepenthes* pitchers are activated by rain, condensation and nectar. *Proc. R. Soc. B,* **2008**, *275*, 259–265.

(101). Li, L.; Koshizaki, N. Vertically aligned and ordered hematite hierarchical columnar arrays for applications in field–emission, superhydrophilicity, and photocatalysis. *J. Matter.Chem*. **2010**, *20*, 2972–2978.

(102). Cebec, F. C.; Wu, Z.; Zhai, L; Cohen, R. E.; Rubner, M. F. Nanoporosity–Driven Superhydrophilicity: A Means to Create Multifunctional Antifogging Coatings. *Langmuir* **2006**, *22*, 2856–2862.

(103). Du, X.; He, J. Facile Fabrication of Hollow Mesoporous Silica Nanospheres for Superhydrophilic and Visible/Near–IR Antireflection Coatings. *Chem.–Eur. J.* **2011**, *17*, 8165–8174.

(104). Son, J.; Kundu, S.; Verma, L. K.; Sakhuja, M.; Danner, A. J.; Bhatia, C. S.; Yang, H. *Sol. Energ.Mat. Sol. C.* **2010**, *98*, 46–51.

(105). Kobayashi, M.; Terayama, Y.; Yamaguchi, H.; Terada, M.; Murakami, D.; Ishihara, K.; Takahara, A. Wettability and Antifouling Behavior on the Surfaces of Superhydrophilic Polymer Brushes. *Langmuir* **2012**, *28*, 7212–7222.

(106). Tijing, L. D.; Ruelo, M. T. G.; Amarjargal, A.; Pant, H. R.; Park, C. H.; Kim, D. W.; Kim, C. S.; Antibacterial and Superhydrophilic Electrospun Polyurethane Nanocomposite Fibers Containing Tourmaline Nanoparticles. *Chem. Eng. J.* **2012**, *197*, 41–48.

(107). Feng, L.; Li, S.; Li, Y.; Li, H.; Zhang, L.; Zhang, J.; Song, Y.; Liu, B.; Jiang , L.; Zhu, D. Super-hydrophobic Surfaces: From Natural to Artificial. *Adv. Mater*. **2002**, *14*, 1857–1860.

(108). Zheng, Y. M.; Gao, X. F.; Jiang, L. Directional adhesion of superhydrophobic butterfly wings. *Soft Matter*. **2007**, *3*, 178–182.

(109). Lee, W.; Jin, M. K.; Yoo, W. C.; and Lee, J. K. Nanostructuring of a polymeric substrate with well–defined nanometer–scale topography and tailored surface wettability. *Langmuir*. **2004**, *20*, 7665–7669.

(110). Jung, Y. C.; Buhsan, B. Biomimetic structures for fluid drag reduction in laminar and turbulent flows. *J. Phys.: Condens. Matter*. **2010**, *22*, 035104.

(111). Kreder1, M. J.; Alvarenga, J; Kim, P.; Aizenberg, J. Design of Anti–icing Surfaces: Smooth, Textured or Slippery? *Nature Review Mater.* **2016**, doi:10.1038/natrevmats.2015.3.

(112). Coulson, S. R.; Woodard, I.; Badyal, J. P. S.; Brewer, S. A.; Willis, C. Super–Repellent Composite Fluoropolymer Surfaces. *J.Phys. Chem. B.* **2000**, *104*, 8836–8840.

(113). Macdonald, B.; Shahsavan, H.; Zhao, B. Biomimetic micro–patterning of epoxy coatings for enhanced surface hydrophobicity and low friction. *Macromol.Mater. Eng.* **2014**, *299*, 237–247.

(114). He, Y.; Jiang. C.; Cao, X.; Chen, J.; Tian, W.; Yuan, W. Reducing Ice Adhesion by Hieriarchical Micro–nano–pillars. *Appl. Sur. Sci.* **2014**, *305*, 589–595.

(115). Bhushan, B.; Her, E. K. Fabrication of superhydrophobic surfaces with high and low adhesion inspired from rose petal. *Langmuir,* **2010**, *26*, 8207–8217.

(116). Ebert, D.; Bhushan, B. Wear–resistant Rose Petal–effect Surfaces with Superhydrophobicity and High Droplet Adhesion Using Hydrophobic and Hydrophilic Nanoparticles. *J. Colloid. Interface. Sci.* **2012**, 384, 182–188.

(117). Feng, L.; Zhang, Y.; Xi, J.; Zhu, Y; Wang, N.; Xia, F.; and Jiang, L. The Structural Color of Red Rose Petals and Their Duplicates. *Langmuir,* **2010**, 26, 14885–14889.

(118). Liu, K.; Tian, Y.; Jiang, L. Bio–inspired Superoleophobic and Smart Materials: Design, Fabrication, and Application. *Prog. Mater. Sci.* **2013**, *58*, 503–564.

(119). Fukada, K.; Nishizawa, S.; Shiratori, S. Antifouling property of highly oleophobic substrates for solar cell surfaces. *J. Appl. Phys.* **2014**, *115*, 103516 1–5.

(120). Marabotti, I.; Morelli, A.; Orsini, L. M.; Martinelli, E.; Galli, G.; Chiellini, E. Fluorinated/siloxane Copolymer Blends for Fouling Release: Chemical Characterisation and Biological Evaluation with Algae and Barnacles. *Biofouling,* **2009**, *25*, 481–493.

(121). Zhao, H.; Lan, K. Y. Super Toner and Ink Repellent Superoleophobic Surface. *ACS Appl. Mater. Interfaces.* **2012**, *4*, 4288–4295.

(122). Zhao, H.; Law, K. Y. Directional Self–Cleaning Superoleophobic Surface. *Langmuir.* **2012**, *28*, 11812–11818.

(123). Zhao, K.; Liu, K. S.; Li, T. F.; Wang, W.; Jiang, L. Superamphiphobic CaLi–based Bulk Metallic Glasses. *Scripta*. *Mater*. **2009**, *60*, 225–227.

(124). Vilcnik, A.; Jerman, I.; Vuk, A. S.; Koželj, M.; Orel, B.; Tomšič, B.; Simončič, B.; Kovač, J. Structural Properties and Antibacterial Effects of Hydrophobic and Oleophobic sol−gel Coatings for Cotton Fabrics. *Langmuir,* **2009**, *25*, 5869–5880.

(125). Martinelli, E.; Suffredini, M.; Galli, G.; Glisenti, A.; Pettitt, M. E.; Callow, M. E.; Callow, J. A.; Williams, D.; Lyall, G. Amphiphilic Block Copolymer/poly(dimethylsiloxane) (PDMS) Blends and Nanocomposites for Improved Fouling–release. *Biofouling* **2011**, *27*, 529–541.

(126). Burdallo, I.; Jorquera, C. J.; Sánchez, C. F.; Baldi, A. Integration of Microelectronic Chips in Microfluidic Systems on Printed Circuit Board. *J. Micromech. Microeng*. **2012**, *22*, 1–7.

(127). Dhananjay, B.; Chantal, K. M. Formation of More Stable Hydrophilic Surfaces of PDMS by Plasma and Chemical Treatments. *Microelectron. Eng*. **2006**, *83*, 1277–1279.

(128). Dhananjay, B.; Chantal, K. M. Hydrophilization and Hydrophobic Recovery of PDMS by Oxygen Plasma and Chemical Treatment—An SEM investigation. *Sensor*. *Actuat*. *B* **2007**, *123*, 368–373.

(129). Lakshmi, R. V.; Bharathidasan, T.; Bera, P.; Basu, B. Fabrication of Superhydrophobic and Oleophobic sol–gel Nanocomposite Coating. *J. Surf. Coat. Tech*. **2012**, *206*, 3888–3894.

(130). Coclite, A. M.; Shi, Y.; and Gleason, K. K. Grafted Crystalline Poly-Perfluoroacrylate Structures for Superhydrophobic and Oleophobic Functional Coatings. *Adv. Mater*. **2012**, *24*, 4534–4539.

(131). Zhang, F.; Zhang, W. B.; Shi, Z.; Wang, D.; Jin, J.; Jiang, L. Nanowire-Haired Inorganic Membranes with Superhydrophilicity and Underwater Ultralow Adhesive Superoleophobicity for High-Efficiency Oil/Water Separation. *Adv. Mater.* **2013**, *25*, 4192–4198.

(132). Yildiz, H. O.; Morrow, N. R. Effect of brine composition on recovery waterflooding. *J. Petrol. Sci. Eng.* **1996**, *14*, 159–168.

(133). Yao, X.; Gao, J.; Song, Y.; Jiang, L. Superoleophobic Surfaces with Controllable Oil Adhesion and Their Application in Oil Transportation. *Adv. Funct. Mater.* **2011**, *21*, 4270–4276.

(134). Xu, F.; Zhu, Y. Highly Conductive and Stretchable Silver Nanowire Conductors. *Adv. Mater.* **2012**, *24*, 5117–5122.

(135). Hansen, T. S.; West, K.; Hassager, O.; Larsen. N. B. Highly Stretchable and Conductive Polymer Material Made from Poly(3,4–ethylenedioxythiophene) and Polyurethane Elastomers. *Adv. Funct. Mater.* **2007**, *17*, 3069–3073.

(136). Liu, C. X.; Choi, J. W. Patterning Conductive PDMS Nanocomposite in an Elastomer Using Microcontact Printing. *J. Micromech. Microeng*. **2009**, *19*, 085019.

(137). Wang, H.; Zhou, H. Robust, Electro–conductive, Self–healing Superamphiphobic Fabric Prepared by One–step Vapour–phase Polymerisation of Poly(3,4–ethylenedioxythiophene) in the Presence of Fluorinated Decyl polyhedral Oligomeric Silsesquioxane and Fluorinated Alkylsilane. *Soft Matter.* **2013**, *9*, 277–282.

(138). Wang, H.; Xue, Y.; Lin, T. One–step Vapour–phase Formation of Patternable, Electrically Conductive, Superamphiphobic Coatings on Fibrous Materials. *Soft Matter.* **2011**, *7*, 8158–8161.

(139). Cong, H.; Pan, T. Photopatternable Conductive PDMS Materials for Microfabrication. *Adv. Funct. Mater.* **2008**, *18*, 1912–1921.

(140). Niu, X.; Peng, S.; Liu, L.; Wen, W.; and Shang, P. Characterizing and Patterning of PDMS-Based Conducting Composites. *Adv. Matter.* **2007**, *19*, 2682–2686.

(141). Das, A.; Schutzius, T. M.; Bayer, I. S.; Megaridis, C. M. Superoleophobic and Conductive Carbon Nanofiber/Fluoropolymer Composite Films. *Carbon*. **2012**, *50*,1346–1354.

(142). Gao, C.; MaCarthy, T. J. The “Lotus Effect” Explained–two Reasons Why Two Length Scales of Topography Are Important. *Langmuir* **2006**, 22, 2966–2967.

(143). Sun, T.; Wang, J.; Feng, L.; Liu, B.; Ma, Y.; Jiang, L.; Zhu, D. Reversible Switching between Superhydrophilicity and Superhydrophobicity. *Angew. Chem. Int. Ed.* **2004**, *43*, 357–360.

(144). Coulson, S. R.; Woodward, I.; Badyal, J. P. S. Super–repellent Composite Fluoropolymer Surfaces. *J. Phys. Chem. B* 2000, 104, 8836–8840.

(145). Howarter, J. A.; Genson, K. L.; Youngblood, J. P. Wetting Behavior of Oleophobic Polymer Coatings Synthesized from Fluorosurfactant–macromers. *ACS Appl. Mater. Interfaces* **2011**, *3*, 2022–2030.

(146). Liu, M.; Wang, S.; Wei, Z.; Song, Y.; L. Jiang, Y. Bioinspired Design of a Superoleophobic and Low Adhesive Water/solid Interface. *Adv. Mater.* **2009**, *21*, 665–669.

(147). Bellanger, H.; Darmanin, T.; de Givenchy, E. T.; Guittard, F. Influence of Intrinsic Oleophobicity and Surface Structuration on the Superoleophobic Properties of PEDOP Films Bearing Two Fluorinated Tails. *J. Mater. Chem. A* **2013**, *1*, 2896–2903.

(148). Zhang, J.; Seeger, S. Superoleophobic Coatings with Ultralow Sliding Angles Based on Silicone Nanofilaments. *Angew. Chem. Int. Ed. English* **2011**, *50*, 6652–6656.

(149). Brewer, S. A.; Willis, C. R. Structure and Oil Repellency. *Appl. Surf. Sci*. **2008**, *254*, 6450–6454.

(150). Ghosh, N.; Bajoria, A.; Vaidya, A. A. Surface Chemical Modification of Poly(dimethylsiloxane)–based Biomimetic Materials: Oil–repellent Surfaces. *ACS Appl. Mater. Interfaces* **2009**, *1*, 2636–2644.

(151). Wang, J.; Song, X.; Li, R.; Shen, J.; Yang, G.; Huang, H. Fluorocarbon Thin Film with Superhydrophobic Property Prepared by Pyrolysis of Hexafluoropropylene Oxide. *Appl. Surf. Sci.* **2012**, *258*, 9782–9785.

(152). Xiang, H.; Komvopoulos, K. Effect of Fluorocarbon Self–assembled Monolayer Films on Sidewall Adhesion and Friction of Surface Micromachines with Impacting and Sliding Contact Interfaces. *J. Appl. Phys*. **2013**, *11*3, 224505 1–9.

(153). Zhao, H.; Law, K. Y.; Sambhy, V. Fabrication, Surface Properties, and Origin of Superoleophobicity for a Model Textured Surface. *Langmuir* **2011**, *27*, 5927–5935.

(154). Darmanin, T.; Guittard, F. Superoleophobic Surfaces with Short Fluorinated Chains? *Soft Matter* **2013**, *9*, 5982–5990.

(155). Yu, H.; Zhou, G.; Chau, F. S.; Wang, S.; Lee, F. Novel Polydimethylsiloxane (PDMS) Based Microchannel Fabrication Method for Lab–on–a–chip Application. *Sens. Actuators B* **2009**, *137*, 754–761.

(156). Kushmeric, J. G.; Hankins, M. G.; de Boer, M. P.; Clews, P. J.; Carpick, R. W. The Influence of Coating Structure on Micromachine Stiction. *Tribol Lett*. **2001**, *10*, 103–108.

(157). Kim, B. H.; Chung, T. D.; Chun, K. A New Organic Modifier for Anti–friction. *J. Microelectromech. S*. **2001**, *10*, 33–40.

(158). Diebold, R. M.; Clarke, D. R. Smooth, Aggregate–free Self–assembled Monolayer Deposition of Silane Coupling Agents on Silicon Dioxide. *Langmuir* **2012**, *28*, 15513–15520.

(159). Shahsavan, H.; Zhao, B. Conformal Adhesion Enhancement on Biomimetic Microstructured Surfaces. *Langmuir* **2011**, *27*, 7732–7742.

(160). Mihály, J.; Sterkel, S.; Ortner, H. M.; Kocsis, L.; Hajba, L.; Furdyga, É.; Mink, J. FTIR and FT–Raman Spectroscopic Study on Polymer Based High Pressure Digestion Vessels. *Croat. Chem. Acta* **2006**, *79*, 497–501.

(161). Kang, G.; Ko, H. J.; Choi, C. K. Chemical Bond Structure of a–C:F Films with a Low Dielectric Constant Deposited by Using CH_4/CF_4 ICPCVD. *J. Korean Phys. Soc*. **2003**, *42*, 676–681.

(162). Koberstein, J. T. Molecular Design of Functional Polymer Surfaces. *J. Polym. Sci. Pol. Phys*. **2004**, *42*, 2942–2956.

(163). Bousquet, A.; Pannier, G.; Ibarboure, E.; Papon, E.; Rodríguez–Hernández, J. Control of the Surface Properties in Polymer Blends. *J. Adhesion* **2007**, *83*, 335–349.

(164). Lim, J. A.; Lee, W. H.; Kwak, D.; Cho, K. Evaporation–induced Self–organization of Inkjet–printed Organic Semiconductors on Surface–modified Dielectrics for High–performance Organic Transistors. *Langmuir* **2009**, *25*, 5404–5410.

(165). Janssen, D.; Palma, R. D.; Verlaak, S.; Heremans, P.; Dehaen, W. Static Solvent Contact Angle Measurements, Surface Free Energy and Wettability Determination of Various Self–assembled Monolayers on Silicon Dioxide. *Thin Solid Films* **2006**, *515*, 1433–1438.

(166). Tang, W.; Huang, Y.; Meng, W.; Qing, F. L. Synthesis of Fluorinated Hyperbranched Polymers Capable as Highly Hydrophobic and Oleophobic Coating Materials. *Eur. Polym. J.* **2010**, *46*, 506–518.

(167). Basu, B. J.; Kumar, V. D.; Anandan, C. Surface Studies on Superhydrophobic and Oleophobic Polydimethylsiloxane–silica Nanocomposite Coating System. *Appl. Surf. Sci*. **2012**, *261*, 807–814.

(168). Yang, F. K.; Zhang, W.; Han, Y.; Yoffe, S.; Cho, Y.; Zhao, B. Contact of Nanoscale Stiff Films. *Langmuir* **2012**, *28*, 9562–9572.

(169). Rieke, P. C. Application of Van oss–Chaudhury–Good Theory of Wettability to Interpretation of Interfacial Free Energies of Heterogeneous Nucleation. *J. Cryst. Growth* **1997**, *182*, 472–484.

(170). Sibonio, S.; Volpe, C. D. On the Definition of Scales in Van oss–Chaudhury–Good Acid–base Theory. *MATCH–Commun. Math. Co*. **2006**, *56*, 291–316.

(171). Zhang, W.; Zheng, Y.; Orsini, L.; Morelli, A.; Galli, G.; Chiellini, E.; Carpenter, E. E.; Wynne, K. J. More Fluorous Surface Modifier Makes it Less Oleophobic: Fluorinated Siloxane Copolymer/PDMS Coatings. *Langmuir* **2010**, *26*, 5848–5855.

(172). Zhang, Y.; Xia, H.; Kim, E; Sun, H. Recent developments in superhydrophobic surfaces with unique structural and functional properties. *Soft Matter* **2012**, *8*, 11217–11231.

(173). Zhang, W.; Yang, K. F.; Han, Y.; Gaikwad, R.; Leonenko, Z.; Zhao, B. Surface and tribological behaviors of the bioinspired polydopamine thin films under dry and wet conditions. *Biomacromolecules* **2013**, *14*, 394–405.

(174). Pan, Z.; Shahsavan, H.; Zhang, W.; Yang, F. K.; Zhao, B. Superhydro–oleophobic bio–inspired polydimethylsiloxane micropillared surface via FDTS coating/blending approaches. *Appl. Sur. Sci.* **2015**, *324*, 612–620.

(175). Wang, D.; Liu, Y.; Liu, X.; Zhou, F.; Liu, W.; Xue, Q. Towards a tunable and switchable water adhesion on a TiO($_2$) nanotube film with patterned wettability. *Chem. Commun.* **2009**, 7018–7020.

(176). Xu, L. P.; Zhao, J.; Su, B.; Liu, X.; Peng, J.; Liu, Y.; Liu, H.; Yang, G.; Jiang, L.; Wen, Y.; Zhang, X.; Wang, S. An ion–induced low–oil–adhesion organic/inorganic hybrid film for stable superoleophobicity in seawater. *Adv. Mater.* **2013**, *25*, 606–611.

(177). Zhang, W.; Yang, K. F.; Pan, Z.; Zhang, J.; Zhao, B. Bio–Inspired dopamine functionalization of polypyrrole for improved adhesion and conductivity. *Macromol. Rapid Commun.* **2014**, *35*, 350–354.

(178). Zhang, W.; Pan, Z.; Yang, K. F.; Zhao, B. A facile in situ approach to polypyrrole functionalization through bioinspired catechols. *Adv. Funct. Mater.* **2015**, *25*, 1588–1597.

(179). Cheng, Q.; Li, M.; Yang, F.; Liu, M.; Li, Lin.; Wang S. Jiang L. An underwater pH–responsive superoleophobic surface with reversibly switchable oil–adhesion. *Soft Matter* **2012**, *8*, 6740–6744.

(180). Ramachandran, R.; Sobolev, K.; Nosonovsky, M. Dynamics of droplet impact on hydrophobic/icephobic concrete with the potential for superhydrophobicity. *Langmuir* **2015**, *31*, 1437−1444.

(181). Stone, H. A. Ice–phobic Surfaces That Are Wet. *ACS Nano*, **2012**, *6*, 6536–6540.

(182). Subramanyam, S. B.; Rykaczewski, K.; Varanasi, K. K. Ice Adhesion on Lubricant–Impregnated Textured Surfaces. *Langmuir* **2013**, *29*, 13414–13418.

(183). Wang, C.; Zhang, W.; Siva, A.; Tiea, D.; Wynne, K. J. Laboratory Test for Ice Adhesion Strength Using Commercial Instrumentation. *Langmuir* **2014**, *30*, 540–547.

(184). Wang, Y.; Xue, J.; Wang, Q.; Chen, Q.; Ding, J.: Verification of Icephobic/anti–icing Properties of a Superhydrophobic Surface. *ACS Appl. Mater.Inter.* **2013**, *5*, 3370–3381.

(185). Fu, Q.; Wu, X.; Kumar, D.; Ho, J. W.; Kanhere, P. D.; Srikanth, N.; Liu, E.; Wilson, P.; Chen, Z. Development of sol–gel Icephobic Coatings: Effect of Surface Roughness and Surface Energy. *ACS Appl. Mater. Inter.* **2014**, *6*, 20685–20692

(186). Glassmaker, N. J. ; Jagota, A.; Hui, C. Y.; Kim, J. Design of Biomimetic Fibrillar Interfaces: 1. Making Contact. *J. R. Soc. Interface* **2004**, *1*, 23–33.

(187). Chandra, A.; Yang, S. Stability of High–aspect–ratio Micropillar Arrays Against Adhesive and Capillary Forces. *Accounts Chem. Res.* **2010**, *43*, 1080–1091.

(188). Hui, C. Y.; Jagota, A.; Lin, Y. Y.; Kramer, E. J. Constraints on Microcontact Printing Imposed by Stamp Deformation. *Langmuir* **2002,** *18*, 1394–1407.

(189). McDonald, B.; Patel, P.; Zhao, B. Droplet Freezing and Ice Adhesion Measurement on Super–cooled Hydrophobic Surfaces. *J. Adhesion*, Accepted, **July 2015**.

(190). Bennett, S. J.; Deveries, K. L. Williams, M. L. Adhesive Fracture Mechanics. *Int. J. Fracture,* **1974**, *10*, 33–44.

(191). Akisanys, A. R. Fleck, N. A. Britle Fracture of Adhesive. *Int. J. Fracture* **1992**, *58*, 93–114.

(192). Jellinek, H. H. G. Adhesive Properties of Ice. *J. of Colloid Sci.* **1959**, *14*, 268–280.

(193). Higgins, J.; Wallace, S.; Minkel, K.; Wagner, R.; Liner, M.; Meal, G. The Design & Operation of a Very Large Vertical Sub–surface Flow Engineered Wetland to Treat Spent Deicing Fluids and Glycol–contaminated Stormwater at Buffalo Niagara International airport. *W. P. T.* **2011**, *6*, DOI: 10.2166/wpt.2011.044.

(194). Lee, H. S.; Singh, P.; Thomason, W.H.; Fogler, H.S. Waxy Oil Gel Breaking Mechanisms: Adhesive Versus Cohesive Failure. *Energy Fuels* **2008**, *22*, 480–487.

(195). Lin, C.; He, G.; Dong, C.; Liu, H.; Xiao, G.; Liu, Y. F. Effect of Oil Phase Transition on Freeze/thaw–induced Demulsification of Water–in–oil emulsions. *Langmuir* **2008**, *24*, 5291–5298.

(196). Darmanin, T.; Tarrade, J.; Celia, E.; Guittard, F. Superoleophobic Meshes with High Adhesion by Electrodeposition of Conducting Polymer Containing Short Perfluorobutyl Chains. *J. Phys. Chem. C* **2014**, *118*, 2052–2057.

(197). Hsieh, C. T.; Wu, F. L.; Chen, W. Y. Contact Angle hysteresis and Work of Adhesion of Oil Droplets on Nanosphere Stacking Layers. *J. Phys. Chem. C* **2009**, *113*, 13683–13688.

(198). Chen, K.; Zhou, S.; Wu, L. Self–healing Underwater Superoleophobic and Antibiofouling Coatings Based on the Assembly of Hierarchical Microgel Spheres. *ACS Nano* **2016**, *10*, 1386–1394.

(199). Pan, Z.; Zhang, W.; Kowalski, A.; Zhao, B. Oleophobicity of Biomimetic Micropatterned Surface and Its Effect on the Adhesion of Frozen Oil. *Langmuir* **2015**, *31*, 9901–9910.

(200). Meuler, A.J.; McKinley, G. H.; Cohen, R. E. Exploiting Topographical Texture to Impart Icephobicity. *ACS Nano* **2010**, *4*, 7048–7052.

(201). Boinovich, L. B.; Emelyanenko, A. M.; Ivanov, V. K.; Pashinin, A. S. Durable Icephobic Coating for Stainless Steel. *ACS Appl. Mater. Interfaces* **2013**, *5*, 2549–2554.

(202). Yeong, Y. H.; Milionis, A.; Loth, E.; Sokhey, J.; Lambourne, A. Atmospheric Ice Adhesion on Water–repellent Coatings: Wetting and Surface Topology Effects. *Langmuir* **2015**, *31*, 13107–13116.

(203). Ling, E.J.; Uong, V.; Renault–Crispo, J. S.; Kietzig, A. M.; Servio, P. Reducing Ice Adhesion on Non–smooth Metallic Surfaces: Wettability and Topography Effects. *ACS Appl. Mater. Interfaces* **2016**, DOI: 10.1021/acsami.6b00187.

(204). Kim, P.; Wong, T. S.; Alvarenga, J.; Kreder, M. J.; Adorno–Martinez, W. E.; Aizenberg, J. Liquid–infused Nanostructured Surfaces with Extreme Anti–ice and Anti–frost Performance. *ACS Nano* **2012**, *6*, 6569–6577.

(205). Miljkovic, N.; Preston, D. J.; Enright, R.; Wang, E. N. Electric–field–enhanced Condensation on Superhydrophobic Nanostructured Surfaces. *ACS Nano* **2013**, *7*, 11043–11054.

(206). Lv, J.; Song, Y.; Jiang, L.; Wang, J. Bio–inspired Strategies for Anti–icing. *ACS Nano* **2014**, *8*, 3152–3169.

(207). Péter, Z.; Volat, C.; Farzaneh, M.; Kiss, L. I. Numerical Investigations of a Nnew Thermal De–icing Method for Overhead Conductors Based on High Current Impulses. *IET Gener. Trans. Dis.* **2008**, *2*, 666–675.

(208). Xu, Z.; Jia, Z.; Li, Z.; Wei, X.; Guan, Z.; MacAlpine, M.; Zhao, Y.; Li, Y. Anti–icing Performance of RTV Coatings on Porcelain Insulators by Controlling the Leakage Current. *IEEE Trans. Dielectr. Electr. Insul.* **2011**, *18*, 760–766.

(209). Sekitani, T.; Takamiya, M.; Noguchi, Y.; Nakano, S.; Kato, Y.; Sakurai, T.; Someya, T. A Large–area Wireless Power–transmission Sheet Using Printed Organic Transistors and Plastic MEMS Switches. *Nat. Mater.* **2007**, *6*, 413–417.

(210). Cao, A.; Dickrell, P.L.; Sawyer, W. G.; Ghasemi–Nejhad, M. N.; Ajayan, P. M. Super–compressible Foamlike Carbon Nanotube Films. *Science* **2005**, *310*, 1307–1310.

(211). Sengupta, R.; Bhattacharya, M.; Bandyopadhyay, S.; Bhowmick, A. K. A Review on the Mechanical and Electrical Properties of Graphite and Modified Graphite Reinforced Polymer Composites. *Prog. Polym. Sci.* **2011**, *36*, 638–670.

(212). Deng, H.; Lin, L.; Ji, M.; Zhang, S.; Yang, M.; Fu, Q. Progress on the Morphological Control of Conductive Network in Conductive Polymer Composites and the Use as Electroactive Multifunctional Materials. *Prog. Polym. Sci.* **2014**, *39*, 627–655.

(213). Pan, Z.; Wang, T.; Sun, S.; Zhao, B. Durable Microstructured Surfaces: Combining Electrical Conductivity with Superoleophobicity. *ACS Appl. Mater. Interfaces* 2016, 8, 1795–1804.

(214). Hoque, E.; DeRose, J. A.; Houriet, R.; Hoffmann, P.; Mathieu, H. J. Stable Perfluorosilane Self–assembled Monolayers on Copper Oxide Surfaces: Evidence of Siloxy–copper Bond Formation. *Chem. Mater*. **2007**, *19*, 798–804.

(215). Aryal, M.; Trivedi, K.; Hu, W. W. Nano–confinement Induced Chain Alignment in Ordered P_3HT Nanostructures Defined by Nanoimprint Lithography. *ACS Nano* 2009, 3, 3085–3090.

(216). Sharpe, R .B. A.; Burdinski, D.; Huskens, J.; Zandvliet, H. J. W.; Reinhoudt, D. N.; Poelsema, B. Chemically Patterned Flat Stamps for Microcontact Printing–FDTS. *J. Am. Chem. Soc.* **2005**, *127*, 10344–10349.

(217). Mochalin, V. N.; Neitzel, I.; Etzold, B. J. M.; Peterson, A.; Palmese, G.; Gogotsi, Y. Covalent Incorporation of Aminated Nanodiamond into an Epoxy Polymer Network. *ACS Nano* **2011**, *5*, 7494–7502.

(218). Li, Y.; Huang, X. J.; Heo, S. H.; Li, C. C.; Choi, Y. K.; Cai, W. P.; Cho, S. O. Superhydrophobic Bionic Surfaces with Hierarchical Microsphere/SWCNT Composite Arrays. *Langmuir* **2007**, *23*, 2169–2174.

(219). Furmidge, C.G. Studies at Phase Interfaces: I. the Sliding of Liquid Drops on Solid Surfaces and a Theory for Spray Retention. *J. Colloid Sci.* **1962**, *17*, 309–324.

(220). Sekitani, T.; Takamiya, M.; Noguchi, Y.; Nakano, S.; Kato, Y.; Sakurai, T.; Someya, T. A Large–area Wireless Power–Transmission Sheet Using Printed Organic Transistors and Plastic MEMS Switches. *Nat. Mater.* **2007,** *6*, 413–417.

(221). Mao, P.; Mahapatra, A. K.; Chen, J.; Chen, M.; Wang, G.; Han, M. Fabrication of Polystyrene/ZnO Micronano Hierarchical Structure Applied for Light Extraction of Light–Emitting Devices. *ACS Appl. Mater. Interfaces* **2015,** *7*, 19179–19188.

(222). Taleb, S.; Darmanin, T.; Guittard, F. Superhydrophobic Conducting Polymers with Switchable Water and Oil Repellency by Voltage and Ion Exchange. *RSC Adv.* **2014**, *4*, 3550–3555.

(223). Kim, J.; Lin, P.; Kim, W. S. Mechanically Robust Super–oleophobic Stamp for Direct Stamping of Silver Nanoparticle Ink. *Thin Solid Films* **2012,** *520*, 4339–4343.

(224). Tang, Y.; Gong, S; Yap, L. W; Cheng, W. Manufacturable Conducting Rubber Ambers and Stretchable Conductors from Copper Nanowire Aerogel Monoliths. *ACS Nano* **2014,** *8*, 5707–5714.

(225). Al–Saleh, M. H.; Sundararaj, U. A Review of Vapor Grown Carbon Nanofiber/Polymer Conductive Composites. *Carbon* **2009**, *47*, 2–22

(226). Yang, Y.; Gupta, M. C.; Dudley K. L.; Lawrence, R. W. Conductive Carbon Nanofiber–Polymer Foam Structure. *Adv. Mater.* **2005**, *17*, 1999–2003.

(227). Yousefi, N.; Sun, X.; Lin, X.; Shen, X.; Jia, J.; Zhang, B.; Tang, B.; Chan, M.; Kim, J. K. Highly Aligned Graphene/Polymer Nanocomposites with Excellent Dielectric Properties for High–Performance Electromagnetic Interference Shielding. *Adv. Mater.* **2014**, *26*, 5480–5487.

(228). Grujicic, M.; Sellappan, V.; Omar, M. A.; Seyr, N.; Obieglo, A.; Erdmann, M.; Holzleitner, J. An Overview of the Polymer–to–Metal Direct–Adhesion Hybrid Technologies for Load–Bearing Automotive Components. *J. Mater. Process. Technol.* **2008**, *197*, 363–373.

(229). Venables, J. D. Adhesion and Durability of Metal–Polymer Bonds. *J. Mater. Sci.* **1984**, *19,* 2431–2453.

(230). Lee, H. H.; Chou, K. S.; Shih, Z. W. Effect of Nano–sized Silver Particles on the Resistivity of Polymeric Conductive Adhesives. *Int. J. Adhes. Adhes.* **2005**, *25*, 437–441.

(231). Chang, C. A. Adhesion Studies of Metals on Fluorocarbon Polymer Films. *J.Vacuum Sci. Technol. , A* **1990**, *8*, 3304–3309.

(232). Wu, P. K.; Lu, T. M. Metal/Polymer Adhesion Enhancement by Reactive Ion Assisted Interface Bonding and Mixing. *Appl. Phys. Lett.* **1997**, *71*, 2710–2172.

(233). Friedrich, J. F.; Mix, R.; Kühn, G. Adhesion of Metals to Plasma–Induced Functional Groups at Polymer Surfaces. *Surf. Coat. Technol.* **2005**, *200*, 565–568.

(234). Karger–Kocsis, J.; Mahmood, H.; Pegoretti, A. Recent Advances in Fiber/Matrix Interphase Engineering for Polymer Composites. *Prog. Mater. Sci.* **2015**, *73*, 1–43.

(235). Xue, C. H.; Chen, J.; Yin, W.; Jia, S. T.; Ma, J. Z. Superhydrophobic Conductive Textiles with Antibacterial Property by Coating Fibers with Silver Nanoparticles. *Appl. Surf. Sci.* **2012**, *258*, 2468–2472.

(236). Ghosh, N.; Bajoria, A.; Vaidya, A. A. Surface Chemical Modification of Poly(dimethylsiloxane)–Based Biomimetic Materials: Oil–Repellent Surfaces. *ACS Appl. Mater. Interfaces* **2009**, *1*, 2636–2644.

(237). Shahsavan, H.; Arunbabu, D.; Zhao, B. Biomimetic Modification of Polymeric Surfaces: A Promising Pathway for Tuning of Wetting and Adhesion. *Macromol. Mater. Eng.* **2012**, *297*, 743–760.

(238). Kholid, F. N.; Huang, H.; Zhang, Y.; Fan, H. J. Multiple Electrical Breakdowns and Electrical Annealing Using High Current Approximating Breakdown Current of Silver Nanowire Network. *Nanotechnology* **2016**, *27*, 025703.

(239). Kaspers, M. R.; Bernhart, A. M.; Bobisch, C. A.; Möller, R. Current Induced Surface Diffusion on A Single–Crystalline Silver Nanowire. *Nanotechnology* **2012**, *23*, 205706.

(240). Cholewinski, A.; Trinidad, J.; McDonald, B.; Zhao, B. Bio–inspired Polydimethylsiloxane–Functionalized Silica Particles–Epoxy Bilayer as a Robust Superhydrophobic Surface Coating. *Surf. Coat. Technol.* **2014**, *254*, 230–237.

(241). Varenberg, M.; Gorb, S. N. Hexagonal Surface Micropattern for Dry and Wet Friction. *Adv. Mater.* **2009**, *21*, 483–486.

(242). Wang, H.; Nair, R.; Zou, M.; Larson, P. R.; Pollack, A. L.; Hobbs, K. L.; Johnson, M. B.; Awitor, O. K. Friction Study of a Ni Nanodot–Patterned Surface. *Tribol. Lett.* **2007**, *28*,183–189.